

ATOMIC RESOLUTION d^2I/dV^2 -IMAGING OF LATTICE IMPACT ON
SUPERCONDUCTIVITY IN HIGH- T_c SUPERCONDUCTORS

A Dissertation

Presented to the Faculty of the Graduate School
of Cornell University

In Partial Fulfillment of the Requirements for the Degree of
Doctor of Philosophy

by

Miao Wang

August 2008

© 2008 Miao Wang

ATOMIC RESOLUTION d^2I/dV^2 -IMAGING OF LATTICE IMPACT ON SUPERCONDUCTIVITY IN HIGH- T_c SUPERCONDUCTORS

Miao Wang, Ph. D.

Cornell University 2008

The role of electron-lattice interaction in pair formation in high- T_c superconductivity has been under debate for twenty years. One thing which strongly distinguishes copper-oxides is that pairing appears to occur at atomic scale. Thus it is at atomic scale where electron-lattice interactions need to be examined. Using newly developed atomic resolution d^2I/dV^2 -imaging technique with other well established spectroscopic imaging methods, three major experiments are performed to investigate lattice impact on superconductivity.

The first experiment reveals intense disorder of mode energy at nanometer scale. d^2I/dV^2 exhibits modulation along Cu-O bond direction and signatures interaction of antinodal quasiparticle with the bosonic mode. The average mode energy has minimal change with changing hole density. Substitution of ^{16}O for ^{18}O throughout the crystal exhibits the classic isotope shift in mode energy. Moreover, the local gap disorder $\Delta(\mathbf{r})$ and mode energy $\Omega(\mathbf{r})$ are anti-correlated.

The second experiment reveals the impact of periodic unit cell distortion on local superconductivity. The periodic unit cell distortion manifests itself as the incommensurate bulk crystalline modulation (called supermodulation). A technique called phase map is developed to accurately determine local supermodulation phase ϕ .

Superconducting gap is found to vary co-sinusoidally with ϕ , indicating that the local pairing strength is modulated by Cu-O_{apical} bond length d_A . Therefore a non random out-of-plane effect of lattice on superconductivity is identified.

In the last experiment, Ω is found to vary co-sinusoidally with ϕ , similar to pairing gap, but almost 180° out of phase. This means Δ and Ω are both modulated by periodic distortion of CuO₅ cage. Experiments on ¹⁶O/¹⁸O isotope samples at the same doping level are performed. Careful comparison of superconducting electronic structure of the isotope samples shows no detectable change. The only change is that the $\Omega(\phi)$ is systematically shifted by several mV while the $\Delta(\phi)$ remains unchanged.

Thorough studies presented in this thesis on **r**- and **k**-space electronic structure with atomic resolution, as well as impact of unit cell dimension change on pairing and lattice vibration mode, provide a complete set of microscopic experimental description of isotope effects in Cuprates, which any theoretical model should be consistent with.

BIOGRAPHICAL SKETCH

Miao Wang was born on April 21, 1980 in Xichang, Sichuan province in China. He went to high school in Chengdu, China from 1995-1998. He was admitted to physics department, Tsinghua University, Beijing China in 1998. In the first week of his college life in Beijing, he got full scholarship from Hong Kong government and Hong Kong Jockey Club for outstanding mainland students and transferred to physics department, Hong Kong University of Science and Technology (HKUST). He spent his last year in undergraduate working with Prof. Xudong Xiao and graduate student Tao Su, to manipulate CO molecules on gold surface. In 2002, he graduated from HKUST and went to physics department at Cornell University. In 2003, he joined research group of Prof. J. C. Davis. Using low temperature STM, he studied two strongly correlated electron systems: superconducting Cuprates and Ruthenates. This thesis mainly contains the results from Cuprate studies.

To My Mother and Grandparents

ACKNOWLEDGMENTS

The first person to thank is my adviser, Prof. Seamus Davis. Without his tireless education and guidance, none of the experimental results presented in this thesis would have been possible. During my six year graduate school, Seamus has shown me what it takes to be a world class scientist: deep insight, superior expertise in technical details, ability to motivate colleagues, strategic thinking and high standard of scientific integrity.

To my parents and grandparents, your love and support have always been with me through rise and falls during my years in the graduate school, and from the moment I was born. I know you are proud of me, but I want to you know that I am proud of you too, always.

My first thank to my colleagues goes to Dr. Joan Hoffmann. As a senior student, you taught me hand on hand how to do low temperature experiment. I always admire you as an excellent experimentalist, especially your beautiful design of low noise cryostat for ^4He experiment. I met Benjamin Hunt in my first day at Cornell in ISSO, and one year later we ended up working on superfluid ^4He experiment led by Joan for my first two years in Davis group. A lot of surprises, wonderful or nasty, during the construction of ^4He experiment. Those were happy times in ^4He group I will remember.

The next important colleague/mentor is Dr. Jinho Lee, who led the d^2I/dV^2 project and trained me to operate and maintain the machine after my switching to STM1. Thank you Jinho for your patience on me and your groundbreaking work which led to

the subsequent experiments presented in this thesis. On STM1 I also closely worked with Dr. Kazuhiro Fujita for more than two years. I benefited enormously from your broad knowledge of Cuprates and your calm personality.

Dr. Jacob Alldredge, for all the laughter and bitterness, it's been weirdly pleasant to have worked with you, and passed my defense one day earlier than you. Your smartness really impresses me.

For the Ruthenates experiment during the last one and half years in my Ph.D., it is my great honor to have worked with Prof. Andy Mackenzie from University of St. Andrews in Scotland. I appreciate the opportunity to study $\text{Sr}_3\text{Ru}_2\text{O}_7$ you brought to us.

I have also worked with Dr. Yuhki Kohsaka, Prof. Christian Lupien, Dr. Minoru Yamashita, Dr. Peter Wahl, Dr. Jinhwan Lee, Dr. Tien-Ming Chuang, Dr. Curry Taylor, Dr. James Slezak, Milan Allan, Andy Schmidt, Ethan Pratt, Mohammad Hamidian, Hiro Miyake and Jason Farrell (who grows $\text{Sr}_3\text{Ru}_2\text{O}_7$ from U. of St. Andrews). Wish all good luck in their future study and career.

TABLE OF CONTENTS

Biographical sketch.....	iii
Dedication.....	iv
Acknowledgements.....	v
Table of contents.....	vii
List of figures.....	x
List of tables.....	xiv

CHAPTER 1: INTRODUCTION TO LOW TEMPERATURE SCANNING TUNNELING MICROSCOPY AND SPECTROSCOPIC IMAGING

STM.....	1
1.1 Scanning Tunneling Microscopy.....	1
1.2 Spectroscopic Imaging STM.....	8
1.3 Noise Consideration.....	10

CHAPTER 2: STM STUDY ON CUPRATES – THE PAST MEASUREMENT PARADIGM.....

PARADIGM.....	14
2.1 BCS Superconductivity.....	14
2.2 Cuprate Superconductor: Basics.....	19
2.3 STM on Cuprate.....	27
2.4 <i>d</i> -wave Energy Gap Map.....	30
2.5 Quasiparticle Interference (QPI).....	33
2.6 Dopant Oxygen as Source of Local Electronic Disorder.....	37

CHAPTER 3: INTERPLAY BETWEEN LATTICE AND SUPERCONDUCTIVITY IN CUPRATE.....

3.1	The Dip-Hump Feature in Cuprate Superconductor.....	40
3.2	d^2I/dV^2 Technique and Gap Referencing.....	45
3.3	Doping Dependence of Mode Energy.....	50
3.4	Interaction with Antinodal Quasiparticle.....	52
3.5	Oxygen Isotope Shift in Mode Energy.....	56
3.6	Anti-correlation between $\Delta(\mathbf{r})$ and $\Omega(\mathbf{r})$	58
3.7	Discussions.....	61

CHAPTER 4: IMPACT OF PERIODIC VARIATION OF INTER-ATOMIC DISTANCE ON SUPERCONDUCTIVITY.....63

4.1	Bulk Supermodulation in $\text{Bi}_2\text{Sr}_2\text{CaCu}_2\text{O}_{8+\delta}$	64
4.2	Extracting Local Supermodulation Phase.....	68
4.3	Impact of Periodic Unit Cell Distortion on Superconductivity.....	73
4.4	Discussion and Conclusions.....	81

CHAPTER 5: IMPACT OF PERIODIC UNIT CELL DISTORTION ON ELECTRON-LATTICE COUPLING.....84

5.1	Remaining Questions from Previous Electron-Lattice Study.....	84
5.2	Review of Isotope Effects in High- T_c Superconductor.....	86
5.3	Oxygen isotope effects on gap and mode energy in optimally doped Bi- 2212.....	89
5.4	Effect of Periodic Unit Cell Distortion on Electron-Lattice Coupling.....	93
5.5	Oxygen Isotope effect on $\bar{\Delta}(\phi)$ and $\bar{\Omega}(\phi)$	99
5.6	Oxygen Isotope Effect on Bogoliubov Quasiparticle Excitation.....	101
5.7	Examine Spectral Function $A(\mathbf{k}, \omega)$ upon Isotope Substitution.....	108
5.8	Discussions and Conclusions.....	112

5.8.1	Inelastic Stimulation of Apical Oxygen?.....	113
5.8.2	Electron-Lattice Interaction as Pairing Glue?.....	115
5.8.3	Anti-correlation Caused by Supermodulation?.....	118
5.8.4	Summary and Conclusions.....	120

APPENDIX A.

ATOMIC RESOLUTION d^2I/dV^2-IMAGING ON $\text{Sr}_3\text{Ru}_2\text{O}$.....	124
-------------------------------------------------------------------------------------------------------------	------------

References.....	133
------------------------	------------

LIST OF FIGURES

Figure 1-1: Schematic diagram of Scanning Tunneling Microscopy (STM).....	1
Figure 1-2: Schematics of quantum mechanical tunneling between tip and sample.....	3
Figure 1-3: Ultra-low vibration lab at Cornell.....	12
Figure 1-4: Circuit diagram of STM to model input noise.....	13
Figure 2-1: Cartoon of Cooper pair.....	15
Figure 2-2: magnetization of type I and type II superconductors.....	18
Figure 2-3: Crystal structure of three most important hole doped cuprates.....	20
Figure 2-4: Scheme of relative energy levels for Cu and O ions in HTSC cuprates....	21
Figure 2-5: Schematic phase diagram for hole doped cuprates.....	24
Figure 2-6: Summary of disorder types of different cuprate families.....	26
Figure 2-7: Cleaving of Bi-2212 crystal.....	27
Figure 2-8: Spatially averaged conductance for different dopings.....	31
Figure 2-9: Gap map measurement scheme.....	32
Figure 2-10: Band structure and ‘model’ for Bi-2212.....	35
Figure 2-11: \mathbf{r} -space and \mathbf{q} -space images of LDOS modulations.....	36
Figure 2-12: Oxygen map.....	38
Figure 3-1: Normalized conductance of superconducting Lead.....	41
Figure 3-2: Examples of different bosonic modes.....	44
Figure 3-3: Numeric procedure to extract $d^2 I / dV^2(\mathbf{r}, \omega)$ in $\text{Bi}_2\text{Sr}_2\text{CaCu}_2\text{O}_{8+\delta}$	48
Figure 3-4: Example of spatial distribution of bosonic mode energy $\Omega(\mathbf{r})$ in $\text{Bi}_2\text{Sr}_2\text{CaCu}_2\text{O}_{8+\delta}$	49
Figure 3-5: Doping dependence of $\Delta(\mathbf{r})$ and $\Omega(\mathbf{r})$	50
Figure 3-6: Doping dependence of energy gap histograms and boson energy histograms.....	51

Figure 3-7: Spatial modulation in $d^2I/dV^2(\mathbf{r}, \omega)$ after gap referencing.....	54
Figure 3-8: $^{18}\text{O}/^{16}\text{O}$ isotope effects on $d^2I/dV^2(\mathbf{r}, \omega)$ spectra and the distribution of boson energies.....	57
Figure 3-9: Anti-correlation between $\Delta(\mathbf{r})$ and $\Omega(\mathbf{r})$	59
Figure 4-1: Same modulation in topograph and gap map.....	65
Figure 4-2: Crystal structure of Bi-2212 and the periodic unit cell distortion due to bulk incommensurate supermodulation.....	66
Figure 4-3: Cu related bond length as function of supermodulation (1.0 measure phase of 2π).....	67
Figure 4-4: Illustration of phase map technique.....	71
Figure 4-5: Illustration of precision of phase map algorithm.....	73
Figure 4-6: Gap modulations at the same wavevector \mathbf{q}_{SM} as bulk modulation across different doping levels.....	74
Figure 4-7: Gap magnitude as a function of crystal supermodulation phase.....	75
Figure 4-8: Relative amplitude $2A$ (peak to peak) of the co-sinusoidal fit.....	76
Figure 4-9: Dopant density modulation.....	77
Figure 4-10: $\Delta(\mathbf{r})$ as a function of distance to dopant atoms.....	79
Figure 4-11: Spectra evolution as response to dopant atom and supermodulation.....	80
Figure 4-12: Local lattice distortion due to dopant oxygen.....	82
Figure 5-1: doping and layer number dependence of isotope effect in T_c	87
Figure 5-2: Magnetization measurement for $^{16}\text{O}/^{18}\text{O}$ substitution.....	90
Figure 5-3: Raman scattering evaluation of isotope substitution.....	91
Figure 5-4: Δ and Ω distriction for optimally doped $^{16}\text{O}/^{18}\text{O}$ Bi-2212.....	92
Figure 5-5: $\Delta(\mathbf{r})$ and $\Omega(\mathbf{r})$ both modulate with \mathbf{q}_{SM}	93
Figure 5-6: Probability of occurrence of Δ and Ω as function of supermodulation phase ϕ	94

Figure 5-7: Supermodulation phase averaged local pairing gap and mode energy.....	96
Figure 5-8: Gap and mode energy modulation as function of periodic unit cell distortion.....	98
Figure 5-9: Oxygen isotope effect on $\bar{\Delta}(\phi)$ and $\bar{\Omega}(\phi)$	100
Figure 5-10: QPI for ^{16}O and ^{18}O optimal doped Bi-2212.....	103
Figure 5-11: Bogoliubov band minima \mathbf{k}_B for ^{16}O and ^{18}O isotopes.....	104
Figure 5-12: Doping dependence of chemical potential.....	105
Figure 5-13: Gap function for ^{16}O and ^{18}O isotope samples.....	106
Figure 5-14: Self consistency check for QPI fitting.....	107
Figure 5-15: DOS fit by $A(\mathbf{k}, \omega)$	111
Figure 5-16: Hypothetical inelastic tunneling path and spatial modulation in d^2I/dV^2	114
Figure 5-17: Examples of dI/dV and d^2I/dV^2 . The peak in d^2I/dV^2 diminishes as the gap size increases and peak height decreases.....	117
Figure 5-18: The spatial zero-displacement correlation coefficient as function of (a) modulation amplitude of Ω along supermodulation wavevector \mathbf{q}_{SM} , and (b) the correlation calculated from $\bar{\Delta}(\phi)$ and $\bar{\Omega}(\phi)$ defined by Equation (5-23).....	119
Figure 5-19: Universal relation between T_c and ρ_s taken from Ref. [128]. The muon- spin-relaxation rate σ is proportional to superfluid density ρ_s . In the underdoped regime, T_c of different families falls onto a straight line as function of σ , or superfluid density ρ_s	121
Figure 5-20: Prediction from Hubbard-Holstein model.....	123
Figure App.-1: Crystal structure of $\text{Ti-Sr}_3\text{Ru}_2\text{O}_7$	124
Figure App.-2: Metamagnetism in $\text{Sr}_3\text{Ru}_2\text{O}_7$. Taken from Ref. [132].....	125
Figure App.-3: The two diagonal component ρ_{aa} and ρ_{bb} of in-plane magnetoresistivity	

of a high purity $\text{Sr}_3\text{Ru}_2\text{O}_7$	126
Figure App.-4: Distance dependence of differential conductance. V_z is z-piezo voltage. The larger V_z corresponds to smaller tip-surface distance d . As d is reduced, two symmetric peaks around $\pm 10\text{mV}$ emerge.....	127
Figure App.-5: Fine structure inside unit cell.....	128
Figure App.-6: The spatial phase reversion of fine structure. Conductance map at energies around Ω_1 and Ω_2 . Equivalent unit cells are added together to increase S/N.....	129
Figure App.-7: Mode energy map. Ω_1 and Ω_2 are defined in Figure App.-5. It is obvious that the mode energy also exhibits the fine structures similar as that in dI/dV map.....	130
Figure App.-8: Distance dependence of mode energy around Ti impurity. The mode energy falls quickly to background value within a unit cell from Ti atom, and exhibits four-fold symmetry.....	131

LIST OF TABLES

Table 5-1: Fitting parameters for $\overline{\Omega}(\phi)$. The equation used to fit is

$$\overline{\Omega}(\phi) = C + A \cos(\phi - \vartheta) + B \cos[2(\phi - \vartheta)]. \quad \text{Amp.}/\overline{\Omega} \text{ is the relative peak-peak amplitude of the } \Omega \text{ modulation.....99}$$

Table 5-2: Doping dependence of chemical potential.....105

Table 5-3: Fitting parameters for $A(\mathbf{k}, \omega)$ 111

CHAPTER 1

Introduction to Low Temperature Scanning Tunneling Microscopy and Spectroscopic Imaging STM

In this introduction Chapter, the basics of Scanning Tunneling Microscopy (STM) and spectroscopic STM (SI-STM) will be discussed. Following that the experimental setup of the ultra-low vibration lab will be summarized. Some discussion will be given to noise reduction too.

1.1 Scanning Tunneling Microscopy

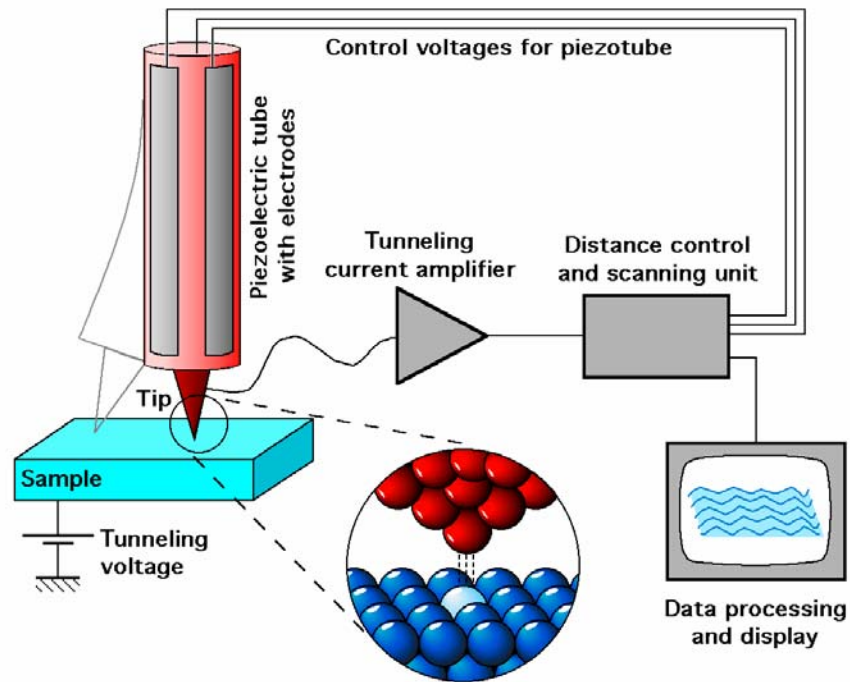


Figure 1-1 Schematic diagram of Scanning Tunneling Microscopy (STM).

Scanning tunneling microscopy (STM) was invented by Binnig and Rohrer [1] and first implemented by Binnig, Rohrer, Gerber and Weibel [2,3]. Since then STM has been a powerful probe to resolve local electronic structure in various conducting/semi-conducting material. The essential components of a STM is shown in Figure 1-1: an atomically sharp tip (usually Tungsten, Pt and PtIr tips are also used), scanner tube made of piezoelectric material, feedback system, coarse approaching mechanism, vibration isolation, data acquisition and analysis. When the tip is brought to the conducting surface within distance range of several Å, upon applying bias voltage between the tip and sample, quantum mechanical tunneling current starts to flow.

- Quantum mechanical tunneling

The schematic diagram of quantum mechanical tunneling between the tip and sample is shown in Figure 1-2. When there is no applied bias voltage, the net current between the tip and sample is zero. The bias voltage's main effect is to shift the relative Fermi levels of the tip and sample by amount eV . The explicit form of net elastic tunneling current is composed of two parts: the current from tip to sample $I_{t \rightarrow s}$, and current from sample to the tip $I_{s \rightarrow t}$. Such quantum mechanical tunneling is a result of wavefunction overlapping of tip and sample, not the electrical current driven by potential difference in circuit. $I_{t \rightarrow s}$ and $I_{s \rightarrow t}$ are non-vanishing if the tip surface separation is small enough so that the wavefunctions of tip and sample can have significant overlap. Upon applying positive bias voltage V on sample, and take the e as the absolute value of electron charge, the current flowing from tip to sample due to electrons of energy ε is written as:

$$I_{t \rightarrow s}(\varepsilon) = -2e \frac{2\pi}{\hbar} |M|^2 \{ \rho_t(\varepsilon - eV) f(\varepsilon - eV) \bullet \rho_s(\varepsilon) [1 - f(\varepsilon)] \} \quad (1-1)$$

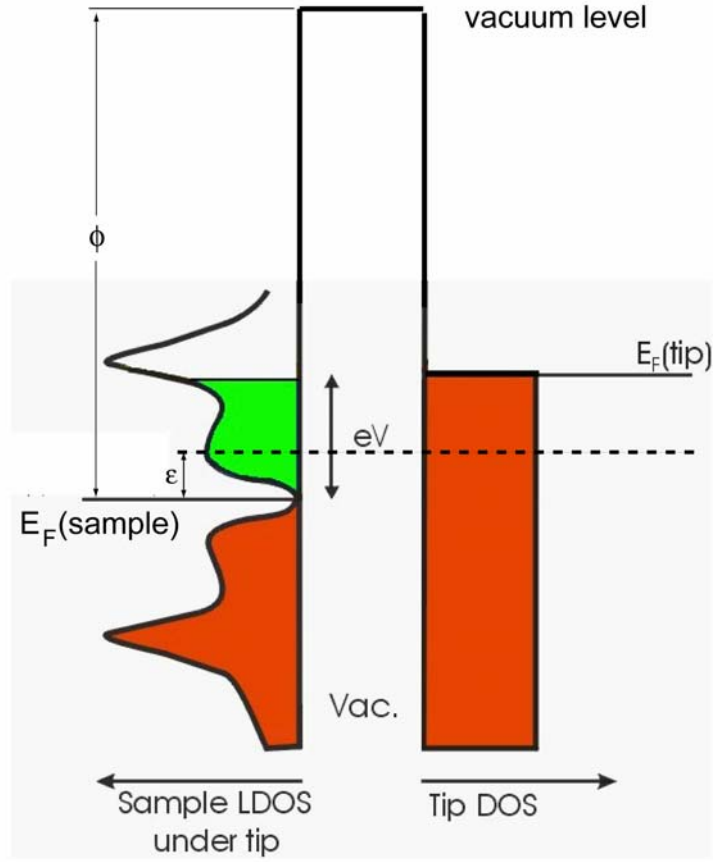


Figure 1-2 Schematics of quantum mechanical tunneling between tip and sample.

The Fermi level of sample is taken as zero energy. In Equation (1-1), $-2e$ accounts for electron of both spins, $|M|^2$ is the tunneling matrix elements, $2\pi/\hbar$ is from the Fermi's golden rule. The probability amplitude of transmitting electrons from tip to sample is constrained by: (1) the average occupation number of electrons in the states with energy ϵ in the tip $\rho_t(E_F - eV + \epsilon)f(E_F - eV + \epsilon)$, (2) the average number of vacant states with the same energy ϵ in the sample which the electron can tunnel into $\rho_s(E_F + \epsilon)[1 - f(E_F + \epsilon)]$. $f(E)$ is Fermi-Dirac distribution function

$$f(E) = \frac{1}{e^{(E-E_F)/k_B T} + 1} \quad (1-2)$$

At the same time, the current from the sample to the tip is:

$$I_{s \rightarrow t}(\varepsilon) = -2e \frac{2\pi}{\hbar} |M|^2 \{ \rho_t(\varepsilon - eV) [1 - f(\varepsilon - eV)] \bullet \rho_s(\varepsilon) f(\varepsilon) \} \quad (1-3)$$

The net current is then

$$I(\varepsilon) = I_{t \rightarrow s}(\varepsilon) - I_{s \rightarrow t}(\varepsilon) \quad (1-4)$$

After taking integral, it becomes

$$I = -2e \frac{2\pi}{\hbar} \int_{-\infty}^{+\infty} \rho_s(\varepsilon) \rho_t(\varepsilon - eV) [f(\varepsilon) - f(\varepsilon - eV)] d\varepsilon \quad (1-5)$$

The experiment runs at 4.2K, thermal broadening is $k_B T \approx 0.36 meV$. The Fermi function can be approximated by a sharp step function

$$f(E) = \begin{cases} 1 & (E < E_F) \\ 0 & (E > E_F) \end{cases} \quad (1-6)$$

Examining Equation (1-5), the only non-zero region of the integrand is $0 < \varepsilon < eV$. Next, we can simplify the integration by noticing density of states of W tip is approximately constant over the energy range we are interested in, i.e., $\sim -200mV$ to $\sim +200mV$. Therefore, we can take the tip density of states out of the integral and the current can be written as:

$$I = -\frac{4e\pi}{\hbar} \rho_t(E_F) \int_0^{eV} |M|^2 \rho_s(\varepsilon) d\varepsilon \quad (1-7)$$

- Tunneling matrix element

Bardeen [4] laid out the foundation for electron tunneling. The essential ingredients in Bardeen's transfer Hamiltonian approach are: (1) The two sides of the tunnel barrier can be treated as separate systems, (2) in the barrier, the many-body wave functions before and after electron transfer from one side to the other side are both good solutions, (3) the wavefunctions of the two sides decay exponentially in the tunnel barrier and quickly drop to zero on the other side, (4) time-dependent perturbation theory. Bardeen's tunneling theory shows that the tunneling matrix elements only depends on the wave function in the barrier, and has very little energy dependence (even in the normal to superconducting tunneling case). That means we can take out the tunneling matrix elements and write the final form for total current as

$$I = -\frac{4e\pi}{\hbar} \rho_t(0) |M|^2 \int_0^{eV} \rho_s(\varepsilon) d\varepsilon \quad (1-8)$$

After taking derivative, the differential conductance dI/dV is proportional to the local density of states:

$$\frac{dI}{dV}(V) \propto \rho_s(\varepsilon = eV) \quad (1-9)$$

Next, some discussion about tunneling matrix elements will be given. According to Bardeen's theory, the tunneling matrix elements $|M|$ is due to the overlapping of wave functions in the junction. The tunneling matrix element is given by:

$$M = \frac{\hbar}{2m_e} \int_{\text{surface}} (\varphi_t^* \frac{\partial \varphi_s}{\partial z} - \varphi_s^* \frac{\partial \varphi_t}{\partial z}) dS \quad (1-10)$$

where the integral is taken on the separation surface between two electrodes (in the original break junction experiment). M represents amplitude of electron transfer from sample to the tip or verse versa and is symmetric for both directions. The wave functions of tip and sample both decay exponentially in the tunneling barrier, and can be described by WKB approximation:

$$\varphi \sim C e^{-\int_{z=0}^{z_0} |p_z| dz} \quad (1-11)$$

Where the momentum p_z inside the tunneling junction is

$$p_z = \frac{\sqrt{2m_e(U(z) - E)}}{\hbar} \quad (1-12)$$

$U(z)$ is the barrier height (in 1D case) in the tunneling barrier and E is the energy of electrons and within the range of bias voltage eV . In the experiments concerned in this dissertation, normally we work in the range of about $\pm 200\text{mV}$. $U(z)$ is determined by work function ϕ and is usually a few eV , hence $E \ll \phi$. In reality, the barrier is not perfect rectangular shape, but comparing to the height of several eV , we can treat $U(z)$ as constant and use work function $U(z) = \phi$. From Equation (1-10), the surface integration will not change the exponential dependence of the tunneling amplitude. By taking square, one gets

$$|M|^2 \propto e^{-2\kappa z} \quad (1-13)$$

where

$$\kappa = \frac{\sqrt{2m_e\phi}}{\hbar} \quad (1-14)$$

In turn, the tunneling current is dependent on distance by the relation:

$$I = Ce^{-2\frac{\sqrt{2m_e\phi}}{\hbar}z} \int_0^{eV} \rho_s(\varepsilon) d\varepsilon \quad (1-15)$$

The matrix elements determine the STM's sensitivity with respect to change of tip-surface separation. Take the typical work function $\phi \approx 3-4\text{ eV}$, the current decays by $e^2 \approx 7.4$ times per Å. The bigger the work function is, the more sensitive the current response will be. This extremely sensitive response of current to distance change gives STM unparalleled advantage in studying electronic structure at nanometer scale. Another application of this relation is to determine the quality of tip after each field emission. Normally after one or two field emissions, the Au surface is quite clean. Since Au is such a good metal (with $\phi \sim 4-5\text{ eV}$), the measured I - V curve on Au surface after field emission is mainly determined by the tip. By measuring the distance dependent current $I(z)$, one can extract the work function (actually some mixture of tip and sample) by taking the logarithmic derivative:

$$\phi = \frac{\hbar^2}{8m_e} \left(\frac{d \ln I}{dz} \right)^2 \approx 0.95 \left(\frac{d \ln I}{dz} \right)^2 eV \quad (1-16)$$

Usually a work function around 3 eV is regarded as one of the indicators of a good tip.

Regarding the spatial resolution of STM, it is also constrained by the electronics. The tip is held at the end of a piezo tube scanner, the electrode outside is divided into 4 quadrants ($\pm x, \pm y$) and along z direction, there is a single piece electrode inside the

scanner tube. The lateral and vertical motion of the tip is controlled precisely by varying the voltage applied to the piezo. The DAC converter used is 16-bit, and the scanner voltage range (for all three directions) is $\pm 220\text{V}$. The lateral scan range is about 200nm , which gives lateral spatial resolution about $200\text{nm}/2^{16} \sim 0.03\text{\AA}$. The full vertical extension is $\sim 550\text{nm}$, with resolution $550\text{nm}/2^{16} \sim 0.08\text{\AA}$. In vertical direction, the noise due to DAC resolution is $440\text{V}/2^{16} \sim 6.7\text{mV}$.

1.2 Spectroscopic Imaging STM

The most basic operation mode of STM is constant-current topographic mode. In this mode, the sample bias voltage is kept constant at V_s (set bias, usually negative in our experiment), when the tip travels line by line on the surface, the feedback loop controls the tip-surface distance z to maintain the constant tunneling current I_s . By recording the relative height change of the tip, one will get an image of “surface height”.

From Equation (1-15), the tunneling current is mainly determined by two factors: the exponential dependence on distance and integrated LDOS from Fermi level to the set bias eV_s . If the LDOS is strictly identical from point to point, then it is true that the change of tip height represents the true surface height (relative). However, LDOS is especially disordered at nanoscale in the cuprate, so the recorded tip height change in topograph does not completely represent the true structural corrugation. On the other hand, the topograph does not represent the total local charge density either. The total charge should be the integration from Fermi level to infinity, but the topograph only includes the integrated LDOS up to some energy around the Fermi level. In the main material studied in this dissertation, $\text{Bi}_2\text{Sr}_2\text{CaCu}_2\text{O}_{8+\delta}$ (Bi-2212), the integrated LDOS is shown to be quite uniform if the integration is taken up to $\pm 600\text{mV}$. Even though

there is ambiguity in the term “surface corrugation” in topograph, it does show periodic structure which has the correct dimension as unit cell, both from real space and from Fourier transformed image. And especially in BSCCO family, the incommensurate crystalline modulation (supermodulation) is also observed clearly in topograph, with modulation periodicity consistent with that reported from X-ray study. These empirical facts show that most of the contribution to the variation of tip height in topograph does come from the structural corrugation.

To distinguish between the electronic and structural contribution to topographic feature experimentally, a simple way is to take the topograph at sequence of different bias voltages. If the feature does not change with bias voltage, then it is mainly structural; if it is bias dependent, then it is mainly electronic.

It is more important in terms of physics to get information about LDOS, rather than the integrated LDOS. As seen in Equation (1-15), if take derivative respect to bias voltage, differential conductance is proportional to LDOS. According to the convention of the past publication, we use $g(V)$ to mark the differential conductance:

$$g(V) \equiv \frac{dI}{dV}(V) \propto e^{-z/z_0} \rho_s(eV) \quad (1-17)$$

where $z_0 = \frac{\hbar}{2\sqrt{2m_e\phi}}$. If we can keep the tip-surface distance z constant and measure the differential conductance as function of (x, y, V) , then we can get three-dimensional dataset, which contains spatial and energy dependence of LDOS, which is usually called LDOS map and labeled by $g(\mathbf{r}) \equiv \frac{dI}{dV}(\mathbf{r})$. In reality, there is no way we can exactly know the tip-surface distance. The usual practice is to take point spectrum at

each point with the same set up voltage and current and feedback turned off. To the first order, topographic corrugation is largely removed.

Now some discussion about spatial and energy resolution. As will be discussed later on, the coherence length in BSCCO is very short, $\xi \sim 10 - 20 \text{ \AA}$ (over this distance, the LDOS, superconducting gap size etc. does not change significantly). To resolve the change in electronic structure at nanometer scale, one has to take LDOS map with high spatial resolution. The usual practice is to keep the spatial resolution about $2 \text{ \AA}/\text{pixel}$ (*i.e.* about 2 sample points per unit cell).

Conductance is measured by standard lock-in method. A small voltage modulation (generated by lock-in amplifier), usually with modulation frequency $f \sim 1 \text{ kHz}$ is added to the DC bias voltage and sent to the sample. The response current is amplified by low noise current amplifier and then fed into lock-in amplifier. dI/dV is measured as the ratio of response amplitude of current at modulation frequency to the amplitude of input modulation. This process will be discussed in detail in Chapter 3. The thermal smear at 4.2K is about 0.36meV, and the most important feature in BSCCO (superconducting peak, electron-boson interaction) is of the energy range 20-80mV. Ideally the modulation voltage should be smaller than the intrinsic energy resolution, but it will reduce the signal to noise (S/N) if we only use sub mV modulation. In the real measurement, about 1-2mV RMS modulation is used ($\sim 5 \text{ mV}$ peak-peak amplitude).

1.3 Noise Consideration

For high precision measurement, noise reduction is at the heart of designing a system. STM is susceptible to both vibrational and electrical noise.

- Vibration isolation

The Lab at Cornell is designed with several layers of vibration isolation. The entire lab is in underground and is separated from the main building by impedance mismatch. Inside the experiment room, there is an acoustic isolation room (called sound room in this group) in which the experiment setup is encapsulated. The sound room and experiment sit on a 30-ton concrete block and floated by 6 air springs. The cryostat is supported by a triangular table which is floated again by 3 smaller air springs. The experiment table and the smaller air springs sit on three wooden tables which are filled with lead. Figure 1-3 shows the schematic vibration isolation and the real lab picture. The vibration noise is reduced to level of a few ng / \sqrt{Hz} at STM head.

- Electrical noise

Another source of noise is the electrical noise. One intrinsic and unavoidable noise is Johnson noise from the resistor of the current preamp. It turns out the Johnson noise is much smaller than the actual voltage noise we have in the output signal. The gain used in the experiment is 10^9 , the resistor used in the current amplifier is about $1\text{ G}\Omega$. The voltage noise spectral density is $0.13\sqrt{R}nV / \sqrt{Hz} \approx 4.1\mu V / \sqrt{Hz}$. The 3dB cutoff frequency of the current preamp used in the experiment is $\omega_0 = 3kHz$, assume one-pole low pass filtering, the effective noise bandwidth $\Delta f_N = \omega_0 / 4 = 0.75kHz$. The r.m.s. noise for this bandwidth is then about $110\mu V$, which corresponds to current noise $\sim 0.1pA$. The current noise we observe is about r.m.s. $5pA$, much larger than estimated Johnson noise.

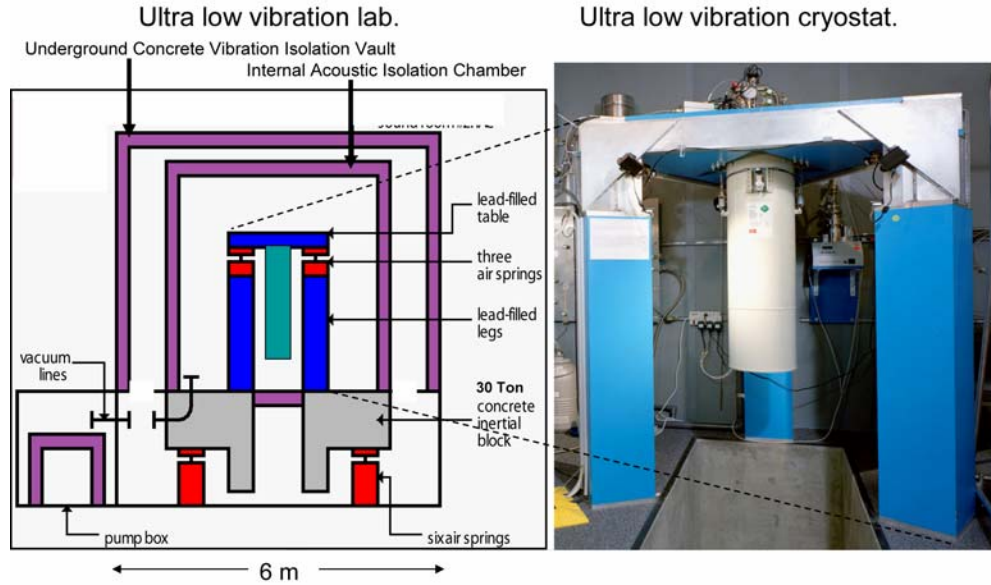


Figure 1-3 Ultra-low vibration lab at Cornell. Left: Diagram showing different stages of vibration isolation: 30-ton concrete block, acoustic isolation room, air springs. Right: Picture of real lab, with all the vibration isolation components linked to the diagram by dashed lines.

The current noise spectral density of STM can be summarized by Equation (1-18) [5]:

$$i_{total} = \sqrt{\left(\frac{e_n}{R_f}\right)^2 + i_n^2 + \frac{4k_B T}{R_f} + (2\pi C_{in} e_n)^2} \quad (1-18)$$

The symbols for different part of circuit are shown in Figure 1-4. The first term is the normal Ohmic current noise caused by input voltage noise of the op-amp. The second term is the intrinsic input current noise, and the third term is the Johnson noise, which is already discussed. The last term is the current noise due to capacitive coupling of the wires, and is the dominant source of current noise in STM. The wires running from room temperature to 4.2K usually have capacitance of $\sim 100\text{pF/m}$. The r.m.s. current noise is about 3pA in real operation. The most efficient to reduce the noise is to reduce the length of cables.

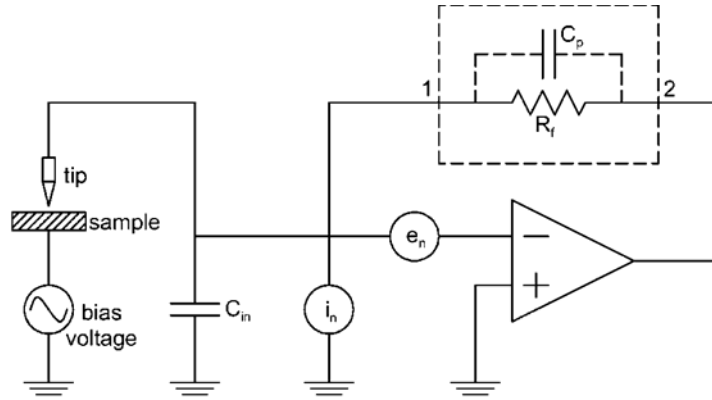


Figure 1-4 Circuit diagram of STM to model input noise. Taken from [5].

There is very good summary about other experimental techniques on Cuprate in J. E. Hoffman's thesis [6], and will not repeat here.

In summary, basic principles and spectroscopic imaging STM is introduced. Some discussion is given to noise consideration for high precision STM measurement.

CHAPTER 2

STM Study on Cuprates – the Past Measurement Paradigm

Over the past decade, STM study on Cuprate at atomic scale has been extremely productive. The novel measurement techniques developed in this group and accumulation of rich data make it possible now to test various hypotheses and to develop new analysis scheme to quantitatively understand microscopic behavior of this exotic material. In this chapter, several important measurement techniques and key results will be reviewed. Those are years of efforts made by previous generations of group members. In the context of this dissertation, focus is on optimally doped $\text{Bi}_2\text{Sr}_2\text{CaCu}_2\text{O}_{8+\delta}$ (Bi-2212). In this chapter, an overview of conventional BCS superconductivity and basics of high temperature superconductivity will be given first, followed by gap map, quasiparticle interference (QPI), and oxygen dopant map.

2.1 BCS Superconductivity

Superconductivity is one of the corner stones of 20th century physics, discovered in 1911 by H. Kamerlingh Onnes in Leiden [7]. The first hallmark of this new phase in condensed matter system is zero resistance below certain critical temperature. Later on, Meissner and Ochsenfeld [8] discovered the next signature of superconductivity, perfect diamagnetism in 1933. After the first discovery of superconductivity, several decades passed before the microscopic nature of traditional superconductivity was precisely described by **BCS** theory in 1957 [9]. The physical picture of **BCS** theory is as following: an electron, with negative charge $-e$, attracts positive ions as it moves inside the solid, therefore this lattice distortion locally induces excessive positive charge. This positive charge in turn attracts another electron, to form a pair with the first one. As long as this attractive interaction is stronger than that of Coulomb

interaction between the two electrons, superconductivity is created. The electron pair formed due to phonon mediation is called ‘Cooper pair’. Figure 2-1 shows the cartoon of this phonon-mediated process

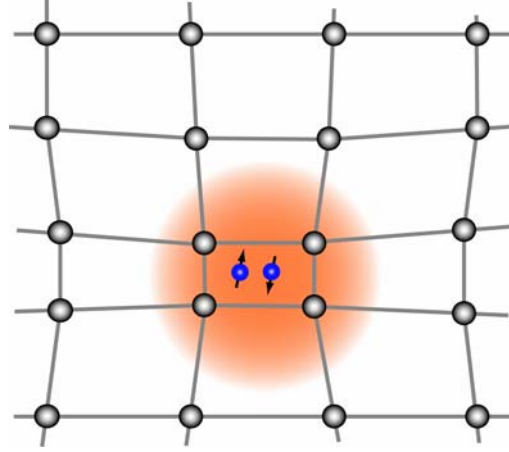


Figure 2-1 Cartoon of Cooper pair. Electrons with opposite spins and momenta moves without dissipation in solid at T=0K. The energy needed to break the pair is Δ , the superconducting gap energy.

Next, a brief review of BCS theory will be given [10]. The BCS ground state is written as:

$$|\psi_G\rangle = \prod_{k=k_1, \dots, k_M} (u_k + v_k c_{k\uparrow}^+ c_{-k\downarrow}^+) |\phi_0\rangle \quad (2-1)$$

where $|u_k|^2 + |v_k|^2 = 1$, $|\phi_0\rangle$ is vacuum. Use so called *reduced Hamiltonian* for the calculation:

$$H = \sum_{k, \sigma} \epsilon_k n_{k\sigma} + \sum_{k, k'} V_{kk'} c_{k\uparrow}^+ c_{-k\downarrow}^+ c_{-k'\downarrow} c_{k'\uparrow} \quad (2-2)$$

where only the Cooper term in the residual interaction is retained. It is the attractive interaction $V_{k, k'}$ which leads to the Fermi liquid instability.

The coefficients of the ground state is found by using variational method to minimize the expectation value of reduced Hamiltonian:

$$\delta \langle \psi_G | \sum_{k,\sigma} \epsilon_k n_{k\sigma} + \sum_{k,k'} V_{kk'} c_{k'\uparrow}^\dagger c_{-k\downarrow}^\dagger c_{-k\downarrow} c_{k'\uparrow} - \mu N | \psi_G \rangle = 0 \quad (2-3)$$

The key results from BCS theory and the important phenomenology for BCS superconductors are the followings:

- Gap Function

$$\Delta \approx 2\hbar\omega_0 e^{-1/N(0)V} \quad (2-4)$$

where Δ is s-wave superconducting gap, the cutoff frequency ω_0 is of order of Debye frequency ω_D , $N(0)$ is Fermi level density of states. At $T = 0K$, Δ is the energy required to break Cooper pair.

- Temperature Dependence of Gap

As temperature goes from 0 K towards T_c , $\Delta(T)/\Delta(T=0)$ decreases monotonically as function of T/T_c , due to thermal excitation of quasiparticles from the ground state. Note the following universality only holds for weak-coupling superconductor and when the temperature is very close and below T_c .

$$\frac{\Delta(T)}{\Delta(T=0)} \approx 1.74 \left(1 - \frac{T}{T_c}\right)^{1/2} (T \approx T_c) \quad (2-5)$$

- Isotope Effect

Historically, isotope effect played the central role to identify the importance of electron-lattice coupling in explaining superconductivity. It is first suggested by Fröhlich theoretically in 1950 [11]. In the same year, isotope effect in superconducting transition temperature T_c is confirmed experimentally in Mercury [12,13]. From BCS ratio $\frac{\Delta(T=0)}{k_B T_c} = 1.764$, gap is proportional to T_c , and from Equation (2-4), T_c is proportional to cutoff phonon frequency $\omega_0 \propto \sqrt{\frac{1}{M}}$. If replacing the ion by its isotope with different mass M , there will be a shift in T_c and the isotope coefficient

$$\alpha = -\frac{\Delta \ln(T_c)}{\Delta \ln(M)} \quad (2-6)$$

should exactly equal to 0.5. Note this result is only valid for a few classic weak-coupling superconductors. Right after the first discovery of high- T_c superconductivity in copper-oxides (cuprates), isotope effect was extensively studied. However, in Cuprates, isotope shift in T_c has complicated dependence on hole doping levels, number of CuO_2 layers, etc.. At optimal and overdoped side, the shift in T_c is vanishingly small and this is widely regarded as evidence against pure electron-phonon mechanism.

- Type I and Type II Superconductor

All superconductors exhibit diamagnetism. According to whether the diamagnetism is ‘perfect’, superconductors are classified into type I and type II. Type I superconductor shows perfect diamagnetism, as discovered by Meissner and Ochsenfeld [8]. Below T_c , a superconductor develops surface current and completely exclude external magnetic field if it does not exceed critical value H_c . Inside a bulk type I superconductor, net magnetic field is zero. At the surface, magnetic field rapidly

decays over a length called the penetration depth λ (usually about 500 Å typical pure superconductors). There is another important quantity, coherence length ξ in Ginzburg-Landau theory, which defines the distance the macroscopic order parameter $\psi(\mathbf{r})$ can vary without suffering energy loss. G-L theory contains an important ratio $\kappa = \frac{\lambda}{\xi}$. This ratio determines with increasing strength, how magnetic field penetrates a superconductor. If $\kappa < \frac{1}{\sqrt{2}}$, as for most pure superconductors, magnetization undergoes first-order transition at H_c . Superconductors with such behavior belong to type I. Superconductors with $\kappa > \frac{1}{\sqrt{2}}$ (Niobium and alloys) belong to type II. There are two critical fields for type II superconductor, H_{c1} and H_{c2} . Instead of breaking down superconductivity discontinuously as increasing field at H_{c1} , flux penetration increases continuously. Between H_{c1} and H_{c2} , flux penetrates with a regular triangle array pattern, forming ‘vortex lattice’, as predicted by Abrikosov [14]. Figure 2-2 shows the magnetization curves for the both cases.

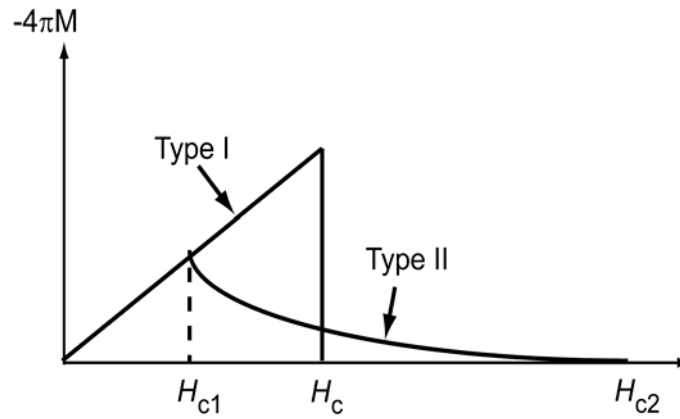


Figure 2-2 Magnetization of type I and type II superconductors. This schematic drawing shows the two types with the same thermodynamic critical field H_c . At H_c , type I undergoes first-order transition, superconductivity is discontinuously broken. At H_{c1} and H_{c2} , type II undergoes continuous transition.

2.2 Cuprate Superconductor: Basics

BCS theory predicts that the highest T_c is somewhere $\sim 30\text{K}$, or at most, $\sim 40\text{K}$ in strong coupling case [15]. The decades effort only achieved $T_c=23\text{K}$ in Nb_3Ge . After that it seemed there was no room for higher superconducting transition temperature. Then in 1986, J. D. Bednorz and K. A. Müller [16] found a superconducting copper-oxide, Ba doped La_2CuO_4 , with T_c as high as 30K . This discovery was so astonishing because the parent compound La_2CuO_4 is an antiferromagnetic insulator, but upon doping holes by substituting small percentage of La^{3+} for Ba^{2+} , the system quickly moves to superconducting phase. The discovery of LBCO triggered the tremendously active research on superconductivity. In 1987, C. W. Chu and colleague [17] discovered $\text{YBa}_2\text{Cu}_3\text{O}_{7-\delta}$, with $T_c=93\text{K}$, the first superconductor with transition temperature above liquid nitrogen temperature 77K . This criterion is practically important, since cooling by liquid nitrogen is orders of magnitudes cheaper than the techniques required to cool material below 77K . Many new families of high T_c superconductors have been discovered, rewriting the record for highest T_c . Most of those materials share the similar layered structure, all containing with CuO_2 planes separated by other layers of various compositions. Superconductivity is widely believed to occur in CuO_2 planes, while other layers mainly act as charge reservoir. Figure 2-3 shows the structure of three main families of hole doped Cuprates. Depending on whether the charge reservoir layers supply holes or electrons to CuO_2 plane, Cuprates are categorized as electron doped and hole doped, both share similar phase diagram. When talking about high temperature superconductor, one often refers to copper-oxides and much effort have been focused on copper-related compounds. Maeno *et al.* [18] discovered in 1994 the $4d$ transition metal Ru also forms an unconventional superconductor, Ru_2SrO_4 (first reported $T_c=0.93\text{K}$), with similar

perovskite structure as Cuprate but p -wave pairing symmetry. This discovery demonstrates that copper is not the necessary element to form superconductivity in layered perovskite. However, the highest T_c is still maintained in copper oxides. This fact tells us copper must have some special role in achieving high T_c . Recently, another transition metal oxide joined the high- T_c family. Layered Fe-based compound shows superconductivity with $T_c=26\text{K}$ in $\text{LaO}_{1-x}\text{F}_x\text{FeAs}$ [19], 41K in $\text{CeO}_{1-x}\text{F}_x\text{FeAs}$ [20] and 43K in $\text{SmO}_{1-x}\text{F}_x\text{FeAs}$ [21]. Active research efforts are being made to investigate the mechanism at the time this thesis is being written.

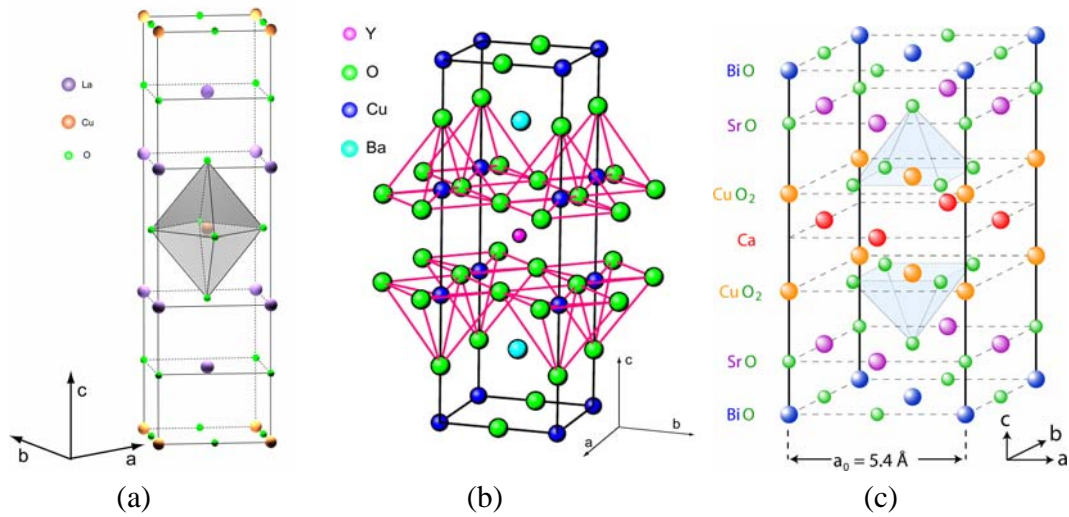


Figure 2-3 Crystal structure of three most important hole doped Cuprates.
(a) $\text{La}_{2-x}\text{A}_x\text{CuO}_4$. Where A can be Ba, Sr, Ca. . . (b) $\text{YBaCu}_3\text{O}_{7-\delta}$. (c) $\text{Bi}_2\text{Sr}_2\text{CaCu}_2\text{O}_{8+\delta}$.

Cuprate has extremely complicated phase space, and its properties are controlled by multiple tuning parameters which will be discussed briefly below. Those include, but not limited to, doping level (carrier concentration), chemical disorder and layer number.

- Charge Transfer Insulator

The parent compounds of Cuprates are charge transfer Mott insulator. Each Cu is in $2+$ valence state and is singly occupied by one electron (or one hole), with the spin of electrons (holes) of nearest neighboring sites antiparalleled, the undoped compound is antiferromagnetic (AF). The on site coulomb repulsion U is as large as $6-8eV$, hence double occupancy is not energetically favorable. Figure 2-4 shows the basic energy level of Cu^{2+} and O^{2-} of HTSC cuprates. There is one electron in $3d_{x^2-y^2}$ orbital of copper, and two electrons occupying oxygen $2p$ orbital. There is another important energy scale, charge transfer gap Δ_{CT} , which is the energy needed to excite one electron from oxygen $2p$ orbital to Cu $3d_{x^2-y^2}$ orbital. Δ_{CT} is $\sim 2-3eV$ for cuprates and much smaller than U . Depending on whether $\Delta_{CT} < U$ or $\Delta_{CT} > U$, the material is called *charge transfer insulator* or *Mott-Hubbard insulator*.

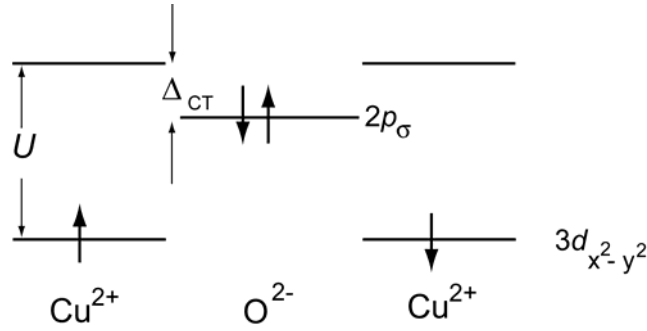


Figure 2-4 Scheme of relative energy levels for Cu and O ions in HTSC cuprates, adopted from S. Maekawa [22]. Arrows are electrons with spin $1/2$.

The antiferromagnetic interaction between electron spins on copper site is mediated by in-plane oxygens, called the *superexchange*. The effective superexchange is written as

$$J = \frac{4t_{pd}^4}{\Delta_{CT}^2} \left(\frac{1}{\Delta} + \frac{1}{U} \right) \quad (2-7)$$

J is of the order ~ 0.1 to 0.2 eV and is believed to be directly proportional to d -wave superconducting gap Δ_k [23] in RVB type of theory. This is a very important hypothesis to test. I have made some serious efforts, with Dr. Jinho Lee, to try to use STM to image local charge transfer gap and d -wave gap at the identical field of view, in the hope of finding out whether there is any correlation between the two quantities. However, due to the high voltage, surface and/or tip are exploded at every attempt. Despite the technical difficulty, this experiment has its fundamental importance and should always be kept in mind.

- Pairing Symmetry

The Symmetry of order parameter in cuprates is one of the most important topics in cuprate research. There is abundant evidence that the pairing symmetry in hole doped cuprates is $d_{x^2-y^2}$. However, in electron doped case the symmetry is still controversial. Following I summarize some important experimental evidence for d -wave symmetry in hole doped cuprates.

1. Phase sensitive measurement performed by SQUID on YBCO [24,25].
2. The relaxation rate of Cu probed by NMR below T_c varies as T^3 , which is consistent with predictions for $d_{x^2-y^2}$ order parameter.
3. Penetration depth measurement on single crystal YBCO [26,27] reveals linear dependence of λ on T . This is consistent with the prediction for a superconductor with a node presenting in the superconducting order parameter. On the other hand, for an s -wave superconductor, the BCS theory

gives exponential dependence of penetration depth on temperature as a consequence of s -wave energy gap.

4. Angle-resolved photoemission spectroscopy (ARPES) reveals an strongly anisotropic superconducting gap consistent $d_{x^2-y^2}$ symmetry [28].

- Charge Carriers in Cuprates

Charge carrier in superconducting cuprates is bonded electron pair of charge $2e$. This is demonstrated unambiguously by Shapiro steps in Josephson tunneling junction. The steps have size of $h\nu/2e$. Also the flux quanta is directly measured to be $hc/2e$ [29,30]. This $2e$ pairing is a direct evidence that some believes explanation of high T_c is some variant version of BCS theory.

- Doping Dependence

Hole concentration is the leading order controlling factor of T_c within the same material. Doping extra holes to CuO_2 can be achieved by (1) substituting trivalent La for divalent elements like Ba, Sr, Ca..., in parent compound La_2CuO_4 , or (2) varying non-stoichiometric oxygen content, like in $\text{YBa}_2\text{Cu}_3\text{O}_{7-\delta}$, $\text{Tl}(\text{Bi})_n\text{Sr}_n\text{Ca}_{n-1}\text{Cu}_n\text{O}_{2n+4+\delta}$. Figure 2-5 shows the schematic phase diagram for hole doped cuprates. With no doping, the parent compounds are AF insulators. With just about 3-5% doping (holes per Cu site), AF order is quickly suppressed and at low temperature, the system moves into superconducting state starting from about 6% to about 25% hole concentration. As a function of doping, the superconducting critical temperature T_c is dome shaped, described by some universal empirical formula [31]:

$$\frac{T_c}{T_{c,\max}} = 1 - 82.6(p - 0.16)^2 \quad (2-8)$$

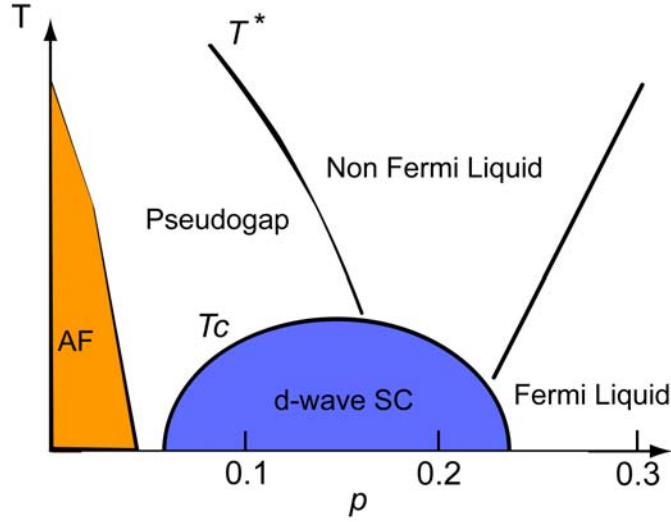


Figure 2-5 Schematic phase diagram for hole doped cuprates.

This relation characterizes LSCO family, YBCO and BSCCO family. The optimal doping is about 16% where maximal T_c is achieved. Above superconducting dome, cuprates exhibit various exotic properties. In underdoped region, there is a cross-over temperature T^* . Below T^* the density of states near Fermi level is gradually depleted, forming a “pseudogap” [32]. The pseudogap possesses $d_{x^2-y^2}$ symmetry and is viewed from two completely different views: one views pseudogap as a real paired state but lacking of coherence, the other one views pseudogap as an order competing with superconductivity. There is another unusual region in the phase diagram. Above the superconducting dome around optimal doping, the normal state in plane resistivity is linear in temperature $\rho_{ab} \sim T$, rather than the conventional Fermi liquid result for normal metal $\rho_{ab} \sim T^2$. Hall coefficient is temperature dependent. This region is called this non-Fermi liquid (NFL). Increasing doping furthermore, the normal state gradually restores T^2 dependence of resistivity as for normal Fermi liquid. It is worthwhile to mention a few words about electron doped cuprates. In electron

doped case, the AF correlation is much stronger than hole doped cuprates. AF phase extends up to much higher doping level and the superconductivity exists within a much narrower doping range. Also T_c is much lower in electron doped cuprates.

- Layer Number Dependence of $T_{c, \max}$

Another remarkable feature of Cuprate is that within a same family, $T_{c, \max}$ at optimal doping scales with number of CuO_2 layers. For example [33], in Mercury based cuprate $\text{HgBa}_2\text{Ca}_{n-1}\text{Cu}_n\text{O}_{2n+2+\delta}$, T_c increases with increasing layer number n until $n=3$, then gradually decreases with further increasing layer number. The distance between charge reservoir layer and CuO_2 plane is found to be critical to superconducting properties in epitaxial cuprate films [34]. This leads to the recognition that although superconductivity exists in CuO_2 plane, the interlayer hopping is an essential parameter to control $T_{c, \max}$ [35].

- Chemical Disorder and Superconductivity

Cuprate is characterized by large variety of chemical disorders, which greatly affect T_c . Two examples will be used for the short discussion. Eisaki *et al.* [36] has a very detailed categorization of different patterns of disorders. These include: (1) Bi:Sr non-stoichiometry in Bi2212 and Bi2201, Sr^{2+} substitution for La^{3+} in La_2CuO_4 and replacing Sr^{2+} by trivalent Ln^{3+} , (2) Y^{3+} replacing Ca^{2+} in Bi2212, (3) disorder that is far away from CuO_2 plane, this type includes excessive oxygen δ in Bi and Tl based cuprates, oxygen deficiency in CuO chain in YBCO etc. See Figure 2-6 for the positions of various disorders. The different types of disorders affect T_c through different possible mechanism. For example, in type (3), hole doping is partly controlled by excessive oxygen, and so is T_c ; out-of- plane effect induced by type (1) disorder affects T_c . K. Fujita *et al.* [37] showed T_c varies substantially as function of

ion radii when substituting Sr^{2+} for Ln^{3+} in Bi2201 and concentration of Nd^{3+} impurity on La site in LSCO. The effect is attributed to local lattice distortion and consequently the change of hopping parameters.

Halogen Family	Bi Family			
Pb Family	1L Ti Family			
La Family	2L Family			
YBCO Family	Hg Family			

(1)	(a-1)		(c-1)																						
	<table><tr><td>T_c</td><td></td></tr><tr><td>$\text{Ca}_{2-x}\text{Na}_x\text{CuO}_2\text{Cl}_2$</td><td>26</td></tr><tr><td>$\text{Pb}_2\text{Sr}_{2-x}\text{La}_x\text{Cu}_2\text{O}_z$</td><td>33</td></tr><tr><td>$\text{La}_{2-x}\text{M}_x\text{CuO}_4$</td><td>39</td></tr><tr><td>$\text{Bi}_2\text{Sr}_{1-x}\text{Ln}_x\text{CuO}_{6+\delta}$</td><td>38</td></tr><tr><td>$\text{TlBa}_{1+x}\text{La}_{1-x}\text{CuO}_5$</td><td>45</td></tr></table>	T_c		$\text{Ca}_{2-x}\text{Na}_x\text{CuO}_2\text{Cl}_2$	26	$\text{Pb}_2\text{Sr}_{2-x}\text{La}_x\text{Cu}_2\text{O}_z$	33	$\text{La}_{2-x}\text{M}_x\text{CuO}_4$	39	$\text{Bi}_2\text{Sr}_{1-x}\text{Ln}_x\text{CuO}_{6+\delta}$	38	$\text{TlBa}_{1+x}\text{La}_{1-x}\text{CuO}_5$	45		<table><tr><td>T_c</td><td></td></tr><tr><td>$\text{Sr}_2\text{CuO}_2\text{F}_{2+x}$</td><td>46</td></tr><tr><td>$\text{La}_2\text{CuO}_{4+\delta}$</td><td>45</td></tr><tr><td>$\text{Ti}_2\text{Ba}_2\text{CuO}_{6+\delta}$</td><td>93</td></tr><tr><td>$\text{HgBa}_2\text{CuO}_{4+\delta}$</td><td>98</td></tr></table>	T_c		$\text{Sr}_2\text{CuO}_2\text{F}_{2+x}$	46	$\text{La}_2\text{CuO}_{4+\delta}$	45	$\text{Ti}_2\text{Ba}_2\text{CuO}_{6+\delta}$	93	$\text{HgBa}_2\text{CuO}_{4+\delta}$	98
T_c																									
$\text{Ca}_{2-x}\text{Na}_x\text{CuO}_2\text{Cl}_2$	26																								
$\text{Pb}_2\text{Sr}_{2-x}\text{La}_x\text{Cu}_2\text{O}_z$	33																								
$\text{La}_{2-x}\text{M}_x\text{CuO}_4$	39																								
$\text{Bi}_2\text{Sr}_{1-x}\text{Ln}_x\text{CuO}_{6+\delta}$	38																								
$\text{TlBa}_{1+x}\text{La}_{1-x}\text{CuO}_5$	45																								
T_c																									
$\text{Sr}_2\text{CuO}_2\text{F}_{2+x}$	46																								
$\text{La}_2\text{CuO}_{4+\delta}$	45																								
$\text{Ti}_2\text{Ba}_2\text{CuO}_{6+\delta}$	93																								
$\text{HgBa}_2\text{CuO}_{4+\delta}$	98																								

(2)	(a-2)	(b-2)	(c-2)																										
 	 <table><tr><td>T_c</td><td></td></tr><tr><td>$\text{La}_{2-x}\text{Sr}_x\text{CaCu}_2\text{O}_6$</td><td>60</td></tr><tr><td>$(\text{La}_{1-x}\text{Ca}_x)(\text{Ba}_{1.75-x}\text{La}_{0.25+x})\text{Cu}_3\text{O}_y$</td><td>80</td></tr><tr><td>$\text{Bi}_{2+x}\text{Sr}_{2-x}\text{CaCu}_2\text{O}_{8+\delta}$</td><td>90</td></tr></table>	T_c		$\text{La}_{2-x}\text{Sr}_x\text{CaCu}_2\text{O}_6$	60	$(\text{La}_{1-x}\text{Ca}_x)(\text{Ba}_{1.75-x}\text{La}_{0.25+x})\text{Cu}_3\text{O}_y$	80	$\text{Bi}_{2+x}\text{Sr}_{2-x}\text{CaCu}_2\text{O}_{8+\delta}$	90	 <table><tr><td>T_c</td><td></td></tr><tr><td>$\text{Pb}_2\text{Sr}_2\text{Y}_{1-x}\text{Ca}_x\text{Cu}_3\text{O}_{8+\delta}$</td><td>80</td></tr><tr><td>$\text{Y}_{1-x}\text{Ca}_x\text{Ba}_2\text{Cu}_3\text{O}_{7-\delta}$</td><td>90</td></tr><tr><td>$\text{Bi}_2\text{Sr}_2\text{Ca}_{1-x}\text{Y}_x\text{Cu}_3\text{O}_{8+\delta}$</td><td>96</td></tr></table>	T_c		$\text{Pb}_2\text{Sr}_2\text{Y}_{1-x}\text{Ca}_x\text{Cu}_3\text{O}_{8+\delta}$	80	$\text{Y}_{1-x}\text{Ca}_x\text{Ba}_2\text{Cu}_3\text{O}_{7-\delta}$	90	$\text{Bi}_2\text{Sr}_2\text{Ca}_{1-x}\text{Y}_x\text{Cu}_3\text{O}_{8+\delta}$	96	 <table><tr><td>T_c</td><td></td></tr><tr><td>$\text{YBa}_2\text{Cu}_3\text{O}_{7-\delta}$</td><td>93</td></tr><tr><td>$\text{TlBa}_2\text{CaCu}_2\text{O}_{7+\delta}$</td><td>110</td></tr><tr><td>$\text{Ti}_2\text{Ba}_2\text{CaCu}_2\text{O}_{8+\delta}$</td><td>110</td></tr><tr><td>$\text{HgBa}_2\text{CaCu}_2\text{O}_{6+\delta}$</td><td>120</td></tr></table>	T_c		$\text{YBa}_2\text{Cu}_3\text{O}_{7-\delta}$	93	$\text{TlBa}_2\text{CaCu}_2\text{O}_{7+\delta}$	110	$\text{Ti}_2\text{Ba}_2\text{CaCu}_2\text{O}_{8+\delta}$	110	$\text{HgBa}_2\text{CaCu}_2\text{O}_{6+\delta}$	120
T_c																													
$\text{La}_{2-x}\text{Sr}_x\text{CaCu}_2\text{O}_6$	60																												
$(\text{La}_{1-x}\text{Ca}_x)(\text{Ba}_{1.75-x}\text{La}_{0.25+x})\text{Cu}_3\text{O}_y$	80																												
$\text{Bi}_{2+x}\text{Sr}_{2-x}\text{CaCu}_2\text{O}_{8+\delta}$	90																												
T_c																													
$\text{Pb}_2\text{Sr}_2\text{Y}_{1-x}\text{Ca}_x\text{Cu}_3\text{O}_{8+\delta}$	80																												
$\text{Y}_{1-x}\text{Ca}_x\text{Ba}_2\text{Cu}_3\text{O}_{7-\delta}$	90																												
$\text{Bi}_2\text{Sr}_2\text{Ca}_{1-x}\text{Y}_x\text{Cu}_3\text{O}_{8+\delta}$	96																												
T_c																													
$\text{YBa}_2\text{Cu}_3\text{O}_{7-\delta}$	93																												
$\text{TlBa}_2\text{CaCu}_2\text{O}_{7+\delta}$	110																												
$\text{Ti}_2\text{Ba}_2\text{CaCu}_2\text{O}_{8+\delta}$	110																												
$\text{HgBa}_2\text{CaCu}_2\text{O}_{6+\delta}$	120																												

(3)	(a-3)	(b-3)	(c-3)																		
 	 <table><tr><td>T_c</td><td></td></tr><tr><td>$\text{Bi}_{2+x}\text{Sr}_{2-x}\text{Ca}_2\text{Cu}_3\text{O}_{10+\delta}$</td><td>110</td></tr><tr><td>$\text{TlBa}_{2-x}\text{Ca}_2\text{Cu}_3\text{O}_{9+\delta}$</td><td>123</td></tr></table>	T_c		$\text{Bi}_{2+x}\text{Sr}_{2-x}\text{Ca}_2\text{Cu}_3\text{O}_{10+\delta}$	110	$\text{TlBa}_{2-x}\text{Ca}_2\text{Cu}_3\text{O}_{9+\delta}$	123	 <table><tr><td>T_c</td><td></td></tr><tr><td>$\text{TlBa}_2\text{Ca}_{2-x}\text{Cu}_3\text{O}_{9+\delta}$</td><td>131</td></tr></table>	T_c		$\text{TlBa}_2\text{Ca}_{2-x}\text{Cu}_3\text{O}_{9+\delta}$	131	 <table><tr><td>T_c</td><td></td></tr><tr><td>$\text{TlBa}_2\text{Ca}_2\text{Cu}_3\text{O}_{9+\delta}$</td><td>133</td></tr><tr><td>$\text{Ti}_2\text{Ba}_2\text{Ca}_2\text{Cu}_3\text{O}_{10+\delta}$</td><td>125</td></tr><tr><td>$\text{HgBa}_2\text{Ca}_2\text{Cu}_3\text{O}_{10+\delta}$</td><td>135</td></tr></table>	T_c		$\text{TlBa}_2\text{Ca}_2\text{Cu}_3\text{O}_{9+\delta}$	133	$\text{Ti}_2\text{Ba}_2\text{Ca}_2\text{Cu}_3\text{O}_{10+\delta}$	125	$\text{HgBa}_2\text{Ca}_2\text{Cu}_3\text{O}_{10+\delta}$	135
T_c																					
$\text{Bi}_{2+x}\text{Sr}_{2-x}\text{Ca}_2\text{Cu}_3\text{O}_{10+\delta}$	110																				
$\text{TlBa}_{2-x}\text{Ca}_2\text{Cu}_3\text{O}_{9+\delta}$	123																				
T_c																					
$\text{TlBa}_2\text{Ca}_{2-x}\text{Cu}_3\text{O}_{9+\delta}$	131																				
T_c																					
$\text{TlBa}_2\text{Ca}_2\text{Cu}_3\text{O}_{9+\delta}$	133																				
$\text{Ti}_2\text{Ba}_2\text{Ca}_2\text{Cu}_3\text{O}_{10+\delta}$	125																				
$\text{HgBa}_2\text{Ca}_2\text{Cu}_3\text{O}_{10+\delta}$	135																				

Figure 2-6 Summary of disorder types of different cuprate families.
In courtesy of Eisaki *et al.* [36]

2.3 STM on Cuprate

The layered structure of cuprate provides natural cleavage planes and makes this family of materials ideal for surface sensitive probes like ARPES and STM. The material can be cleaved in UHV or low temperature ultra-vacuum and reveal a perfect flat surface to study. However, for STM, up to now, there are only two cuprate families which yield high quality data. One is BSCCO family, another is $\text{Ca}_{2-x}\text{Na}_x\text{CuO}_2\text{Cl}_2$. This dissertation will focus on double layered BSCCO, Bi2212. In Bi2212, the weakest link in the layered structure is between two adjacent BiO layers (See Figure 2-7). From crystal grower's point of view, between the charge neutral layers is the easiest place to cleave the crystal.

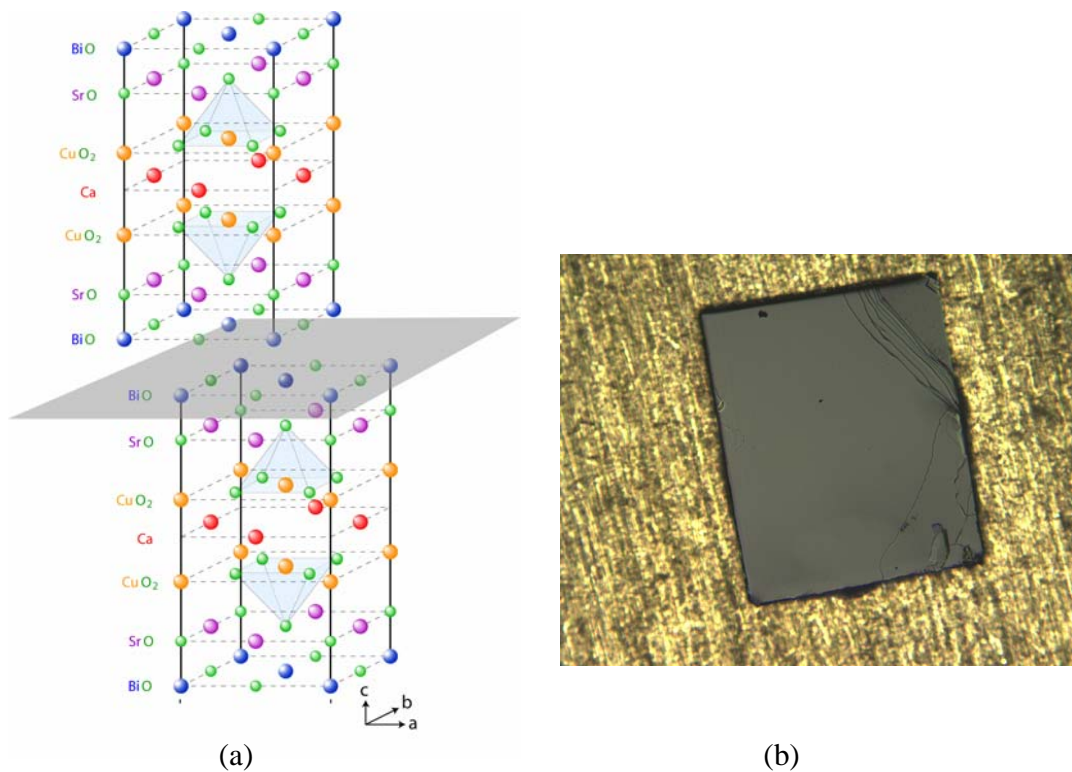


Figure 2-7 Cleaving of Bi-2212 crystal. (1) The crystal naturally cleaves between two BiO layers. (2) Cleaved surface of Pb-doped Bi2212 (OD65K).

In practice, the cleaving is done in the following steps:

- (1) Carefully select a crystal of size about 1mmx1mm, no thicker than 0.7mm. If necessary, should cut it either along *a-b* plane or *c* axis to the right size. If the sample is too thick, it will have the risk to crash to tip during the insertion. (This is usually a concern for thick samples like YBCO)
- (2) Paint a thin layer of silver epoxy (H20E) on the brass sample stud, make it the similar shape and size as the sample.
- (3) Use vacuum tweezers to place the sample on the painted glue, try to align with the painted glue pattern on the sample stud then push down gently. Bake the sample in the oven at 80°C for 90 minutes.
- (4) Take out sample. Under the optical microscope, use scotch tape to carefully remove any flaky part of the sample. Put a small drop of glue at the center of the sample. Prepare a brass or aluminum rod, with about 1mm diameter, sand the end to make it flat. Put a thin layer of glue at the flat surface. Then carefully use tweezers to stand the rod on the sample, the end with glue should match with the top surface of sample. Use tweezers to gently push the rod down. Make the rod stand as vertical as possible.
- (5) Bake for another 90 minutes.
- (6) Insert the sample into the fridge. Cool the sample just above the 4K plate key hole for about 4 hours. Do not touch the 4K plate during initial cooling as to avoid thermal shock to the sample.
- (7) Quickly cleave the sample and insert into STM head.

During the whole process, there are a few *possible pitfalls*. (1) The cleaving rod is too tilted after being glued on the sample. This may lead to some unexpected trouble. For example, the rod may not be knocked out when the cleaver is actuated. (2) There is a Teflon guide which grabs the end of the sample transfer rod as to guide the rod through the bent cryostat tubing. However, if the misalignment is too severe, detaching the Teflon guide will cause big vibration and may shake off the rod from the sample, hence cleave at almost room temperature rather than 4K. Usually when this happens we will land on a surface full of contamination.

Now back to the discussion of physics. Superconductivity occurs in CuO_2 plane, two layers below the cleaving plane. STM is usually thought as a surface probe. Hence the question (and usually the criticism about STM) is: is STM really accessing CuO_2 electronic property? The strongest argument is from Quasiparticle Interference (QPI), which measures interference pattern of elastically scattered quasiparticles from the points of highest joint density of states (JDOS) on the Fermi surface with initial and final momenta \vec{k}_i and \vec{k}_f [38]. By extracting Bogoliubov dispersion $E_B(\vec{k})$ from a set of vectors $\{\vec{q} = \vec{k}_f - \vec{k}_i\}$, Ref.[32] shows consistency between STM result and measured band structure by ARPES. Additionally, McElroy *et al.* [39] shows that QPI measured in STM is in quantitative agreement with autocorrelation of single particle spectra function $A(\vec{k}, \omega)$ measured by ARPES. These observations provide decisive argument that STM is indeed accessing intrinsic electronic states in CuO_2 plane.

As a matter of fact, STM measurement on BSCCO might have been saved from the fact that the cleaving does not happen right above CuO_2 plane. As a general rule, when cleaving along between planes, the periodic structure along the c -axis (in BSCCO case) is interrupted and will result in some dangling bonds. If the cleaving

happens just above CuO_2 planes, the dangling bonds will re-combine as to lower the total energy and therefore leave a reconstructed surface to STM. This surface layer may not even preserve superconductivity within it. However, in reality we have the surface terminated at BiO layer, two layers above CuO_2 plane. Hence, the CuO_2 plane is unperturbed and retains the bulk property. Because BiO and SrO are high gap insulator layer, they should be playing a similar role as vacuum (with a different dielectric constant) in the tunneling process.

In the next few sections, some well established STM measurement paradigms will be reviewed.

2.4 *d*-wave Energy Gap Map

The most prominent spectroscopic feature in STM measurement on cuprate is the “coherence peak” and is believed to be the superconducting gap. The superconducting gap size is defined to be the half of energy difference between the two primary peaks. It is well known that as doping increases the gap size decreases. Figure 2-8 shows the evolution of averaged spectra as function of doping measured by STM. The spectra evolve from having small gap and sharp coherence peak to large and broad gap. For the gap which is bigger than $\sim 65\text{mV}$, the peak is not well defined and is “pseudogap” type. Recently Alldredge *et al.* successfully used a scattering rate $\Gamma_2 = \alpha E(E = \Delta)$ in a simple modified *d*-wave density of states to depict evolution of electronic excitation from overdoped to underdoped side. This striking result shows so called “pseudogap” is likely to be a natural consequence of increased inelastic scattering possibly from spin fluctuation when $p > 0$. This result supports the view that so called “pseudogap” state is a pairing state but lacking coherence.

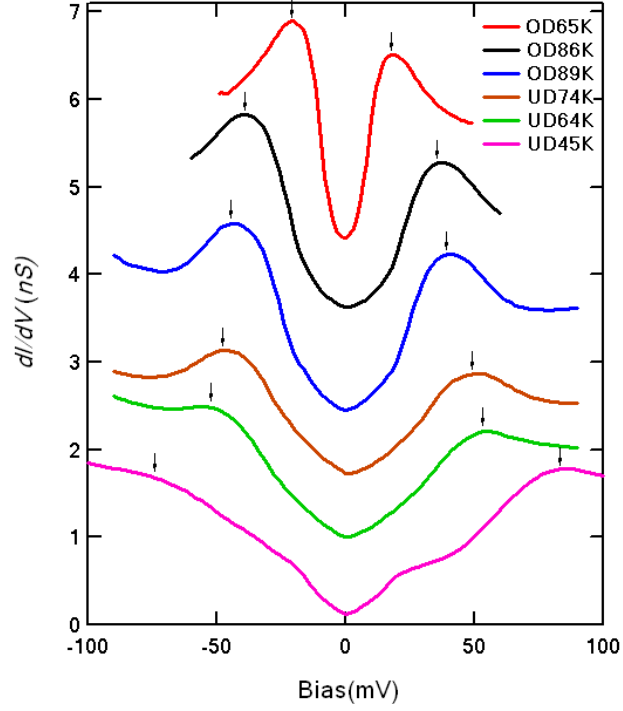


Figure 2-8 Spatially averaged conductance for different dopings. Spectral shape evolves from pronounced coherence peak in overdoped sample to broad, even totally vanished hump in underdoped side.

Gap size exhibits strong spatial disorder, manifested as patches of similar gap size regions about 2-3nm [40]. The nanometer patches in gap indicate the local nature of superconducting state and further studied in Ni-doped underdoped sample to reveal long range characteristics of a granular superconductivity [41]. Figure 2-9 shows typical gapmap for optimally doped Bi2212. For a field of view (FOV) of $\sim 40\text{nm}$, typically $(256)^2 \sim 10^5$ spectra are collected and analyzed to generate a gap map. The gap size varies over a large range from $\sim 25\text{mV}$ to $\sim 60\text{mV}$, with average $\sim 40\text{mV}$ for optimal Bi-2212.

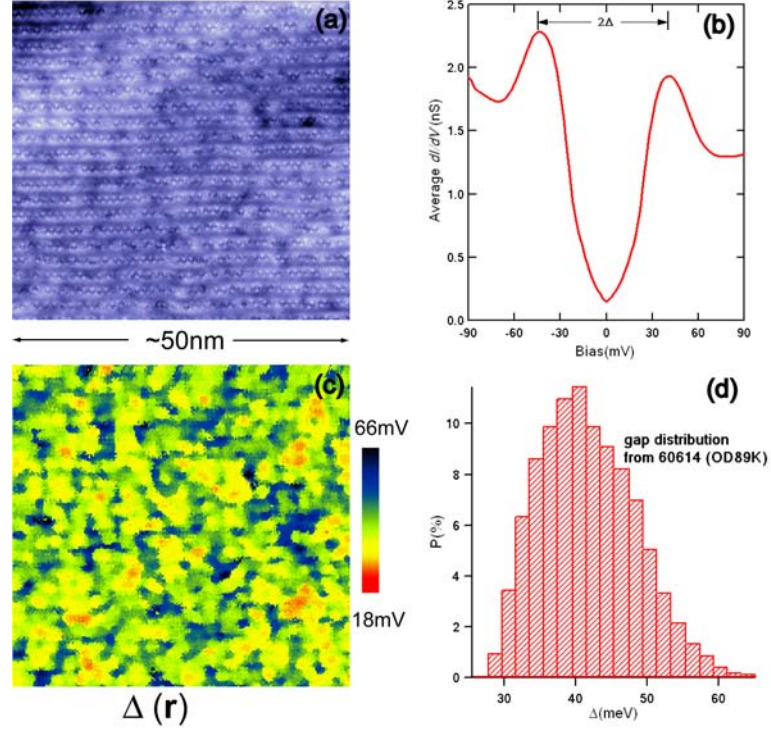


Figure 2-9 Gap map measurement scheme. This is from nearly optimal doped (slightly OD with T_c 89K) sample from RunC26. (a) Constant current topographic image of BiO layer taken at set up condition -150mV/10pA. (b) Spatially averaged spectrum. Half of the energy difference between the two coherence peaks is defined as gap Δ . (c) Extract Δ from each of $(256)^2$ spectra to generate gap map. Strong disorder is seen as local gap variation. (d) Histogram of gap size distribution, peaked around 40meV with arithmetic average 40.8meV and statistical spread about $\pm 8meV$.

Besides the Bi atoms and electronic inhomogeneity seen on the topograph, there is another prominent feature. There is an incommensurate modulation along a -axis (see Figure 2-3(c)), with periodicity $\sim 26\text{\AA}$ (~ 4.8 unit cell), seen on the topograph in Figure 2-9(a) as corrugations of surface. This modulation represents the periodic unit cell dimension distortion. It is obvious that the similar modulation pattern also appears in the gap map. Careful analysis of the correlations of gap map and topograph together

with crystallographic knowledge about BSCCO supermodulation reveals an impact of periodic local lattice distortion on superconductivity. This will be discussed in more details in later chapters.

2.5 Quasiparticle Interference (QPI)

STM has the unique ability to probe local electronic structure in real space. Moreover, because of the disorder nature of cuprates, the quasiparticles are violently scattered from impurities between states with well-defined \mathbf{k} 's. In superconducting Bi2212, the low energy (compared to gap maxima) conductance map $g(\mathbf{r}, \omega)$ is quite homogeneous and exhibits global spatial modulation. Thus exploring \mathbf{r} -space and \mathbf{k} -space relationship will provide new avenue to the understanding of quasiparticle behavior below T_c . McElroy *et al.* [38] developed novel quasiparticle Fourier Transform-Scanning Tunneling Spectroscopy (FT-STs) technique and made important discoveries of quasiparticle excitation in superconducting Bi2212.

For a delocalized state in a simple piece of metal with well-defined wavevector, when scattered elastically by impurity, its wavevector changes from \bar{k}_i to \bar{k}_f , but the energy remains the same. The scattering probability is described by the famous Fermi's golden rule:

$$w(\bar{k}_i \rightarrow \bar{k}_f) = \frac{2\pi}{\hbar} \left| \langle \bar{k}_i | V | \bar{k}_f \rangle \right|^2 n(E_i, \bar{k}_i) n(E_f, \bar{k}_f) \quad (2-9)$$

Where $\langle \bar{k}_i | V | \bar{k}_f \rangle$ is the matrix element of the interaction which causes the transition from the initial to the final state. Because there must be available states to scatter from and to, the product of density of states for initial and final states $n(E_i, \bar{k}_i) n(E_f, \bar{k}_f)$ naturally comes in as physical constraint. $E_i = E_f$ in the case of elastic scattering.

Assuming constant matrix elements, the scattering intensity is mainly determined by the joint density of states (JDOS).

In a superconductor, there is an additional coherence factor in the scattering process.

$$w_{sc}(\vec{k}_i \rightarrow \vec{k}_f) = (u_i u_f^* \mp v_i v_f^*) \frac{2\pi}{\hbar} \left| \langle \vec{k}_i | V | \vec{k}_f \rangle \right|^2 n(E_i, \vec{k}_i) n(E_f, \vec{k}_f) \quad (2-9)$$

In this modified equation

$$u_k^2 = \frac{1}{2} \left(1 + \frac{\mathcal{E}_k}{\sqrt{\Delta^2 + \mathcal{E}_k^2}} \right), \quad v_k^2 = \frac{1}{2} \left(1 - \frac{\mathcal{E}_k}{\sqrt{\Delta^2 + \mathcal{E}_k^2}} \right) \quad (2-10)$$

v^2 is the probability that a pair is occupied, u^2 is the probability that a pair is unoccupied. The positive sign in Equation (2-9) correspond to scalar potential scattering which does not change \vec{k} or spin σ . The negative sign corresponds to scattering from magnetic impurity, which breaks the time reversal symmetry.

Because of d -wave symmetry, the contour of constant energy (CCE) for quasiparticle in superconducting cuprate (for example, Bi-2212) has four-fold symmetry. The CCE is banana shaped on top of normal state band structure (Figure 2-9(a)). The density of states (DOS) is the integration of inverse energy gradient respective to \mathbf{k} along constant energy surface (contour)

$$n(\omega) = \int_{E(\vec{k})=\omega} \frac{1}{\nabla_{\vec{k}} E} \quad (2-11)$$

It is obvious from the plot that the biggest increase of \mathbf{k} as function of E $|\nabla_{\vec{k}}|^{-1}$ is at the eight tips of the ‘bananas’. Hence the quantum interference between the wave-like state \vec{k}_i and \vec{k}_f will produce the real space modulation with wavevector $\vec{q} = \vec{k}_f - \vec{k}_i$, and the strongest modulation is from the \mathbf{q} vectors connecting each tip of the four ‘bananas’. This model is called ‘octet model’ [42] and successfully described the

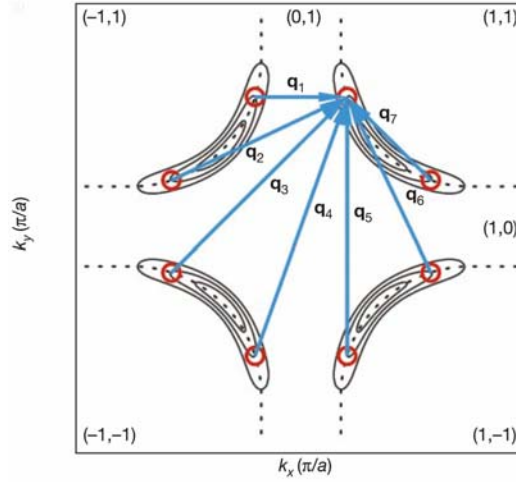


Figure 2-10 Band structure and ‘octet model’ for Bi2212. Taken from McElroy *et al.* [38]. The solid lines indicate the CCE for quasiparticle with different energies with increasing ‘banana’ size corresponding to higher excitation energy. The red circles label the points on the CCE with highest DOS. The \mathbf{q} -vectors connecting the red circles is the expected QPI pattern in Fourier transformed conductance map $g(\mathbf{q}, \omega)$.

essential features of quasiparticle interference. The example of QPI and its corresponding real space modulation is shown in Figure 2-10. Next I summarize the key results from the QPI study in McElroy *et al.* [38]:

- (1) On occupied side, the extracted location of octet elements $\mathbf{k}_s(\omega)$ and gap function $\Delta(\theta_k)$ agree well with ARPES measured Fermi surface and ARPES derived

$\Delta(\theta_k)$ of similar doping. This agreement gives confidence that STM is indeed accessing CuO_2 plane electronic states.

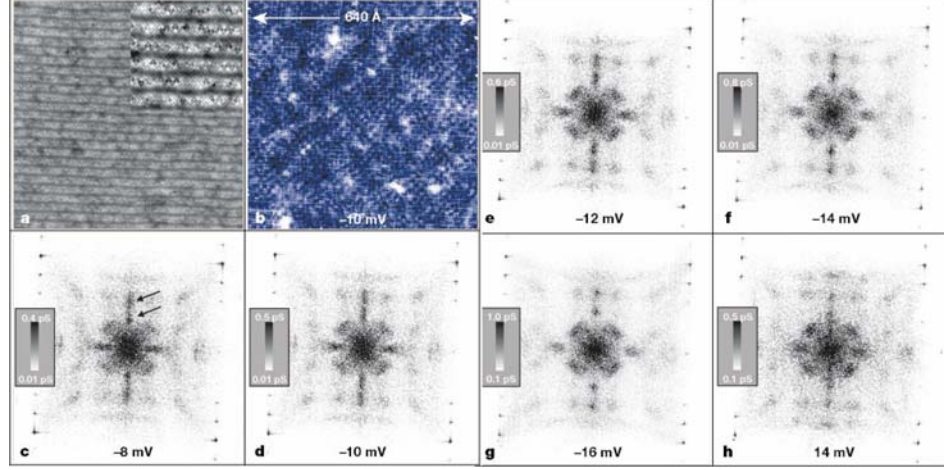


Figure 2-11 **r**-space and **q**-space images of LDOS modulations. Taken from ref. [38]. (a) Topographic image of BiO layer. (b) Representative **r**-space modulation $g(\mathbf{r}, \omega)$. (c)-(g) $g(\mathbf{q}, \omega)$ in filled side. The reciprocal lattice site is near the four corners. (h) The $g(\mathbf{q}, \omega)$ on empty side.

- (2) FT-STs on unoccupied states reveals similar but not identical $g(\mathbf{q}, \omega)$ compared with negative side. However, the derived gap function $\Delta(\mathbf{k})$ is indistinguishable between empty and filled states. This fact provides evidence that Bogoliubov type description of quasiparticle, which is accurate in BCS superconductor, in cuprate is at least qualitatively valid.
- (3) At energy $\omega \approx \Delta_0$, there is intense modulation in LDOS with $\mathbf{q} = \mathbf{G}$, where \mathbf{G} is reciprocal lattice vector. At certain energy ω , wherever ω is equal to local gap value, this modulation appears locally in $g(\mathbf{r}, \omega)$. The modulation corresponds to the antinodal states $\mathbf{k} \approx (\pi/a_0, 0)$ and hence signals strong scattering of antinodal quasiparticle.

Some technical notes on the measurement of QPI. To successfully image QPI, resolution in both \mathbf{r} -space and \mathbf{k} -space is needed. We also have time limitation from liquid Helium hold time (~ 72 hours). Suppose we take a map on a FOV of size $L \times L \text{ \AA}$, and the spatial resolution is $N \times N$ pixels. The optimal orientation for QPI is that supermodulation (which is along a -axis) is either aligned horizontally or vertically. This will put Cu-O-Cu bond pointing to 45 degrees and hence after Fourier transform the lattice Cu peaks are close to the four corners of the FFT image. In this way the details of \mathbf{q} -space pattern inside a unit cell will be zoomed in best. From the reciprocal relations between \mathbf{r} - and \mathbf{k} -space, it is easy to show that when the following relation is satisfied, we can get the best momentum space information:

$$\frac{N}{L} = 2 \times \frac{1}{a_0} \times \frac{1}{\sqrt{2}} \quad (2-12)$$

Where L is in unit of \AA , and a_0 is the length of Cu-O-Cu bond, $\sim 3.83 \text{ \AA}$. The factor $\sqrt{2}$ is to account for the diagonal orientation. Hence, for the typical FOV of about 520 \AA (nominally 460 \AA , but there is a lateral calibration factor about 1.15), the ideal pixel number $N \sim 200$. In practice, 256×256 pixels are used, to get higher S/N. The QPI will be discussed in more detail when comparing oxygen isotope effect.

2.6 Dopant Oxygen as Source of Local Electronic Disorder

Nanoscale electronic disorder has been discovered by SI-STM in many cuprate materials. These include the spatially varying energy gap on CuO chain in $\text{YBa}_2\text{Cu}_3\text{O}_{7-x}$ [43], the nondispersive ‘checkerboard’ LDOS modulation in $\text{Na}_x\text{Ca}_{2-x}\text{CuO}_2\text{Cl}_2$ [44], the subgap dispersive LDOS modulation [38] and energy gap disorder [40,41] in Bi2212 .

Hole doping in Bi2212 ($\text{Bi}_2\text{Sr}_2\text{CaCu}_2\text{O}_{8+\delta}$) is achieved by adding nonstoichiometric oxygen (δ per unit cell) into the crystal. The nonstoichiometric oxygen is electron acceptor with $-2e$ charge and is believed to reside either between BiO and SrO or within BiO layers [45]. The stoichiometric oxygen in BiO layer cannot be detected at low energy since they form BiO band structure as large gap insulator. The dopant oxygen, however, can form an impurity state below the Fermi level at lower energy.

- Dopant Oxygen Map (McElroy *et al.* [46])

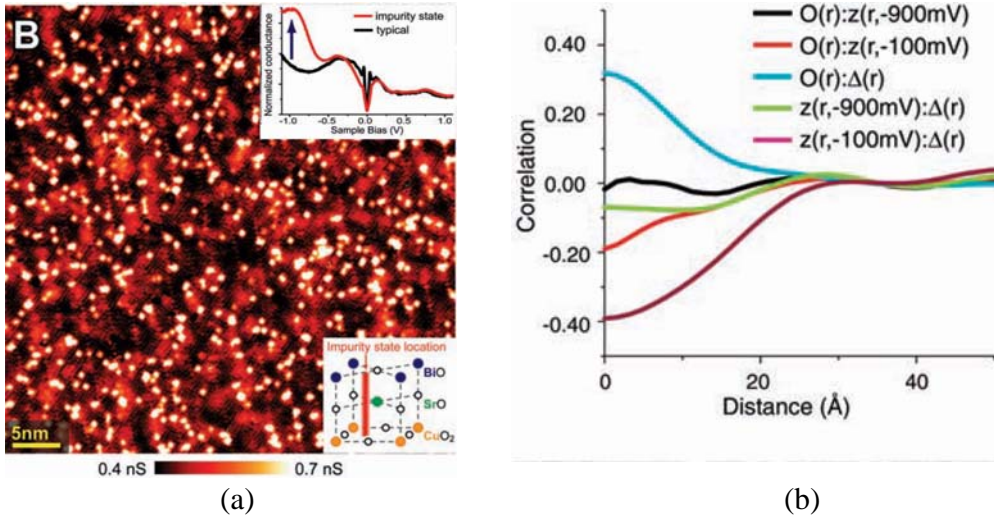


Figure 2-12 Oxygen map. From Ref. [46]. (a) The conductance map $g(\mathbf{r}, E = -0.96 \text{ eV})$. The bright dots show up because there is a broad peak near $V = -0.96 \text{ V}$ (see the upper right inset). The lower right inset shows the lateral position of this LDOS maxima. (b) The normalized correlation between various simultaneously measured images.

At bias voltage $V = -0.96 \text{ V}$, there is randomly distributed bright maxima in LDOS. Those bright spots in LDOS are determined as between Bi and O laterally but their vertical position is unknown. The density of such bright maxima scales with doping level, which supports the postulate that these each of these -0.96 V states corresponds to a single oxygen dopant. (See Figure 2-12(a)).

- Effect of Dopant Oxygen

From Figure 2-12(a) inset, one of the effects of dopant oxygen is to shift spectral weight to higher energy (on filled side). A simple electrostatic picture is that since the dopant oxygen ion is negatively charged, it will accumulate holes around it and therefore diminishing of gap size is expected [47-49]. However, the correlation between dopant oxygen position and local gap value shows the opposite trend. Figure 2-12(b) shows a series of normalized correlations between topograph $z(\mathbf{r}, V_B)$, oxygen location $O(\mathbf{r})$, and local gap size $\Delta(\mathbf{r})$. Here I will only summarize the result for gap. The zero displacement correlation $C[\Delta(\mathbf{r}) : O(\mathbf{r})] \approx +0.3$. This positive correlation means instead of diminishing gap magnitudes, there is increased gap magnitudes when approaching dopant oxygen. Another theoretical explanation is that dopant atoms causes local lattice distortion and hence modulates the local pair interaction either through changing local electron-phonon coupling or superexchange interaction [50]. This local pair modulation model successfully reproduced essential features seen in STM measurement: positive correlation between gap map and dopant location and anticorrelation between coherence peak height and gap value.

CHAPTER 3

Interplay between Lattice and Superconductivity in Cuprate

In BCS superconductor, electron-phonon interaction causes the electron pairing. In cuprate, however, the situation is far from clear. Electron-Boson interactions (EBI) are detected by various experimental probes, yet no consensus about which mode is the ‘pairing glue’ (or whether a ‘glue’ is needed) in high- T_c has been reached. A fundamental difficulty in spatially averaged probes like ARPES or neutron scattering is: the intrinsic nanoscale disorder in cuprate may leave some essential ingredient of EBI undetected. In this chapter, the atomic resolution d^2I/dV^2 -imaging study on $\text{Bi}_2\text{Sr}_2\text{CaCu}_2\text{O}_{8+\delta}$ will be presented. This work is led by Dr. Jinho Lee and the superior quality crystal is prepared by Dr. Kazuhiro Fujita (who also worked on measurement for a long time). I was heavily involved in determining oxygen isotope shift.

3.1 The Dip-Hump Feature in Cuprate Superconductor

- Strong Coupling BCS

First of all, a little bit history will be given. The phonon mechanism of conventional superconductor was qualitatively confirmed by isotope experiment on superconducting transition temperature T_c [12]. The direct observation of electron-lattice coupling in conventional superconductor is observed in break junction experiment where ‘kinks’ in superconducting density of states are detected [51] at known phonon energies. McMillan and Rowell [52] calculated phonon density of states from tunneling spectrum and later on, McMillan [15] used Eliashberg theory [53] of strong coupling superconductor to predict T_c for various superconductors and got quantitative agreement with the experiment, hence unambiguously proved BCS theory

is the correct microscopic description for conventional superconductor. In weak-coupling BCS theory, opening of superconducting gap will deplete density of states near to Fermi level and pile them up at the gap edge. But above the gap, the density of states will go back to its normal metal one (roughly constant). However, when the electron-phonon coupling becomes strong, deviation from weak-coupling BCS theory can be seen. Such deviation was first observed in break junction tunneling experiment by Giaever, Hart Jr. and Megerle [51]. Figure 3-1 is borrowed from the original paper. The ‘kink’ features, which is the signature of electron-phonon coupling, continue to be a hot topic to study in high- T_c research after forty years. Normalized density of states $N_{sc}(E)/N_{norm}(E)$ is measured with high precision for a Pb-MgO-Mg sandwich. The authors noticed that the crossover energy above which the normalized DOS comes back to unity is about Debye temperature, $E \approx k_B \theta_D$.

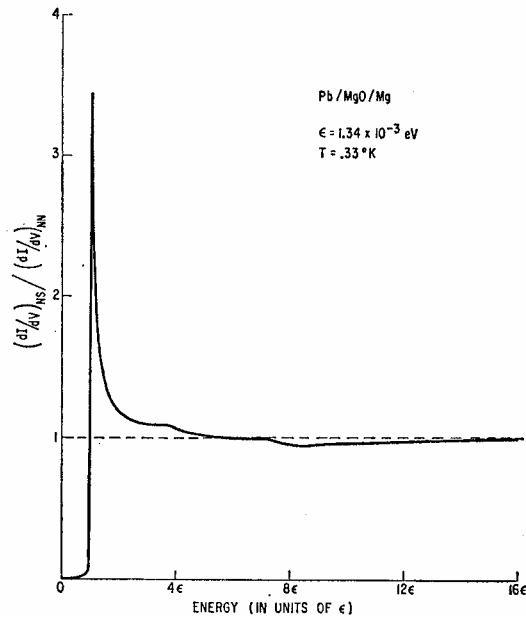


Figure 3-1 Normalized conductance of Lead. Borrowed from ref. [51]. The ‘bumps’ at high energy is deviation from weak-coupling BCS theory and is the signature of electron-phonon coupling in a strong-coupling superconductor.

- Electron-Boson Coupling in Cuprates

In cuprates, electron-boson interactions are studied extensively but no consensus about the role of boson in electron pairing has been reached. The studies include:

1. Tunneling spectroscopy, in which similar singularity in DOS as in conventional superconductor is first observed [54] and studied extensively in the framework of Eliashberg strong-coupling theory of superconductivity under the assumption that such singularity corresponds to a boson (largely thought as phonon) responsible for pairing, as in conventional strong-coupling superconductor [55-59].
2. Angle Resolved Photoemission Spectroscopy (ARPES). A ‘kink’ is also observed in band dispersion by ARPES [60-65], which is mainly interpreted as electron coupled to phonon [60,63,65] or magnetic resonance mode [60].
3. Inelastic Neutron Scattering (INS) measures both low energy and high energy spin excitations ranging from parent insulator to superconducting phase in LSCO, YBCO and LBCO. Magnetic neutron scattering has provided abundant evidences for the intimate relation between magnetic and superconducting order [66-70]. These include (but not limited to): A good review has been given by Birgeneau, Stock, Tranquada and Yamada [71].
4. INS also measures phonon dispersion in cuprates, which shows strong interaction between phonon and doped holes and the relationship with temperature [24-27].

The two main contenders for pairing boson in cuprates, phonon and magnetic modes, all find supports for their importance in high- T_c superconductivity. For phonon, examples include: (i) Through temperature and doping dependence study on different families of hole doped cuprates, Lanzara *et al.* [63] identified the ‘kink’ seen in

ARPES band dispersion around 50-80 mV as due to electron-phonon coupling. (ii) In LSCO and YBCO, INS measurement shows that the zone boundary phonon significantly softens upon doping [72,73], indicating the strong coupling between phonons and doped holes. The examples that support the importance of magnetic modes are: (i) In LSCO and YBCO, upon hole doping, the commensurate AF order is destroyed and incommensurate spin density wave (SDW) is developed. The magnetic peak of SDW is displaced from the (π, π) position symmetrically [18,19]. Strikingly, the value of this displacement vector from (π, π) scales with T_c/doping (in underdoped side) [74]. (ii) Perhaps a more fundamental argument supporting magnetic origin is, AF spin fluctuation tends to favor a d -wave order parameter with vanishing gap at points or lines at Fermi surface [30,31]. Figure 3-2 shows the examples from ARPES and INS.

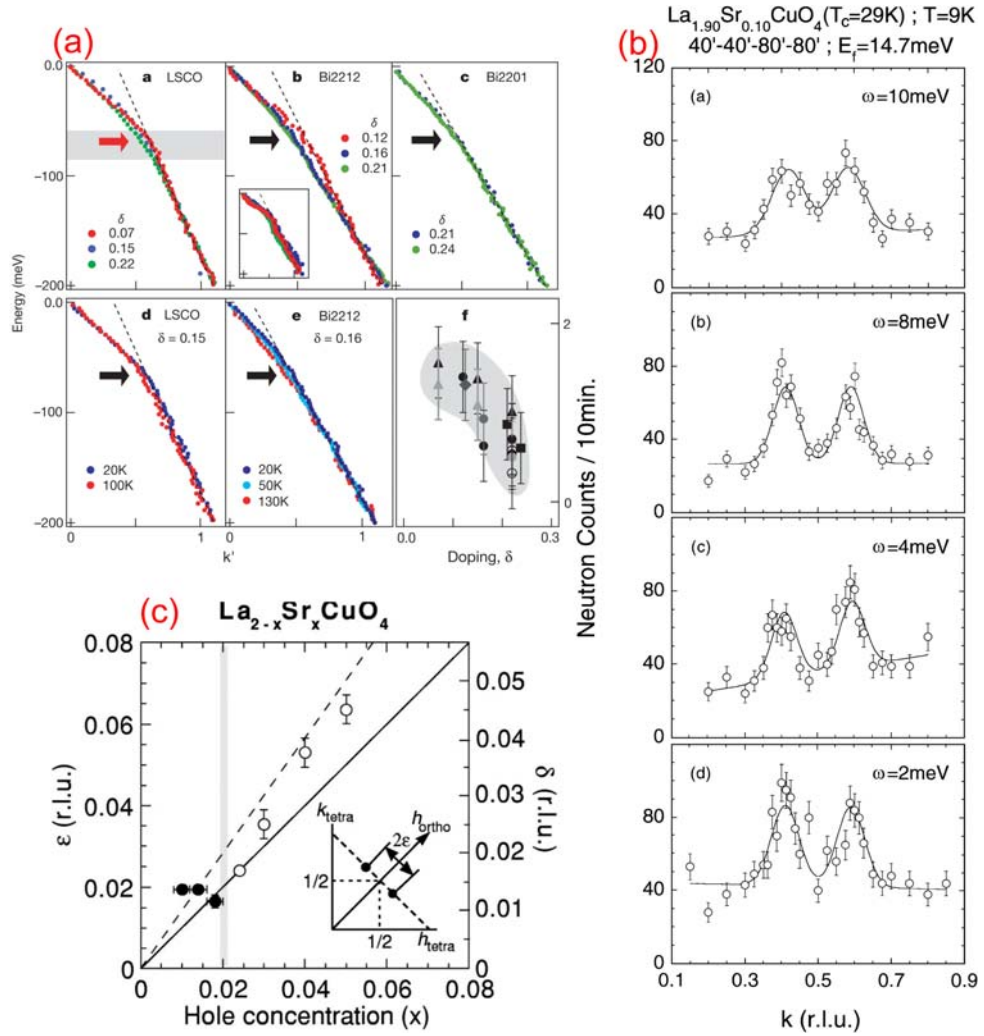


Figure 3-2 Examples of different bosonic modes. (a) From Lanzara *et al.* [63]. The 'kink' seen in band dispersion is around 50-80mV. The ubiquitous 'kink' feature seen in many families of p-type cuprates, the insensitivity of 50-80mV kink energy to doping, and the temperature dependence of this 'kink' signal are strong evidence that this renormalization seen in ARPES is due to electron-phonon interaction. (b) INS on LSCO from Lee *et al.* [67]. The undoped insulator has AF order defined by a single peak at (π, π) (not shown here). Upon doping, the incommensurate SDW emerges, with magnetic peak symmetrically displaced from (π, π) . (c) From Matsuda *et al.* [74]. The magnitude of the displace vector scales with doping (for low doping case), suggesting that the incommensurate magnetic excitation is directly associated with superconductivity.

3.2 d^2I/dV^2 Technique and Gap Referencing

Inelastic tunneling is a well established tool in STM measurement. The peak in second derivative (or the step feature in dI/dV) has been used to mark the energy of onset of additional tunneling channel. For example, in single-molecule vibrational spectroscopy [75], the step comes from excitation of vibrational mode when the energy goes above threshold and additional tunneling channel is available. In Spin-flip spectroscopy [76], step feature is created by tunneling electrons' losing energy to spin-flip excitation of magnetic atom in external magnetic field.

The 'kink' feature in tunneling spectra is associated with electron self-energy change due to coupling to bosonic mode. In general, taking derivative will reduce the S/N by about one order of magnitude. That's why it took 10 hours for Stipe *et al.* [75] to get a single d^2I/dV^2 spectrum. The challenge in Cuprate is that its superconducting electronic structure is atomically disordered. Hence we need to image both EBI and lower energy electronic disorder with atomic resolution simultaneously. The ~72 hour Helium hold time leaves us about 3 seconds for each d^2I/dV^2 spectrum. An atomic resolution d^2I/dV^2 -imaging technique is mainly developed by Dr. Jinho Lee.

The idea is similar as measuring dI/dV using lock-in. The response of the sample after perturbed by some small voltage ΔV is ΔI . In most cases, the I - V characteristic of solids is differentiable and we can assume purely resistive response. Using Taylor's expansion,

$$I(V + \Delta V) = I(V) + \left. \frac{dI}{dV} \right|_V \Delta V + \frac{1}{2} \left. \frac{d^2I}{dV^2} \right|_V (\Delta V)^2 + \dots \quad (3-1)$$

$$\Delta I = I(V + \Delta V) - I(V) = \left. \frac{dI}{dV} \right|_V \Delta V + \frac{1}{2} \left. \frac{d^2I}{dV^2} \right|_V (\Delta V)^2 + \dots \quad (3-2)$$

In standard lock-in method, a sinusoidal perturbation is sent to experiment:

$$\Delta V = \Delta V_0 \cos(\omega t) \quad (3-3)$$

Hence

$$\Delta I = \left. \frac{dI}{dV} \right|_V \Delta V_0 \cos(\omega t) + \frac{1}{2} \left. \frac{d^2 I}{dV^2} \right|_V (\Delta V_0)^2 \cos^2(\omega t) + \dots \quad (3-4)$$

Then this response current goes through the current amplifier. The phase shift induced by various circuit components like filter is compensated by the phase setting in Lock-in amplifier, hence we drop the additional phase in the analysis. The input response to Lock-in amplifier is voltage signal

$$V_{sig} = G \Delta I \quad (3-5)$$

Where G is the gain. To get approximate dI/dV , use Lock-in amplifier to multiply input response signal with reference signal $V_{ref} \cos(\omega t)$. After low pass filter, one gets

$$LF[V_{ref} \cos(\omega t) V_{sig}] = \frac{1}{2} G \left. \frac{dI}{dV} \right|_V \Delta V_0 \quad (3-6)$$

Where LF stands for “low pass filter”. Note all the high frequency is substantially filtered out, that’s why there is no term with frequency ω (or higher harmonics) left.

Hence,

$$\boxed{\left. \frac{dI}{dV} \right|_V \propto LF[V_{ref} \cos(\omega t) V_{sig}]} \quad (3-7)$$

This is how the usual Lock-in measurement of conductance dI/dV is done. To measure d^2I/dV^2 , multiply the reference signal $V_{ref} \cos(2\omega t)$, and hence gets

$$V_{ref} \cos(2\omega t) V_{sig} = \frac{dI}{dV} \Big|_V \Delta V_0 \cos(\omega t) + \frac{1}{2} \frac{d^2I}{dV^2} \Big|_V (\Delta V_0)^2 \cos(\omega t) \frac{\cos(2\omega t) + 1}{2} + \dots \quad (3-8)$$

Similarly, after low pass filter, one gets

$$LF[V_{ref} \cos(2\omega t) V_{sig}] = \frac{1}{8} G \frac{d^2I}{dV^2} \Big|_V (\Delta V_0)^2 \quad (3-9)$$

Therefore, when setting the Lock-in to phase lock on second harmonic response, there is also a simple relation

$$\boxed{\frac{d^2I}{dV^2} \propto LF[V_{ref} \cos(2\omega t) V_{sig}]} \quad (3-10)$$

In the real measurement, two Lock-in amplifiers are used. One sends out modulation perturbation and then multiply ω reference to response signal to extract dI/dV from first harmonic. The same response signal is fed into a second Lock-in, multiplied by 2ω reference to extract d^2I/dV^2 from second harmonic.

In real experiment, both dI/dV and d^2I/dV^2 are simultaneously recorded. Directly measured and numeric d^2I/dV^2 from dI/dV yield the same result. Next, I will summarize the numeric procedure to extract d^2I/dV^2 from dI/dV , and introduce the ‘gap referencing’ method. The example of result from each step is shown in Figure 3-3.

1. Take the raw spectrum, identify the gap maxima as Δ shown in Figure 3-1(a). In the conventional superconductor, phonon mode energy Ω is measured from gap edge [52], i.e. $\Omega = E - \Delta$. In cuprate, gap has strong local variation, hence in order to remove the local disorder $\Delta(\mathbf{r})$, one needs to identify the local gap maxima for each spectrum, then shift $dI/dV(\mathbf{r}, E)$ to new energy scale $dI/dV(\mathbf{r}, \omega = E - \Delta)$. In practice, gap map $\Delta(\mathbf{r})$ is generated first, then the spectrum is shifted according to the local gap value. This process is called ‘gap reference’.

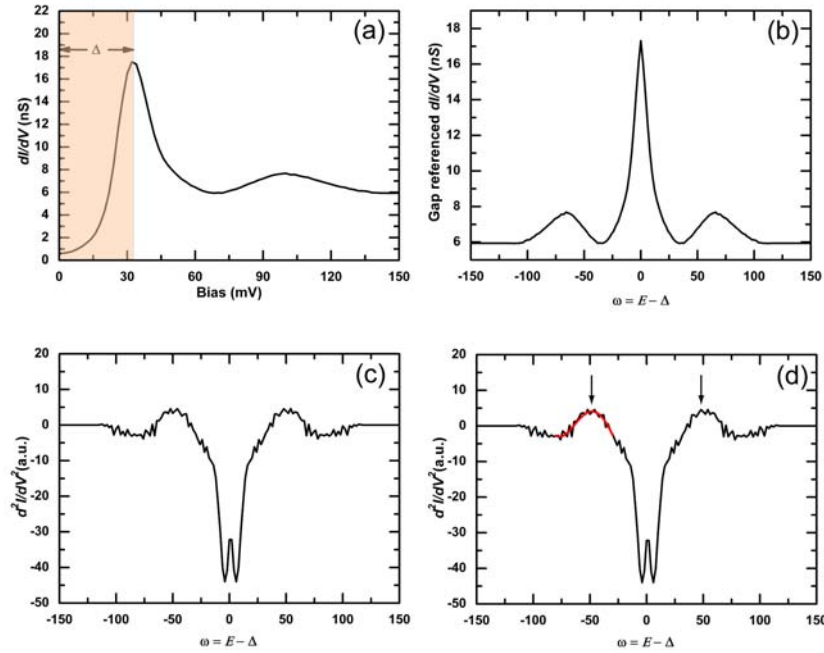


Figure 3-3 Numeric procedure to extract $d^2I/dV^2(\mathbf{r}, \omega)$ in $\text{Bi}_2\text{Sr}_2\text{CaCu}_2\text{O}_{8+\delta}$. (a) A raw spectrum from conductance map $dI/dV(\mathbf{r}, E = eV)$. No spatial average is taken. This demonstrates the S/N needed to either obtain d^2I/dV^2 numerically or from direct measurement. (b) Symmetrized $dI/dV(\mathbf{r}, \omega = E - \Delta)$ after gap reference. (c) 3 point ‘divergent’ derivative gives $d^2I/dV^2(\mathbf{r}, \omega = E - \Delta)$. (d) Polynomial fit of $d^2I/dV^2(\mathbf{r}, \omega)$. The fitted curve in red shows the quality of this algorithm. The arrows indicate to the peaks bosonic energy.

2. Due to time constraint, usually a half map is taken, $0 \rightarrow +150\text{mV}$ or $-150 \rightarrow 0\text{mV}$. After shifting energy scale, we can reflect the half spectrum to make it symmetric, as shown in Figure 3-3(b).
3. Next, take 3 point numeric derivative by $y'(x) \approx \frac{y(x+h) - y(x-h)}{2h}$. This derivative is taken from 0mV to higher and lower bias energies, hence yielding the symmetric $d^2I/dV^2(\mathbf{r}, \omega)$ with the broad peak around $\pm 50\text{mV}$ bosonic mode energy. See Figure 3-3(c).
4. At last, using polynomial (from order 4 to 11) $y(x) \approx c_0 + \sum_{n=4}^{11} c_n x^n$ to fit the numeric $d^2I/dV^2(\mathbf{r}, \omega = -30\text{mV} \rightarrow -80\text{mV})$. Then peak of the fitted curve is the mode energy $\Omega(\mathbf{r})$. The overlaid red curve in Figure 3-3(d) is the fitted polynomial.

Figure 3-4 shows the spatial distribution of boson energy after gap referencing. Strong local disorder is revealed.

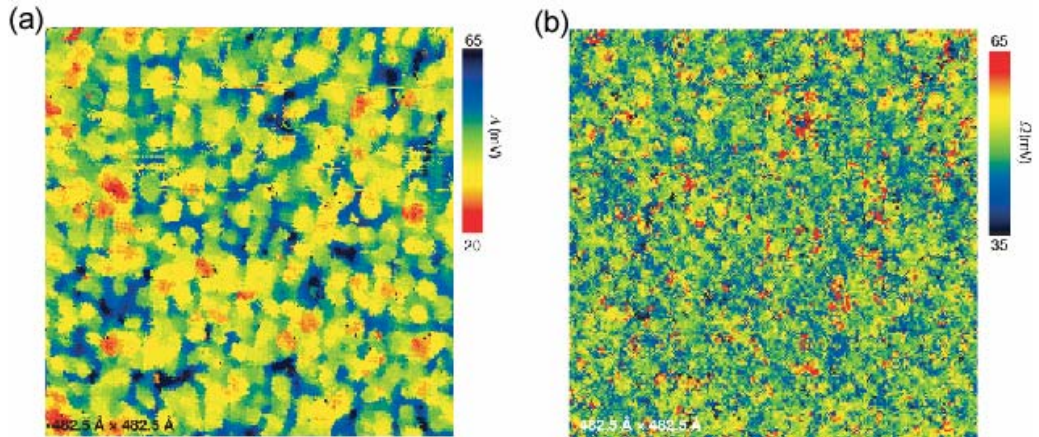


Figure 3-4 shows the example of spatial distribution of bosonic mode energy $\Omega(\mathbf{r})$ in $\text{Bi}_2\text{Sr}_2\text{CaCu}_2\text{O}_{8+\delta}$. (a) The gap map $\Delta(\mathbf{r})$, showing the $\sim 2\text{-}3\text{nm}$ ‘coherent’ patch. (b) Image of distribution of boson energies $\Omega(\mathbf{r}) = \Pi(\mathbf{r}) - \Delta(\mathbf{r})$. $\Pi(\mathbf{r})$ is the bias voltage where the peak in d^2I/dV^2 occurs.

3.3 Doping Dependence of Mode Energy

There has been a long debate about the origin of bosonic modes coupled to the electrons in hole doped cuprate, as discussed in section 3.1. One important marker to identify which one is coupled to the electron (in superconducting state) is the doping dependence, since spin mode will have quite strong doping dependence while lattice mode, should in general be inert to doping change.

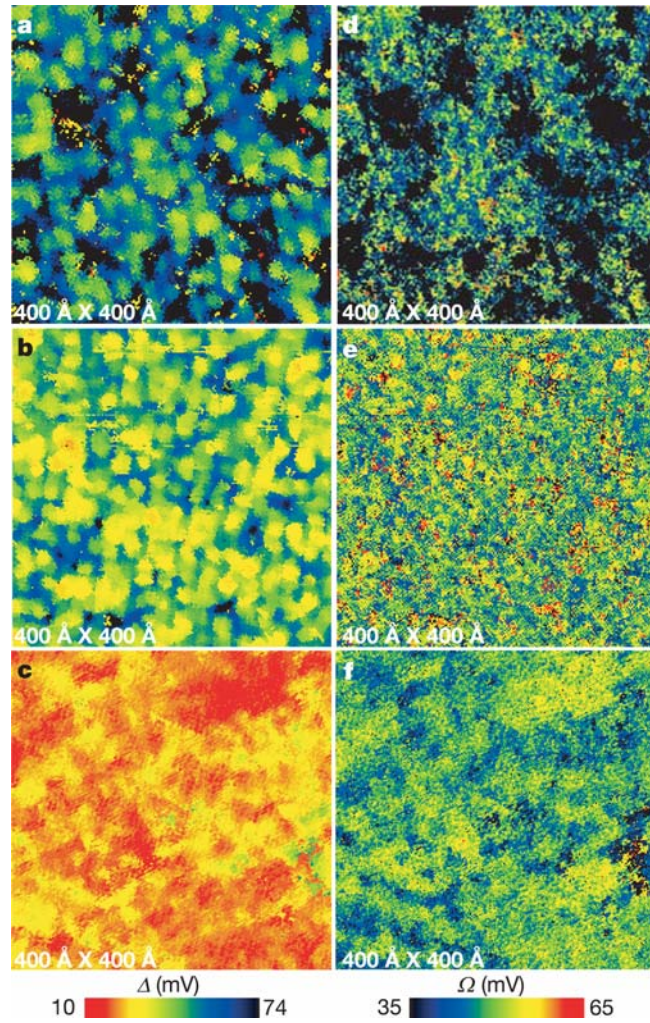


Figure 3-5 Doping dependence of $\Delta(\mathbf{r})$ and $\Omega(\mathbf{r})$ in $\text{Bi}_2\text{Sr}_2\text{CaCu}_2\text{O}_{8+\delta}$. (a)-(c): gap maps of three dopings $p \sim 0.12$, ~ 0.18 and ~ 0.24 respectively. (d)-(f): the simultaneously determined $\Omega(\mathbf{r})$.

Figure 3-5 shows the doping dependence of gap maps $\Delta(\mathbf{r})$ and mode energy maps $\Omega(\mathbf{r})$ for $p \sim 0.12$, $p \sim 0.18$ and $p \sim 0.24$. In order to show the change of energies with doping, all the $\Delta(\mathbf{r})$'s are displayed in the same absolute color scale, and so are all the $\Omega(\mathbf{r})$'s. The black regions in $\Delta(\mathbf{r})$ and $\Omega(\mathbf{r})$ are where neither Δ nor Ω values can be determined (the 'pseudogap' region). Three pieces of information are immediately revealed: (i) The average gap value reduces from ~ 60 meV to ~ 20 meV with increasing doping, but average mode energy $\bar{\Omega}$ more remains similar. (ii) $\Delta(\mathbf{r})$ and $\Omega(\mathbf{r})$ are spatially anti-correlated. (iii) The spatial correlation pattern changes over the doping.

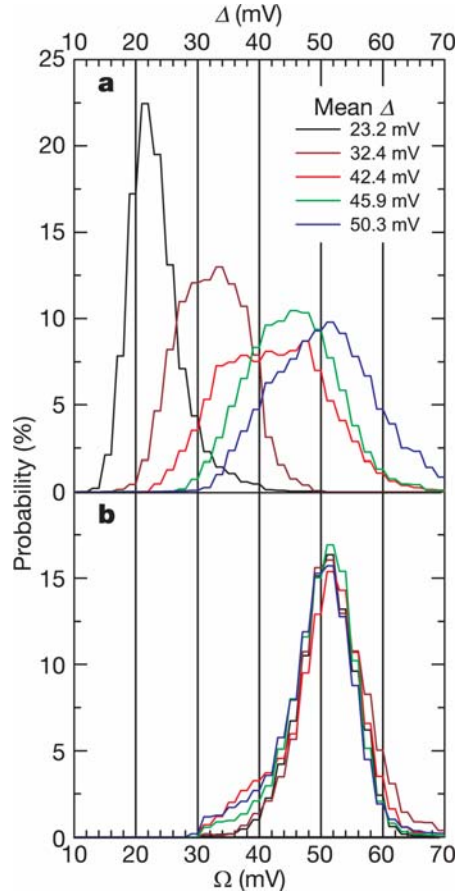


Figure 3-6 Doping dependence of energy gap histograms and boson energy histograms. While $\bar{\Delta}$ falls rapidly with doping, $\bar{\Omega}$ remains unchanged.

Figure 3-6 clearly shows the drastically different response of Δ and Ω to doping change. The average gap increase from $\sim 20\text{mV}$ to $\sim 50\text{mV}$ and the distribution shape changes from sharply peaked to broad shape when doping changes from $p \sim 0.24$ to $p \sim 0.12$. However, the value of mode energy $\bar{\Omega} = 52 \pm 1\text{mV}$ is not influenced by changing hole concentration, nor is the shape of Ω distribution. The datasets used are 50418, 20219, 40504, 41223, 40704.

3.4 Interaction with Antinodal Quasiparticle

Theoretical predictions have been made about spatial modulation in $dI/dV(\mathbf{r})$ or $d^2I/dV^2(\mathbf{r})$ caused by coupling of electron to bosonic mode. For example, coupling to the “41mV” collective spin resonance mode is predicted to result in modulation in $dI/dV(\mathbf{r})$ with wavevector $Q \approx (\pi, \pi)$ at energies $\approx \pm(\Delta_0 + \Omega_0)$ [77]. Where Δ_0 is the gap maxima and Ω_0 is mode energy. Considering τ_1 scattering from various bosonic modes, Zhu *et al.* [78] also show that highly anisotropic coupling to B_{1g} phonon will produce spatial modulation in $d^2I/dV^2(\mathbf{r})$, again at $\approx \pm(\Delta_0 + \Omega_0)$. As usual, experimental results do have some deviation from those theoretical predictions. The unprocessed $d^2I/dV^2(\mathbf{r}, E)$ does not show any modulation as predicted by the above theories. However, there is a basic assumption in all above theoretical models which does not match the real experimental observation, and such experimental observation is one of the key properties of cuprate. That is, the strong local disorder of gap maxima Δ . As a matter of fact, the spatial modulation might have been “scrambled” by the strong disorder in Δ , because if there is modulation in intensity of $d^2I/dV^2(\mathbf{r})$ at the bosonic energy $\Pi = \Delta + \Omega$, Π would be shifted randomly by disordered Δ and hence the high intensity point of $d^2I/dV^2(\mathbf{r})$ would be moved to different energies. Therefore, in this case, the inherent global spatial pattern is broken into small nanometer pieces and redistributed to different energies.

Figure 3-7 shows the comparison between unprocessed $d^2I/dV^2(\mathbf{r}, E)$ and ‘gap referenced’ $d^2I/dV^2(\mathbf{r}, E - \Delta)$. If there is very weak, non-dispersive modulation either in the unprocessed or ‘gap referenced’ layered image, then adding the image over a range of energy of interest would enhance the contrast. By doing the summation, we have an image $B(\mathbf{r}) = \sum_E d^2I/dV^2(\mathbf{r}, E)$, where summation of E covers the energies centered at $\bar{\Delta} + \bar{\Omega}$ (which depends on doping) and whose range is determined by statistical spread of both Δ and Ω . The next step is to use the data shifted from $|E| > \Delta$ to the local bosonic energy scale $\omega(\mathbf{r}) = E - \Delta(\mathbf{r})$ based on the reasoning discussed above. To enhance contrast, the integration is also performed to ‘gap referenced’ data to generate $\Gamma(\mathbf{r}) = \sum_{\omega=40mV}^{65mV} d^2I/dV^2(\mathbf{r}, \omega)$. Since both $\bar{\Omega}$ and its distribution remains unchanged for different dopings, the same summation range can be used for all the dopings, $\sim 40mV$ to $\sim 65mV$. After this operation, several intriguing results emerge.

- (1) In the unprocessed data, neither $d^2I/dV^2(\mathbf{r})$ at individual energy E nor the integrated version $B(\mathbf{r}) = \sum_E d^2I/dV^2(\mathbf{r}, E)$ shows any spatial modulation. This is true for all the dopings from $p \sim 0.12$ to $p \sim 0.22$. See Figure 3-7(a) and (b).
- (2) After ‘gap referencing’, clear spatial modulation shows up. The integration $\Gamma(\mathbf{r}) = \sum_{\omega=40mV}^{65mV} d^2I/dV^2(\mathbf{r}, \omega)$ enhances such spatial contrast, and such enhancement after integration is also a proof that this modulation is non-dispersive (otherwise the spatial feature would be smeared out after summation). Fourier transform of $\Gamma(\mathbf{r})$ shows modulation wavevectors $\mathbf{p}_1 \approx 2\pi/a_0[\pm(0.2, 0); \pm(0, 0.2)] \pm 15\%$, which corresponds to ~ 5 unit cell spatial periodicity. See Figure 3-7 (c) and (d).

Figure 3-7 Qasi-periodic spatial modulation in $d^2I/dV^2(\mathbf{r}, \omega)$ after gap referencing.

(a) Integrated modulation $B(\mathbf{r}) = \sum_{E=70mV}^{120mV} d^2I/dV^2(\mathbf{r}, E)$ made from data 40504. Gap

value has average $\bar{\Delta} \approx 43.0mV$ and spread from 30mV to 60mV. Mode energy $\bar{\Omega} \approx 52mV$ and spread from 40 to 60mV. Hence the relevant energy range for EBI $\Delta + \Omega \approx 70mV \rightarrow 120mV$ is used for integration. There is no obvious real space modulation. (b) The Fourier transform of $B(\mathbf{r})$. There is no feature in \mathbf{q} -space. (c)

Integrated modulation $\Gamma(\mathbf{r}) = \sum_{\omega=40mV}^{65mV} d^2I/dV^2(\mathbf{r}, \omega)$ for the same dataset. Clear spatial

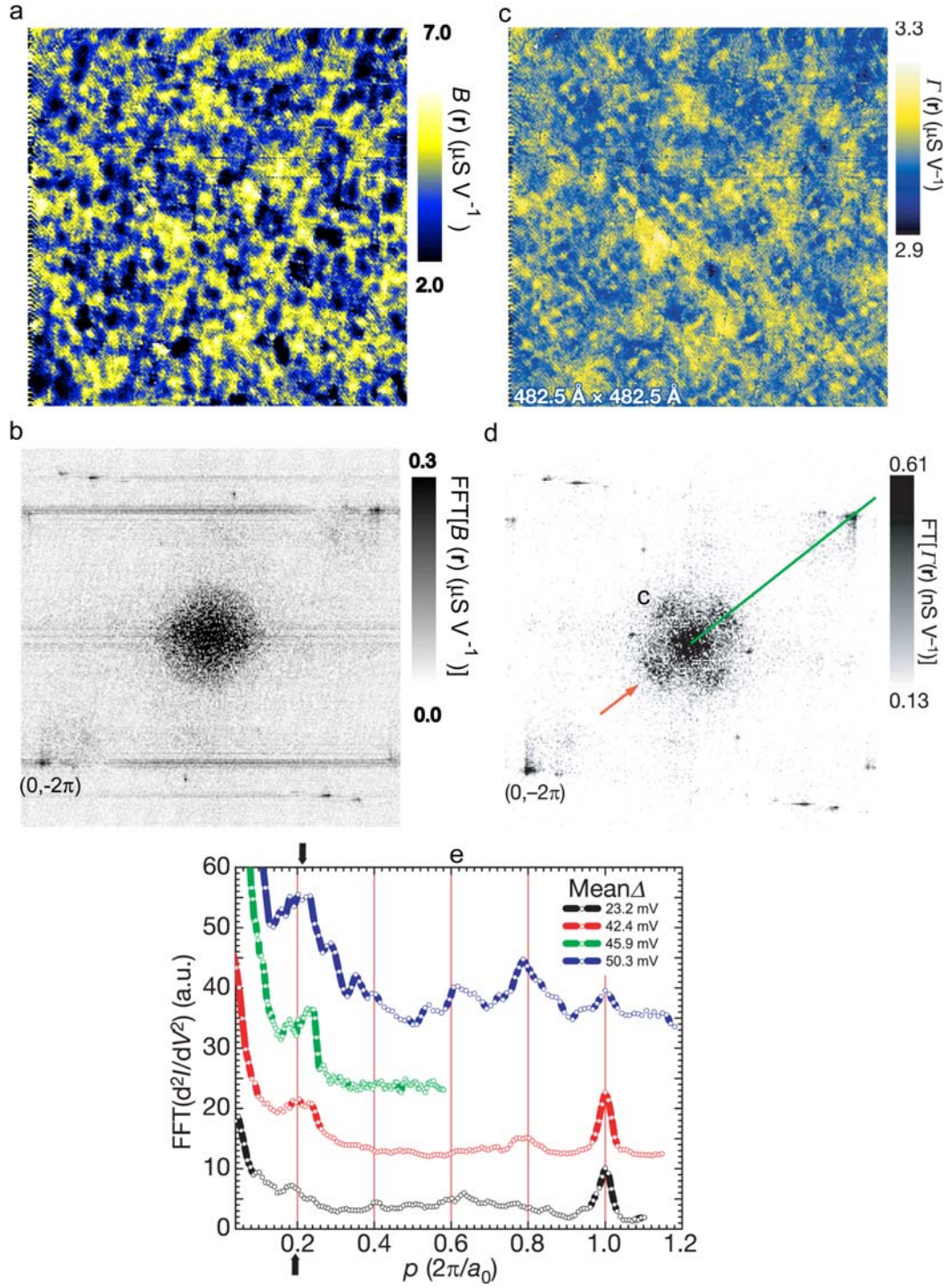
modulation is seen along Cu-O bond direction and having wavelength about $5a_0$.

This modulation is seen in gap referenced $\Gamma(\mathbf{r})$ for all the dopings. (d) Fourier transform of $\Gamma(\mathbf{r})$. The wavevectors of $d^2I/dV^2(\mathbf{r}, \omega)$ are

$\mathbf{p}_1 \approx 2\pi/a_0[\pm(0.2,0);\pm(0,0.2)] \pm 15\%$, as indicated by the arrow. (e) Doping

dependence of \mathbf{p}_1 . The plot shows the intensity of FFT along $(0,0) \rightarrow (0,2\pi)$ direction.

The very similar modulation wavevectors are found in all dopings, with the variation within the resolution.



- (3) The modulation in $\Gamma(\mathbf{r})$ along Cu-O bond direction is doping independent within experimental resolution.

The observation of modulation in $d^2I/dV^2(\mathbf{r},\omega)$ is a signature that the detected bosonic mode strongly interacts with antinodal quasiparticle. The fact that one needs to do gap reference to reveal such modulation is an amazing but still not well understood point, although we have some hand waving arguments earlier in this section. More will be discussed at the end of this chapter.

3.5 Oxygen Isotope Shift in Mode Energy

The doping independence of average mode energy $\bar{\Omega}$ points to lattice mode as the candidate for the boson mode detected in STM. However, a more definitive proof would be to change some of the inherent lattice characteristics and measure the response. Isotope substitution is a well established tool to probe the lattice effect, since the primary effect of such substitution is to change ionic mass M and naturally, the property of lattice vibration.

The oxygen substituted $\text{Bi}_2\text{Sr}_2\text{CaCu}_2\text{O}_{8+\delta}$ is grown by Dr. Fujita, with all the ^{16}O replaced by ^{18}O . The superb quality of such isotope substituted crystal enables us to do experiment and finally detected the shift of mode energy due to such substitution.

Figure 3-8 shows the result of atomic resolution d^2I/dV^2 -imaging on oxygen isotope substituted Bi-2212. The shift in the mode energy is simple but it took long and careful measurement to confirm. Figure 3-8 (a) shows the spatially averaged second derivative $d^2I/dV^2(\omega = E - \Delta)$ after gap reference. The peak in d^2I/dV^2 is shifted to lower energy for ^{18}O sample. This check is simple but important, since it is the

result from the minimal processed data and hence is free from possible numeric error. Figure 3-8(b) shows histograms of Ω for ^{16}O and ^{18}O samples. The shift of average mode energy is $-3.7 \pm 0.8 \text{ meV}$, about 6% reduction in mode energy, this reduction is $\sim 1 - \sqrt{16/18}$, which is expected from the classical lattice vibration model.

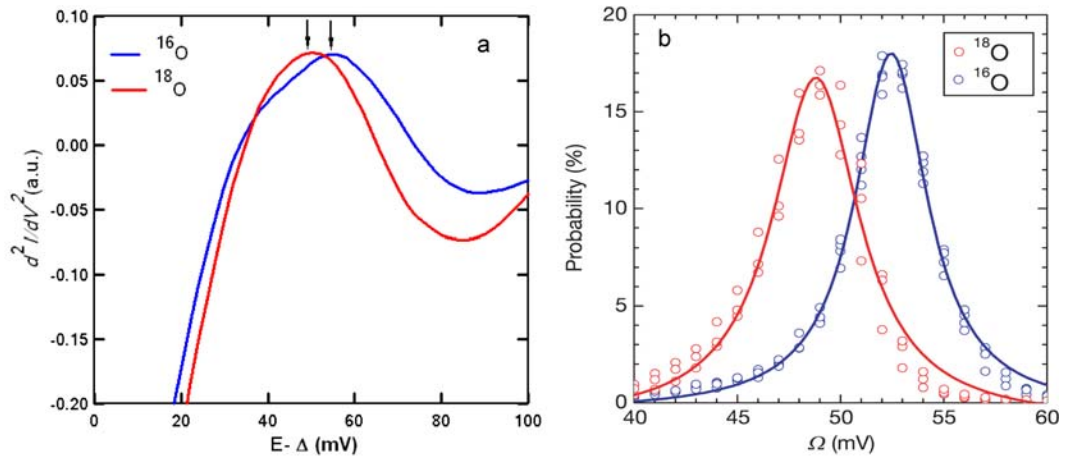


Figure 3-8 $^{18}\text{O}/^{16}\text{O}$ isotope effects on $d^2I/dV^2(\mathbf{r}, \omega)$ spectra and the distribution of boson energies. (a) The spatially averaged $d^2I/dV^2(\omega)$ after gap reference from 60614 (^{16}O) and 51219 (^{18}O). The peak of $d^2I/dV^2(\omega)$ is shifted from 54mV for ^{16}O (blue) to 50mV for ^{18}O (red). (b) The histograms for all values of Ω measured on ^{16}O samples (blue) and ^{18}O samples (red). The average shift of mode energy is $-3.7 \pm 0.8 \text{ meV}$. This shift in distribution is measured the same for both filled side and empty side. Note: the doping levels from the two isotope samples are different, with $^{16}\text{T}_c \approx 76\text{K}$ and $^{18}\text{T}_c \approx 88\text{K}$.

The oxygen isotope shift in mode energy is the direct proof that the d^2I/dV^2 signal detected in STM is dominated by the lattice vibration involving oxygen. The doping difference for the two isotopes should not change the conclusion about isotope shift, since the mode energy does not change with doping.

3.6 Anti-correlation between $\Delta(\mathbf{r})$ and $\Omega(\mathbf{r})$

A mysterious part of the story is the discovered anti-correlation between local superconducting gap and bosonic mode energy. The normalized correlation function between two functions $f(\mathbf{r})$ and $g(\mathbf{r})$ is defined as

$$C_{f,g}(\mathbf{R}) = \frac{\int [f(\mathbf{r}) - \bar{f}] \times [g(\mathbf{r} + \mathbf{R}) - \bar{g}] d^2\mathbf{r}}{\sqrt{A_{f,f}(0)A_{g,g}(0)}} \quad (3-10)$$

Where the autocorrelation $A_{f,f}(\mathbf{R})$ and $A_{g,g}(\mathbf{R})$ are defined as

$$A_{f,f}(\mathbf{R}) = \int [f(\mathbf{r}) - \bar{f}] \times [f(\mathbf{r} + \mathbf{R}) - \bar{f}] d^2\mathbf{r}$$

$$A_{g,g}(\mathbf{R}) = \int [g(\mathbf{r}) - \bar{g}] \times [g(\mathbf{r} + \mathbf{R}) - \bar{g}] d^2\mathbf{r} \quad (3-11)$$

This anti-correlation can be quite easily seen from the images of $\Delta(\mathbf{r})$ and $\Omega(\mathbf{r})$, as in Figure 3-5. The normalized zero-displacement correlation is about -0.30. However, there is a known source which causes gap disorder, dopant oxygen (see Chapter 2.6), where gap becomes larger when approaching dopant atoms. It is very logical to suspect that the anti-correlation between $\Delta(\mathbf{r})$ and $\Omega(\mathbf{r})$ is caused by dopant oxygen if near them $\Omega(\mathbf{r})$ diminishes. To test this hypothesis, an oxygen map was obtained by measuring conductance at $V=-0.96\text{V}$, at the same FOV where $\Delta(\mathbf{r})$ and $\Omega(\mathbf{r})$ are taken. The ability to keep the atomically sharp tip precisely registered at a FOV $\sim 40\text{nm}$ for over a week is essential. The result of this test rules out the dopant oxygen atoms as the source of $\Delta(\mathbf{r}) : \Omega(\mathbf{r})$ anti-correlation. Figure 3-9(a) shows the normalized correlation between position of oxygen dopants $O(\mathbf{r})$, local gap maxima $\Delta(\mathbf{r})$ and boson energy $\Omega(\mathbf{r})$. The zero-displacement correlation $C[\Delta(\mathbf{r}) : \Omega(\mathbf{r})] \approx -0.30$, while $C[O(\mathbf{r}) : \Omega(\mathbf{r})] \approx 0$, indicating that dopant oxygen does not affect mode energy and therefore, the mysterious anti-correlation between gap and mode energy must come

from other sources. Figure 3-9 (b) shows the two dimensional $\Delta\Omega$ histograms for ^{16}O and ^{18}O samples. The negative slope is just another way of showing the anti-correlation. As expected, the 2D histogram for ^{18}O is shifted down in Ω value. Note the $\bar{\Delta}$ is different, which is caused by different doping.

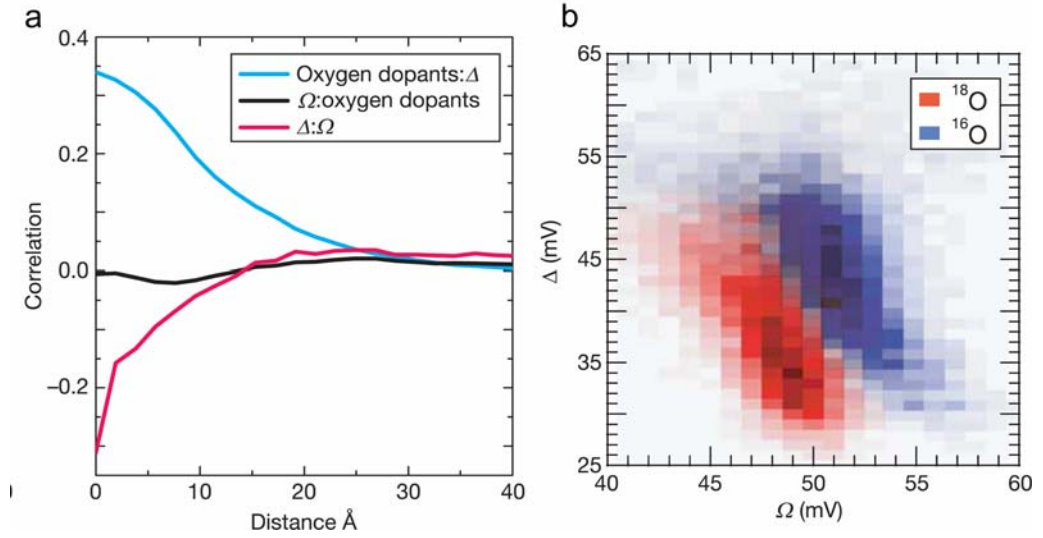


Figure 3-9 Anti-correlation between $\Delta(\mathbf{r})$ and $\Omega(\mathbf{r})$. (a) Normalized correlation between the dopant atom positions $\text{O}(\mathbf{r})$, local gap value $\Delta(\mathbf{r})$ and $\Omega(\mathbf{r})$. The zero-displacement correlation $C[\text{O}(\mathbf{r}) : \Delta(\mathbf{r})] \approx 0.35$, consistent with Ref. [46], and the gap-mode energy correlation $C[\Omega(\mathbf{r}) : \Delta(\mathbf{r})] \approx -0.30$. $\Omega(\mathbf{r})$ and $\text{O}(\mathbf{r})$ are not correlated. (b) The two dimensional $\Delta\Omega$ histograms of the frequency of occurrence of a given pair of (Δ, Ω) values in a single spectrum. The blue is for ^{16}O and red for ^{18}O . Ω is shifted down by a few meV with substitution of ^{16}O by ^{18}O . $\bar{\Delta}$ is different by 5.6 meV since the doping level for the two isotopes is different, with $^{16}T_c \approx 76\text{K}$ and $^{18}T_c \approx 88\text{K}$. The correlation analysis is made from 51219 and 60113.

Since the boson mode energy is correlated with the local gap maxima, and such relation cannot be simply explained by dopant oxygen effect, this boson must have important and direct impact on the electronic structure in the CuO_2 plane, where superconductivity occurs.

The last point is that such local disorder in $\Omega(\mathbf{r})$ is short ranged. As standard definition of coherence length, fit the distance dependence of autocorrelation function then define the e^{-1} decay as the coherence length. The electronic coherence length of was defined in early paper [40].

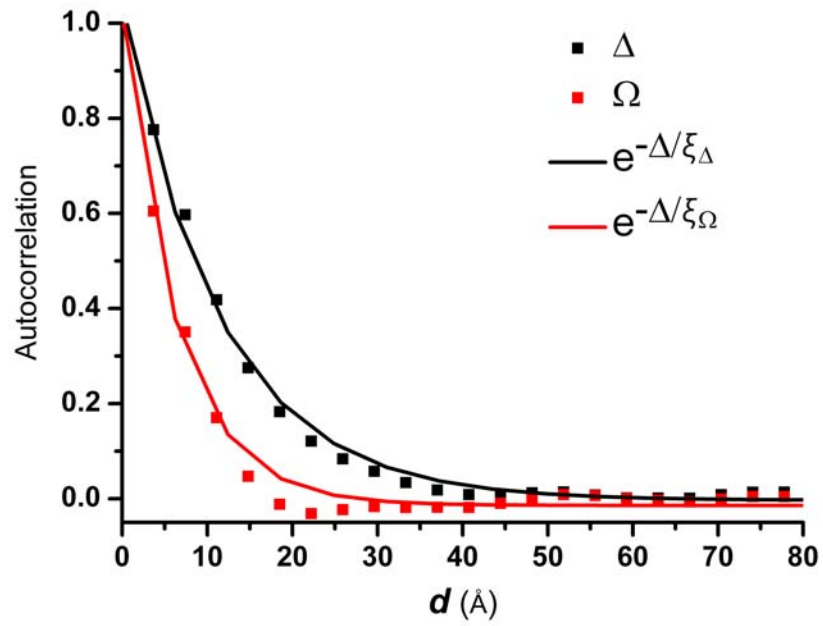


Figure 3-10 Coherence length of Δ and Ω . The autocorrelation $C(\mathbf{r})$ is calculated for both $\Delta(\mathbf{r})$ and $\Omega(\mathbf{r})$. The coherence length is obtained by using exponential decay $e^{-x/\xi}$ to fit $C(\mathbf{r})$. The fitted coherence length is $\xi_{\Delta} = 11.6 \text{ \AA}$ and $\xi_{\Omega} = 6.2 \text{ \AA}$.

From the plot, it is clear the coherence length of mode energy is $< 10 \text{ \AA}$, which is only about half of the coherence length of superconducting gap. This is another indicator the lattice mode detected by STM is highly localized vibrational mode, not quite the same as the phonon in the conventional sense, which is collective motion of lattice.

3.7 Discussoins

From the atomic resolution d^2I/dV^2 -imaging study in Bi-2212, important information about EBI, which is one of the central topics in cuprate research, is revealed. The discovery can be summarized as the following:

- (a) Boson mode energy is intensely disordered at nanometer scale, with the correlation length depending on doping.
- (b) Modulation in $d^2I/dV^2(\mathbf{r}, \omega)$ signatures strong interaction between the boson with antinodal quasiparticle. More importantly, such modulation only shows up after gap referencing $\omega(\mathbf{r}) = E - \Delta(\mathbf{r})$ to remove gap disorder.
- (c) Changing hole density has minimal effect on the average mode energy $\overline{\Omega}$.
- (d) Upon oxygen isotope substitution $^{16}\text{O} \rightarrow ^{18}\text{O}$, $\overline{\Omega}$ is reduced by about 6%, which is expected from the classical model of lattice vibration, where the natural frequency $\propto \sqrt{1/M}$.
- (e) There is moderate anti-correlation between $\Delta(\mathbf{r})$ and $\Omega(\mathbf{r})$, with zero-displacement correlation coefficient $C[\Delta(\mathbf{r}) : \Omega(\mathbf{r})] \approx -0.3$ for nearly optimal doping.

From these experimental observations, important deductions can be made and new questions raise.

From the energy range of the Ω , doping independence of Ω , and $^{16}\text{O}/^{18}\text{O}$ isotope effect on mode energy, lattice vibration mode is the logical candidate for the boson detected by d^2I/dV^2 -imaging. The mode energy detected in optimally doped Bi-2212 (^{16}O) spans over the range from 40meV to 65meV and centered at

$\bar{\Omega} = 52 \pm 1 \text{ meV}$ AND is doping independent. From INS result, the ‘resonant’ spin-1 mode has energy of 43 meV in optimally doped Bi-2212 and more importantly, is softened to 38 meV in the over doped regime [69]. The incommensurate spin density wave also has strong energy (dispersive) and doping dependence. For example, the high energy ($E \approx 85 \text{ meV}$) incommensurate peaks are rotated 45 degrees relative to the low energy ($E \approx 24 \text{ meV}$) peaks in $\text{YBa}_2\text{Cu}_3\text{O}_{6.6}$ [68], while the EBI detected in STM is dispersionless, always along antinodal direction. More decisively, the oxygen isotope induced mode energy reduction by $\sim 6\%$ upon substitution of ^{16}O for ^{18}O providing strong evidence that the boson detected in d^2I/dV^2 is some lattice vibration mode involving oxygen.

However, new questions arise. There are several new possibilities: (1) the gap disorder $\Delta(\mathbf{r})$ is induced by the heterogeneity in pairing potential, and such heterogeneity is caused by disorder in the frequencies $\Omega(\mathbf{r})$ (and coupling strength) of the oxygen related vibrational mode. However, gap strongly depends on doping while mode energy distribution remains the same across a wide range of hole density argues against the relevance of the detected mode to superconductivity. (2) The d^2I/dV^2 feature is not pairing EBI, for example, the inelastic stimulation of oxygen vibration mode in the tunneling barrier [79]. But the ubiquitous anti-correlation between $\Delta(\mathbf{r})$ and $\Omega(\mathbf{r})$ cannot be explained trivially. (3) The detected EBI is related to competing electronic orders to superconductivity, and the anti-correlation is a result of such competition. In the following chapters, experimental results will be presented to partly answer the questions.

CHAPTER 4

Impact of Periodic Variation of Inter-Atomic Distance on Superconductivity

Superconductivity exists in CuO_2 plane and T_c varies with hole concentration. This leads to extensive theoretical investigation of purely electronic mechanism of high- T_c . However, there is an apparent deficiency of such approach. As mentioned in Chapter 2, different families of cuprate which share the same in-plane electronic structure can have drastically different T_c . For example, in monolayer system, $T_{c,\text{max}} = 26\text{K}$ for $\text{Ca}_{2-x}\text{Na}_x\text{CuO}_2\text{Cl}_2$, while $T_{c,\text{max}} = 98\text{K}$ for $\text{HgBa}_2\text{CuO}_{4+\delta}$. Therefore, there must be an out-of-plane mechanism which controls the in-plane electronic structure.

Theoretically, Ohta *et al.* [80] emphasizes the critical role of apical oxygen O_{Apical} in controlling $T_{c,\text{max}}$ over different families of hole doped cuprates. In this theoretical model, the energy level of a hole on O_{Apical} relative to the level when it's on in-plane oxygen O_{plane} , ΔV_A , is the primary parameter to control electronic structure in CuO_2 plane. Within the picture that Zhang-Rice singlet [81] plays essential role in high- T_c superconductivity, more stable singlet gives higher T_c . The singlet stability is measured by parameter t , which is the energy difference between the ground state (bonding state) and the first excited state (anti-bonding state). t is in turn primarily determined by ΔV_A . Most importantly, ΔV_A sensitively depends on local structure.

Pavarini *et al.* [35] found the range of intralayer hopping is controlled by the structures perpendicular to CuO_2 plane. The distance between in-plane copper and O_{apical} , d_A is shown to directly control the ratio t'/t by changing the hybridization between Cu $4s$ and $\text{O}_{\text{apical}} 2p_z$ (t is the hopping integral along (1,0) and t' is the hopping integral along (1,1) direction), and hence influence $T_{c,\text{max}}$.

Experimentally, chemical substitution of cations of different radii is known to dramatically change T_c . For example, in doped La_2CuO_4 superconductor [82] $(\text{Ln}_{1-x}\text{M}_x)_2\text{CuO}_4$ (Ln^{3+} are lanthanoid and M^{2+} are Ca, Sr, Ba), T_c is found to decrease linearly with A-site disorder at the same doping, and increase rapidly with mean A-site cation radius $\langle r_A \rangle$. In Ln-Bi2201 ($\text{Bi}_2\text{Sr}_{1.6}\text{Ln}_{0.4}\text{CuO}_{6+\delta}$), T_c increases monotonically with increasing Ln^{3+} radius [37]. Since the substituted cations have the same valence, the primary effect is attributed to displacement of apical oxygen, and hence change the hopping parameter t'/t as proposed by Pavarini *et al.* [35]. Also it has been known for almost 20 years that hydrostatic pressure has large effect on T_c [34,83]. Although the microscopic explanation of pressure dependence of T_c is still lacking due to complicated material and temperature dependence [84], the pressure induced T_c change signatures importance of lattice in cuprate superconductivity.

The key structural element in cuprate is the CuO_5 pyramid (or CuO_6 octahedra in single layered compounds). Sitting at the apex of the pyramid is apical oxygen. In this chapter, the focus is on the effect of systematic perturbation of position of O_{apical} on superconductivity. The algorithm to precisely extract local unit cell distortion and account for lateral phase slip is developed by Dr. Slezak for his Ph.D. thesis, while me, Dr. Jinho Lee and Kazuhiro Fujita did most of the precision measurement.

4.1 Bulk Supermodulation in $\text{Bi}_2\text{Sr}_2\text{CaCu}_2\text{O}_{8+\delta}$

The motivation for the supermodulation study is that, it has been known for many years that the topographic imaging on BiO surface by STM shows incommensurate modulation (see Figure 4-1(a) and corresponding FFT in the inset). Also, it has been known that gap map $\Delta(\mathbf{r})$ also has similar modulation which can be easily seen by

eyes (see Figure 4-1(b) and FFT). In constant current imaging mode, STM does not directly detect the real crystal corrugation. The total current (as discussed in Chapter 1)

$$I = Ce^{-2\sqrt{\frac{2m_e\phi}{\hbar}}z} \int_0^{eV} \rho_s(\varepsilon) d\varepsilon \quad (4-1)$$

Hence to be exact, STM only detects local probability of wave function up to certain energy. However, structural corrugation, in metallic case, should dominate the tunneling probability because of the sensitive distance dependence of tunneling current (~ 10 times/ \AA). Therefore, the corrugation seen on BiO surface primarily represents the periodic structural modulation. The intriguing fact is that such structural modulation is also present in the energy scale closely related to superconductivity.

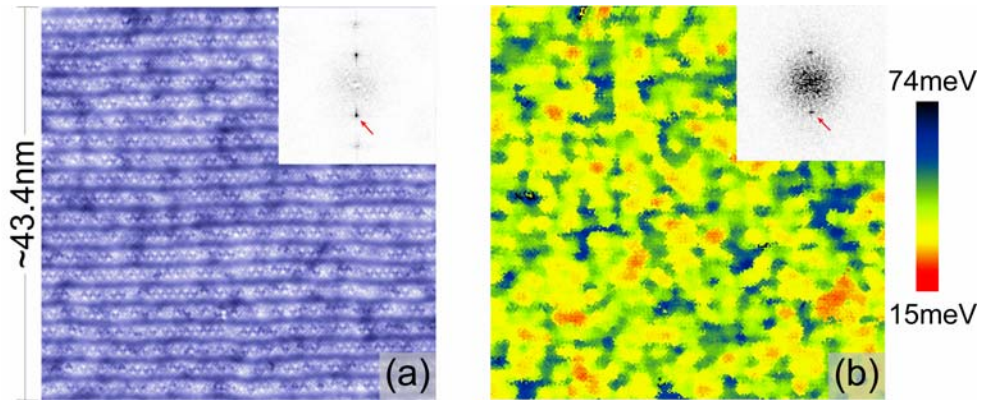


Figure 4-1 Same modulation in topograph and gap map. (Dataset 60614) (a) Constant current imaging of BiO layer for nearly optimally doped Bi2212. (b) Simultaneously obtained gap map $\Delta(\mathbf{r})$. Modulation in $\Delta(\mathbf{r})$ is accompanied by disorder induced by dopant oxygen. Insets in both panels: the Fourier transform of topograph and $\Delta(\mathbf{r})$. The arrows in the insets indicate the wavevector corresponding to the modulation seen in both images

In BSCCO ($\text{Bi}_2\text{Sr}_2\text{Ca}_{n-1}\text{Cu}_n\text{O}_{4+2n}$) family, there exists natural variation in unit cell dimensions [45,85-89]. This change in unit cell dimension is manifested as bulk

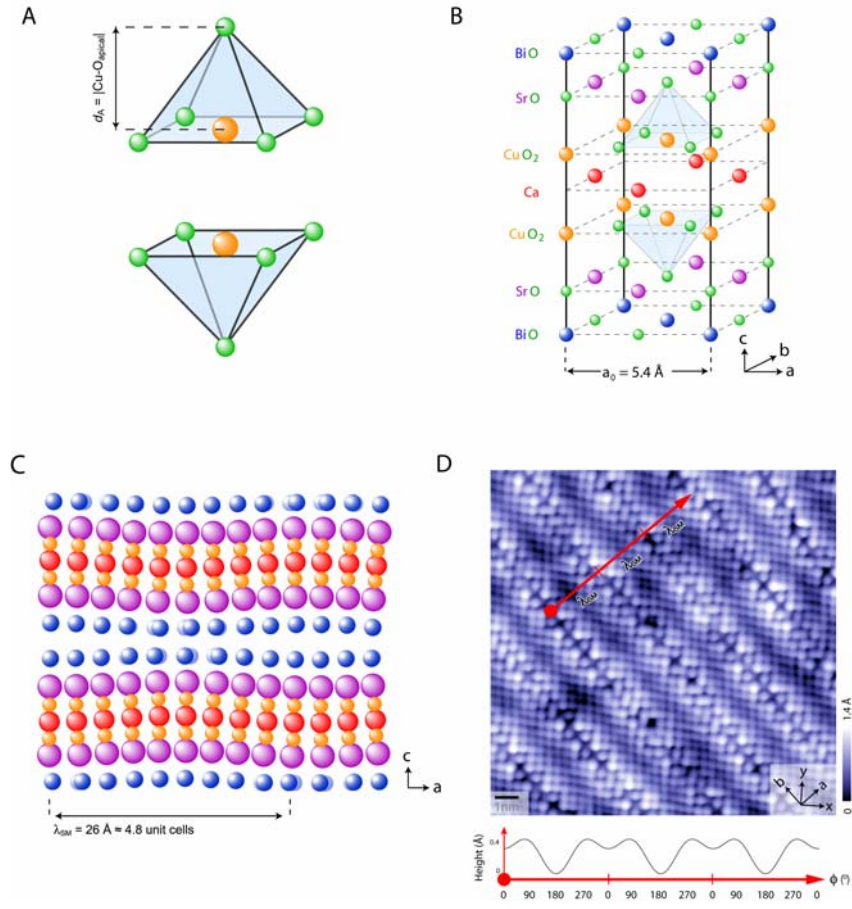


Figure 4-2 Crystal structure of Bi-2212 and the periodic unit cell distortion due to bulk incommensurate supermodulation. (A) The CuO_5 pyramid in the bi-layer system. Each apical oxygen sits at the apex of the pyramid. The distance d_A is the $\text{Cu-O}_{\text{apical}}$ bond length. (B) Crystal structure of top half of the unit cell. (The lower half is displaced along a -axis by $a_0/2$.) (C) Simulated supermodulation viewed along b -axis (oxygen atoms not included) according to crystallographic parameters in [45]. Note there is modulation both along a - and c -axis. (D) A representative 14.6 nm topographic image. The corrugation on the surface represents the bulk supermodulation along c -axis. The lower curve is the simulated topographic height by using first and second harmonics.

incommensurate modulation, called ‘supermodulation’. This modulation is along a -axis and the period is about 26 Å. Figure 4-2 shows the crystal structure and simulated bulk supermodulation. In Bi-2212, each unit cell contains 2 CuO_2 layers, 2 SrO layers,

2 BiO layers and 1 Ca layer. The effect of the modulation is to displace the atoms from their average position within each unit cell almost sinusoidally, with Bi and Sr atoms displaced both along a - and c -axis by up to 4\AA , and Cu atoms mainly along c -axis by up to 3\AA [85]. This modulation is believed to arise from mismatch of in-plane lattice spacing between different layers. Now consider the change in distance between various atoms in a unit cell due to supermodulation. Among those the Cu related bond length change is the most important. Figure 4-3 shows the bond length as function of supermodulation phase simulated from the structure refinement.

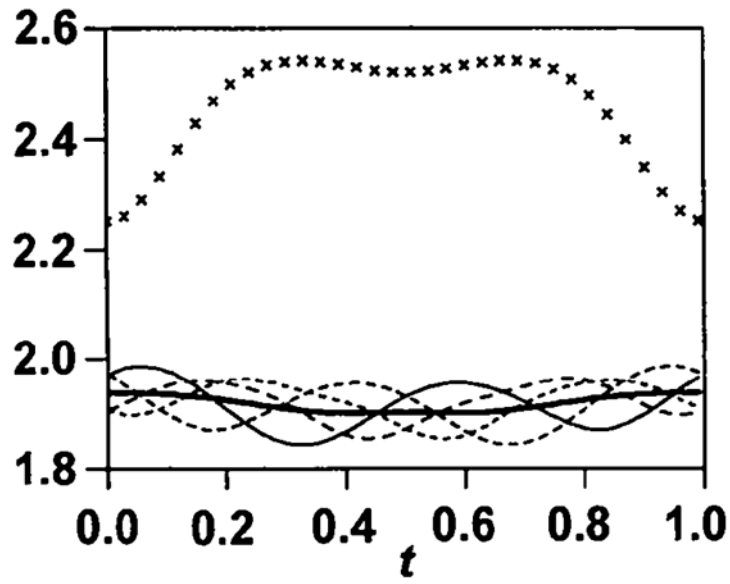


Figure 4-3 Cu related bond length as function of supermodulation (1.0 means phase of 2π). Cross: Cu-O_{apical} distance d_A . Dashed: Cu-O_{plane} distance. Bottom solid line: the averaged in-plane Cu-O distance.

The modulated displacement of μ th atom in a unit cell is described by [45] :

$$\mathbf{U}_i^\mu(x^\mu) = \sum_{n=0}^2 (A_{i,n}^\mu \cos 2\pi n x^\mu + B_{i,n}^\mu \sin 2\pi n x^\mu) \quad (4-1)$$

$$\text{Where } x^\mu = \mathbf{q}_{SM} \bullet \mathbf{r}_0^\mu \quad (4-2)$$

\mathbf{r}_0^μ is the average position of the μ th atom. In addition, there is occupancy probability of the site μ . \mathbf{q}_{SM} is the supermodulation wavevector and can be written as $\mathbf{q}_{SM} = q_1 \mathbf{a}^* + q_2 \mathbf{b}^* + q_3 \mathbf{c}^*$, where $\mathbf{a}^*, \mathbf{b}^*, \mathbf{c}^*$ are reciprocal vectors of the lattice, $q_1 \approx 0$, $q_2 \approx 0.212$, $q_3 \approx 1$ [87].

$$\mathbf{P}^\mu(x^\mu) = \sum_{n=0}^2 (A_{i,n}^\mu \cos 2\pi n x^\mu + B_{i,n}^\mu \sin 2\pi n x^\mu) \quad (4-3)$$

Figure 4-3 is the simulated result using the refinement parameter in Ref. [45]. The detailed structural analysis from literature is done in [90]. The key results from crystallography are:

- (1) The biggest change in Cu related bond length due to supermodulation is d_A , the Cu-O_{apical} distance (see Figure 4-2(A)).
- (2) There is considerable second harmonic variation.

4.2 Extracting Local Supermodulation Phase

To quantify the effect of supermodulation on superconductivity, one needs to establish the functional relation between these two quantities. The first thing to do is to uniquely label each point on the topograph by a quantity which defines supermodulation. Then sort the local gap value according to such quantity. For a periodic function, the phase is such quantity. The real line cut from the topograph along \mathbf{q}_{SM} direction contains other high frequency components. The primary high frequency signal comes from Bi atoms (O is invisible in topograph). Hence the phase

cannot be simply defined by measuring the distance between maxima and minima. A more serious problem is the supermodulation meanders (Figure 4-1 (a)) and the phase slips. For a perfect periodic function with wavevector \mathbf{q}_{SM} , the phase of each point \mathbf{r} can be uniquely defined as

$$\varphi(\mathbf{r}) = 2\pi\mathbf{q}_{SM} \bullet \mathbf{r} \quad (4-4)$$

With the phase slip, at each point there is slight deviation from the perfect phase predicted by (4-4). Denote this deviation by $\theta(\mathbf{r})$. Hence the resulting local phase $\phi(\mathbf{r})$ is the sum:

$$\phi(\mathbf{r}) = 2\pi\mathbf{q}_{SM} \bullet \mathbf{r} + \theta(\mathbf{r}) = \varphi(\mathbf{r}) + \theta(\mathbf{r}) \quad (4-5)$$

A technique called ‘phase map’ is then developed by Dr. Slezak (details in his thesis [90]). Here I list the main procedures and the result of each step.

A typical topograph is shown in Figure 4-4 (a). The quasi-parallel dark lines are the minima of the supermodulation distortion. Starting with the topograph, do the following:

- (1) Take the topograph $Z(\mathbf{r})$, and Fourier filter. The FFT $[Z(\mathbf{r})]$ consists of several major features: atomic peaks, first and second harmonics of supermodulation (see Figure 4-4 (b)). Only take the Fourier component of first harmonic of supermodulation (\mathbf{q}_{SM} and with finite variation to account for the phase slip) and perform the inverse Fourier filter. After this operation, 4-4 (c) is produced.

- (2) From Figure 4-4 (c), it is easy to see the meander and phase slip of the supermodulation. This image contains both the ‘perfect part’ and the phase slip and is proportional to $\cos[2\pi\mathbf{q}_{SM} \bullet \mathbf{r} + \theta(\mathbf{r})]$
- (3) Generate “reference” image $\cos(2\pi\mathbf{q}_{SM} \bullet \mathbf{r})$ and $\sin(2\pi\mathbf{q}_{SM} \bullet \mathbf{r})$, which is defined by the perfect phase $\mathbf{q}_{SM} \bullet \mathbf{r}$ (Figure 4-4 (d)).
- (4) Multiply the Fourier filtered image 4-4 (c) by the reference images 4-4 (d) and then low pass filter the result. The effect of this operation is similar to what a lock-in amplifier does to pick up signal amplitude of certain frequency. Now we are dealing with “spatial frequency \mathbf{q}_{SM} ”.

$$\underbrace{\cos(2\pi\mathbf{q}_{SM} \bullet \mathbf{r})}_{\text{reference}} \bullet \underbrace{\cos[2\pi\mathbf{q}_{SM} \bullet \mathbf{r} + \theta(\mathbf{r})]}_{\text{with phase slip}} = \frac{1}{2} [\cos(4\pi\mathbf{q}_{SM} \bullet \mathbf{r} + \theta(\mathbf{r})) + \cos(\theta(\mathbf{r}))] \quad (4-6)$$

$$\underbrace{\sin(2\pi\mathbf{q}_{SM} \bullet \mathbf{r})}_{\text{reference}} \bullet \underbrace{\cos[2\pi\mathbf{q}_{SM} \bullet \mathbf{r} + \theta(\mathbf{r})]}_{\text{with phase slip}} = \frac{1}{2} [\sin(4\pi\mathbf{q}_{SM} \bullet \mathbf{r} + \theta(\mathbf{r})) - \sin(\theta(\mathbf{r}))] \quad (4-7)$$

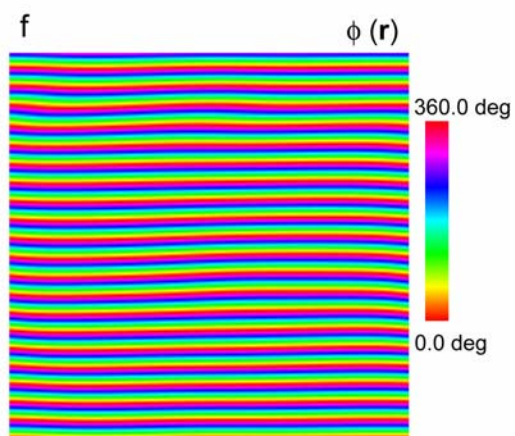
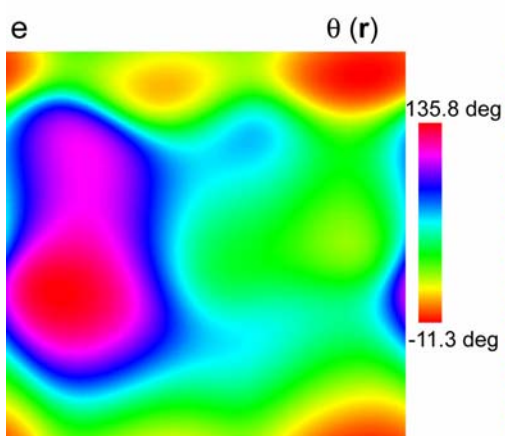
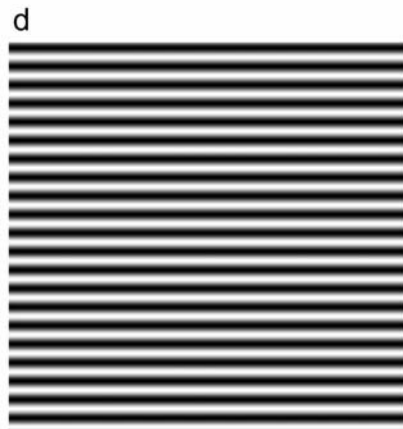
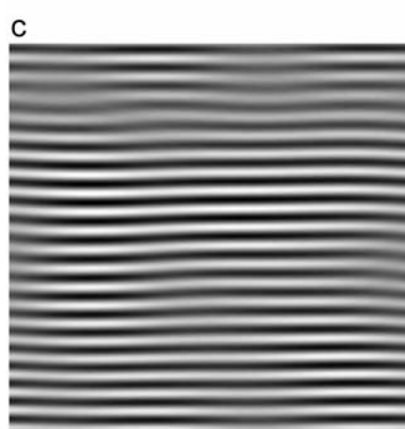
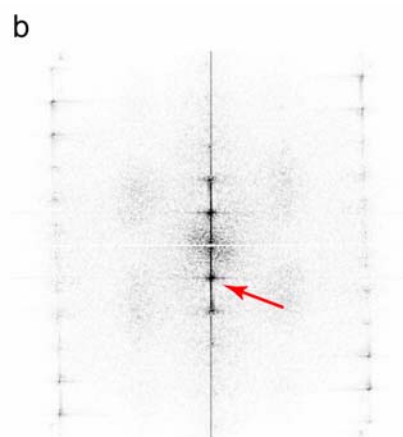
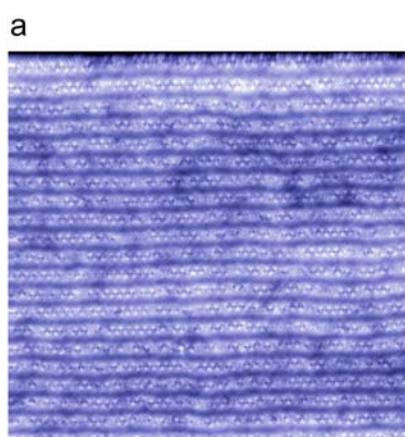
Low pass filter the result in (4-6) and (4-7), we get $\sin(\theta(\mathbf{r}))$ and $\cos(\theta(\mathbf{r}))$.

Taking arctan of the ratio $\sin(\theta(\mathbf{r}))/\cos(\theta(\mathbf{r}))$, $\theta(\mathbf{r})$ can be uniquely determined.

- (5) Figure 4-4 (e) shows the local phase shift $\theta(\mathbf{r})$. Note, due to periodicity, large phase shift like 357° and 3° are equivalent.
- (6) Figure 4-4 (f) shows the final result for local phase map $\phi(\mathbf{r})$. The maxima of supermodulation distortion is defined as $\phi = 0^\circ$ and the minima is defined as $\phi = 180^\circ$. Figure 4-5 overlays the lines of constant phase $\phi = 0^\circ$ on the topograph, to show the accuracy of this algorithm.

After precisely labeling the local supermodulation phase, we can now examine the relation between electronic structure and unit cell distortion.

Figure 4-4 Illustration of phase map technique. (a) Topographic imaging of BiO plane. The spatial resolution is about 40nm:256pixel. (b) Fourier transformed image of topograph (a). The arrow points to the wavevector \mathbf{q}_{SM} for first harmonic of supermodulation. (c) The Fourier filtered topograph which only contains the modulation $\mathbf{q}_{SM} + \Delta\mathbf{q}$, where $\Delta\mathbf{q}$ is the small variation which describe the phase slip. (d) The perfect reference image $\cos(2\pi\mathbf{q}_{SM} \bullet \mathbf{r})$. Another reference image $\sin(2\pi\mathbf{q}_{SM} \bullet \mathbf{r})$ is also needed to determine $\theta(\mathbf{r})$ but not shown here. (e) The phase shift $\theta(\mathbf{r})$ determined from lock-in technique. (f) The resulting total local phase $\phi(\mathbf{r}) = 2\pi\mathbf{q}_{SM} \bullet \mathbf{r} + \theta(\mathbf{r})$.



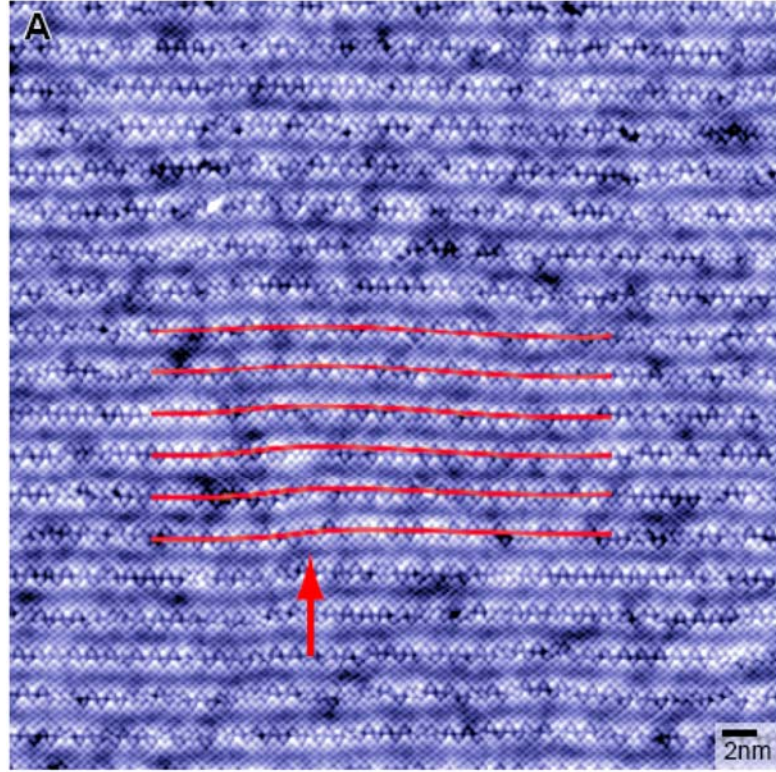


Figure 4-5 Illustration of precision of phase map algorithm. This figure shows a topograph. The red lines are the lines of constant local phase $\phi = 0^\circ$.

4.3 Impact of Periodic Unit Cell Distortion on Superconductivity

With the phase map technique to accurately determine local supermodulation phase ϕ , we can now quantitatively analyze the relation between unit cell dimension and the pairing gap.

To systematically study the supermodulation effect, samples at different doping are examined. Figure 5-6 shows the topograph, gap map and the corresponding Fourier transformed images. The modulation in gap with wavevector \mathbf{q}_{SM} is universal across wide range $p \sim 0.13, 0.15$ and 0.17 .

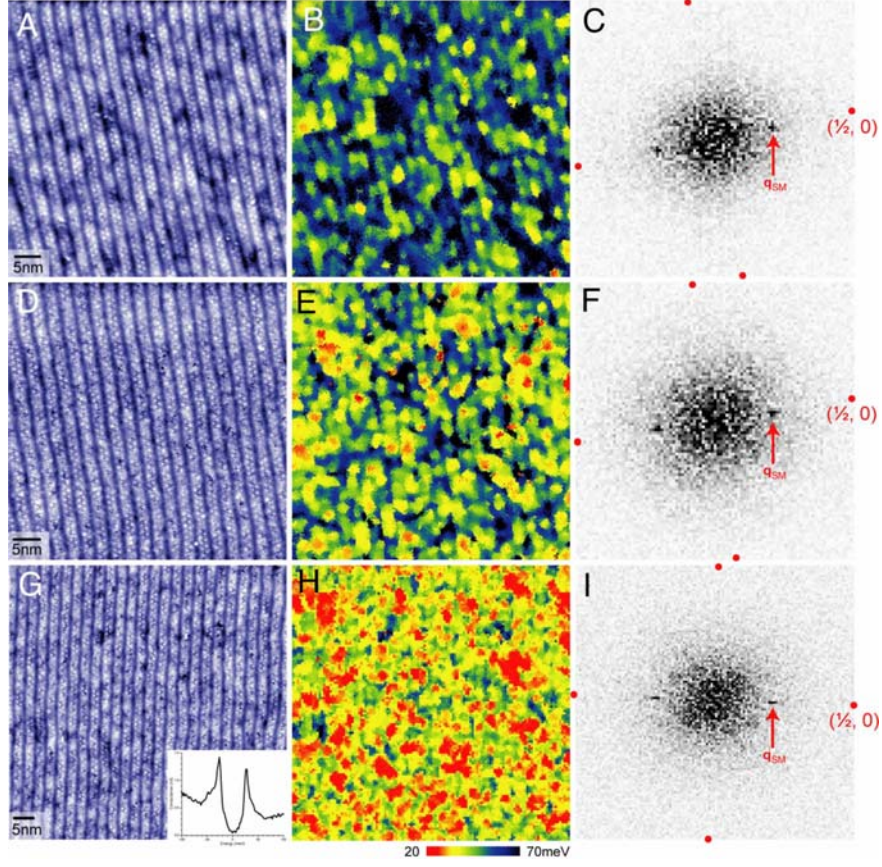


Figure 4-6 Gap modulations at the same wavevector \mathbf{q}_{SM} as bulk modulation across different doping levels. (A), (D) and (E): Topographic images of different doping Bi-2212, with $p \sim 0.13, 0.15, 0.17$ respectively. (B), (E) and (H): Gap maps corresponding to the adjacent topographs (A), (D) and (E), with mean gap value 50mV, 47mV and 37mV. (C), (F) and (I): Fourier transformed images of gap maps (B), (E) and (H), all showing the supermodulation peak \mathbf{q}_{SM} as indicated by the red arrows.

Next, phase map is made based on the simultaneously obtained topographic images shown in Figure 4-6, with bin size 5° . All spectra and corresponding local gap $\Delta(\mathbf{r})$ are averaged for each discretized ϕ . Figure 5-7 shows the result of phase averaged pairing gaps. Figure 4-7 (A), (C) and (E) show the 2D-histograms $\Delta: \phi$. The color scale represents the normalized probability that one can find a spectrum with gap value Δ and lie in the position with local supermodulation phase $\phi \pm 2.5^\circ$. The 2D-

histograms show quite wide spread, but it is clear that there is moderate modulation of the gap size with high probability for a given value of ϕ .

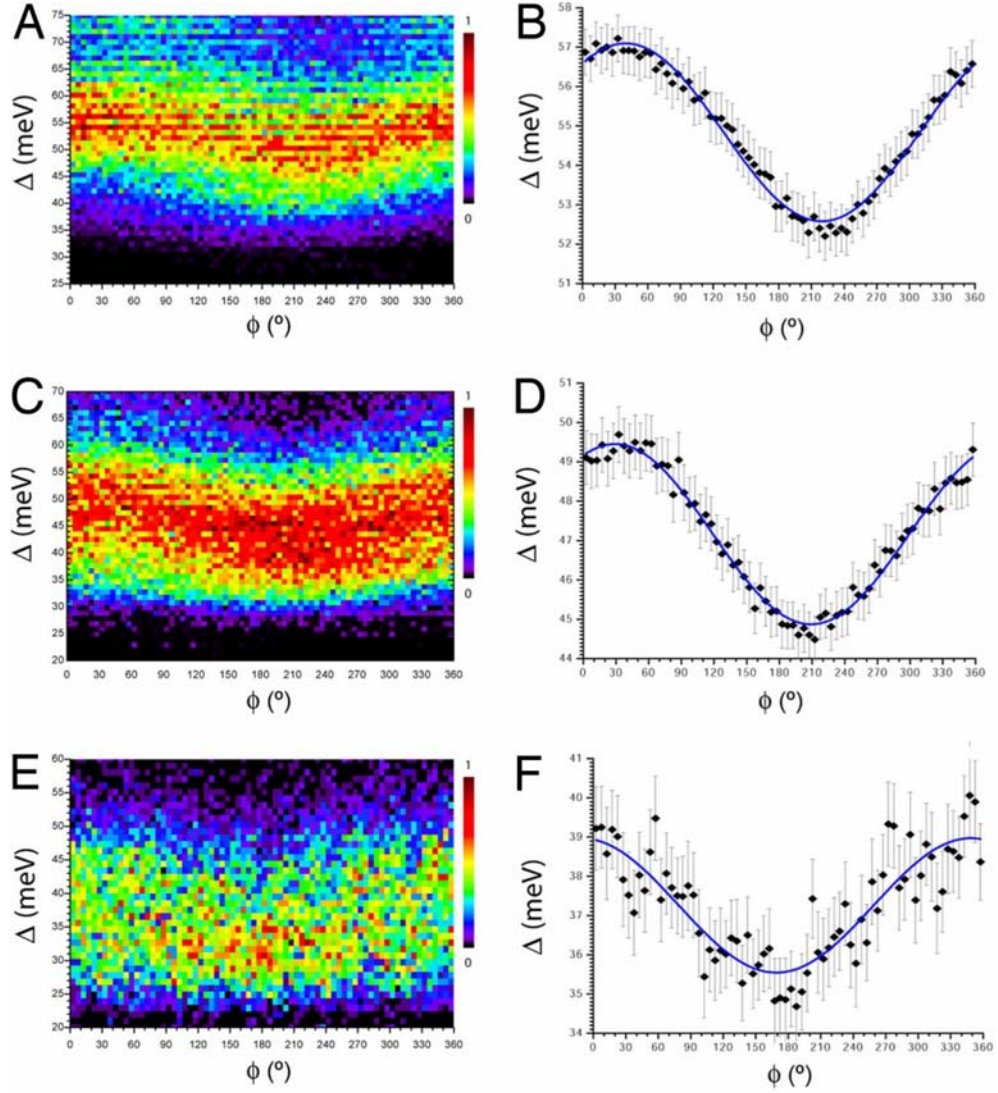


Figure 4-7 Gap magnitude as a function of crystal supermodulation phase. (A), (D) and (E): Normalized 2D-histograms showing the probability that certain gap value Δ occurs at a given local supermodulation phase ϕ for underdoped (A), optimally doped (D) and overdoped (E) samples. (B), (D) and (F): Scattered plots are the mean gap value for each ϕ with error bar representing 95% confidence interval. The blue lines are the fit by first harmonic function $\Delta = \Delta_0 + A\cos(\phi + \vartheta)$.

The local gap disorder $\Delta(\mathbf{r})$ shows co-sinusoidal variation with supermodulation phase ϕ . The fit lines clearly show that on average, gap maxima occur around $\phi = 0^\circ$ and minima occur around $\phi = 180^\circ$. As discussed earlier, the biggest change within a unit cell induced by bulk supermodulation is the Cu-O_{apical} distance d_A , which varies by as much as 12%. It is widely accepted that such change in d_A is because the modulation along c -axis has greater amplitude in CuO₂ plane than in the adjacent SrO layer. d_A is minimal at supermodulation maxima $\phi = 0^\circ$ and maximal at supermodulation minima $\phi = 180^\circ$. Therefore, the local pairing gap $\Delta(\mathbf{r})$ is anti-correlated with d_A .

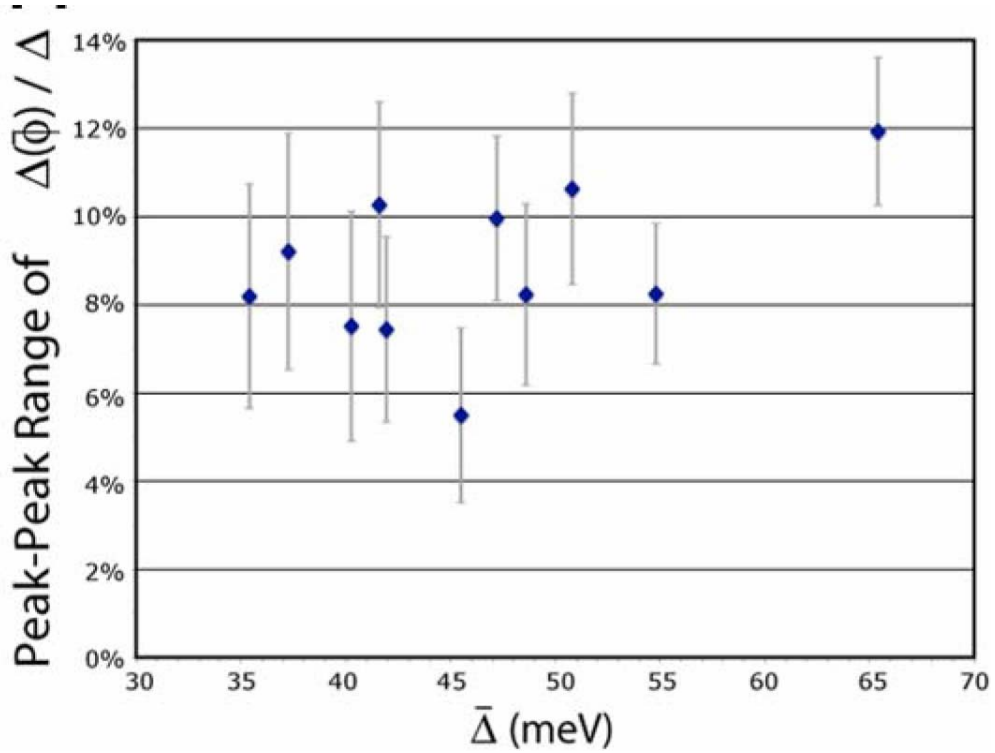


Figure 4-8 Relative amplitude $2A$ (peak to peak) of the co-sinusoidal fit. There is no apparent relationship to hole density.

In order to take into account the varying mean gap value for different doping levels, we use the relative peak to peak modulation amplitude of $\Delta(\phi)$, $2A/\bar{\Delta}$, to define the

strength of gap variation. The relative modulation amplitude is found to be insensitive to hole density, about $9\pm 2\%$. Figure 4-8 shows the scatter plot of relative amplitude as function of doping levels (mean gap $\bar{\Delta}$). There's no clear doping dependence.

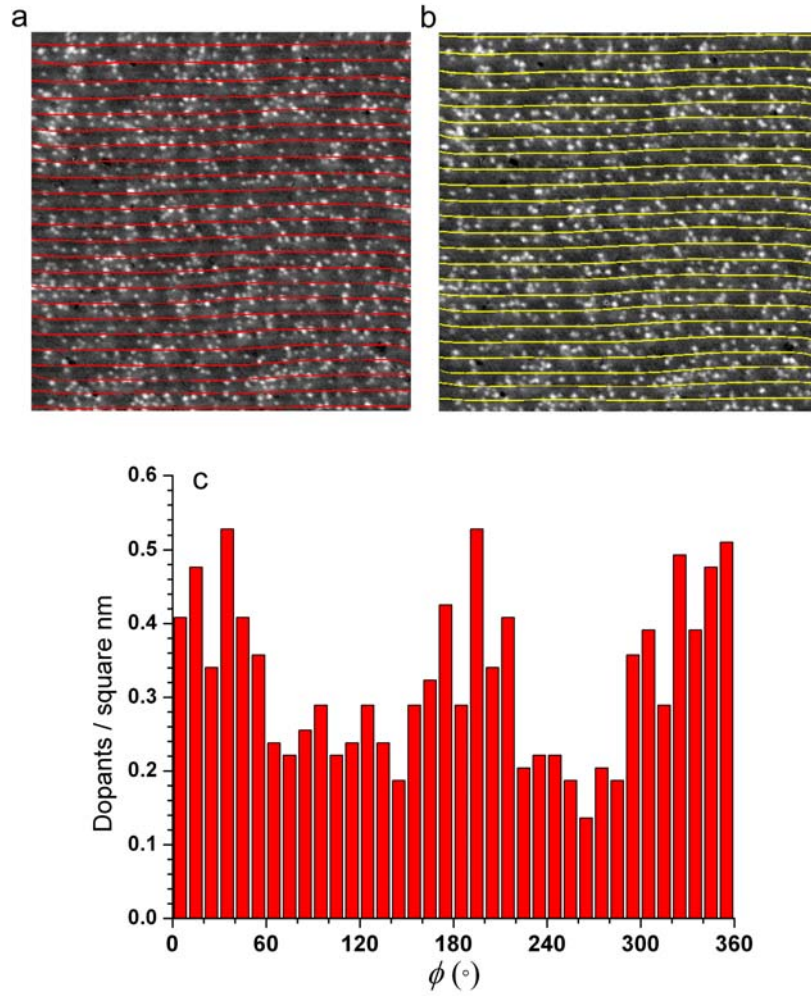


Figure 4-9 Dopant density modulation. (a) and (b): High energy map $g(\mathbf{r}, V \sim -0.9V)$ which identifies the dopant induced impurity states overlaid with the lines tracing out constant phase $\phi = 0^\circ$ (a) and $\phi = 180^\circ$ (b). (c) Dopant impurity state density vs. supermodulation phase. This double-peaked distribution is found in every doping studied.

The immediate question is, if dopant oxygen population is modulated by supermodulation, since gap size is correlated with the position of the dopant atoms, the observed gap modulation $\Delta(\phi)$ could be the result of dopant density modulation. In order to differentiate those possibilities, we took topographic image, gap map and oxygen dopant map $g(\mathbf{r}, V \sim -0.9V)$ (as described in Chapter 2) on the same FOV. Applying phase map procedure on the topograph, we can generate lines tracing out constant phase. Choose the representative ones, $\phi = 0^\circ$ (supermodulation maxima) and $\phi = 180^\circ$ (supermodulation minima) and overlay the traces on the oxygen map, there is no obvious change in the number of dopants near to the supermodulation maxima and minima (Figure 4-9 (a)-(b)). Sorting the number of dopants according to supermodulation phase ϕ and plot the dopant density vs ϕ to find the probability of finding a dopant induced state at given ϕ , it turns out that density of dopants and ϕ are correlated. However, dopant density peaks at both $\phi = 0^\circ$ and $\phi = 180^\circ$ (See Figure 5-9 (c)). $\Delta(\phi)$ only has one peak around $\phi = 0^\circ$, therefore dopant density modulation as the primary cause of gap modulation at \mathbf{q}_{SM} can be ruled out.

Although dopant atom is not the cause of gap modulation, the details of variation of conductance $g(V)$ near to dopant atoms and that due to supermodulation show great similarity. To reveal the effect of dopant atom on superconducting spectra, an dopant distance map is developed. For each point on oxygen dopant map, one can define a distance d to the nearest dopant atom. All points can be labeled uniquely by a particular value $d(\mathbf{r})$. Then, the spectra having the similar d value are averaged.

A dopant oxygen map $g(\mathbf{r}, V=-0.96V)$ is obtained on a FOV about 40nm (Figure 4-10 (a)), then a gap map $\Delta(\mathbf{r})$ is taken on the identical FOV (Figure 4-10 (b)). The algorithm to calculate $d(\mathbf{r})$ is implemented to generate the dopant distance map $d(\mathbf{r})$

(Figure 4-10 (c)) and finally, we can average gap size $\Delta(\mathbf{r})$ according to different d values and hence obtain the average gap size as function of distance to the dopant atoms (Figure 4-10 (d)). On average, the mean gap value falls by $>7\text{mV}$ within distance to the dopant atom of $\sim 2\text{nm}$.

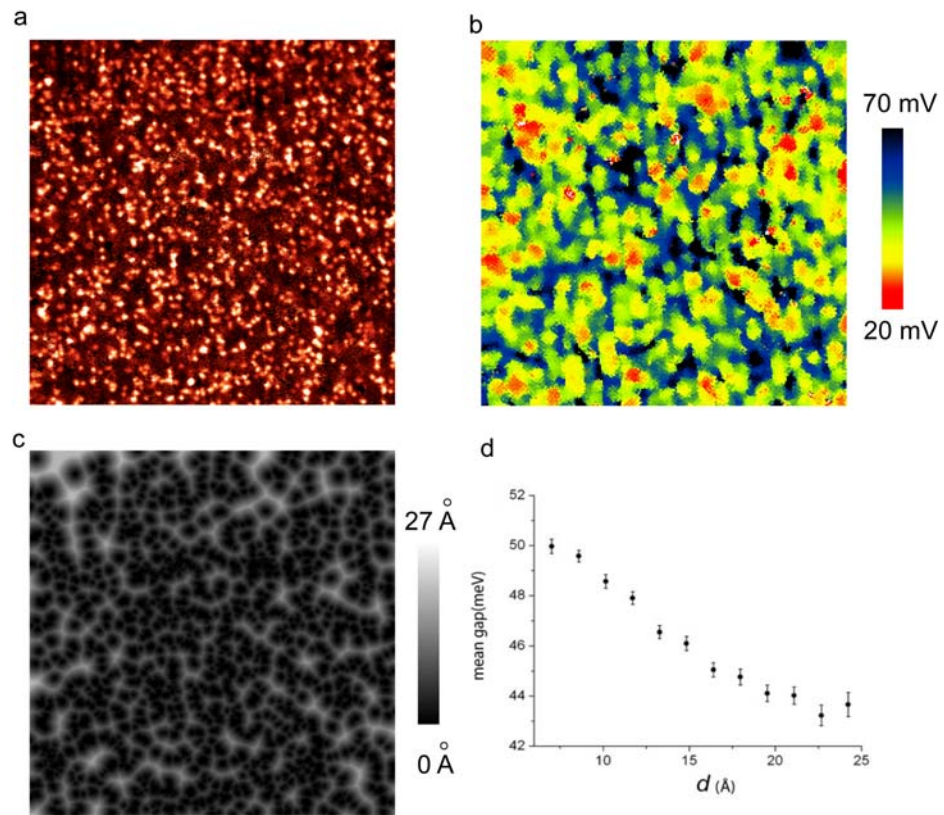


Figure 4-10 $\Delta(\mathbf{r})$ as a function of distance to dopant atoms. (a) Conductance map $g(\mathbf{r}, V=-0.9\text{V})$ of oxygen dopant induced impurity states. (b) Gap map $\Delta(\mathbf{r})$ at the identical FOV as (a). (c) The map $d(\mathbf{r})$, the distance to nearest dopant atoms for each point. (d) d -averaged gap value using the gap map (b) and distance map (c). Data is from 41023 and 41026.

To further examine the details, we use the above map $d(\mathbf{r})$ and phase map $\phi(\mathbf{r})$ to sort spectra and make average. The result is shown in Figure 4-11. As approaching the

dopant atoms, the gap size increases and the superconducting peak height diminishes with significant broadening (Figure 4-11 (b)). Going from supermodulation minima $\phi = 180^\circ$ to maxima $\phi = 0^\circ$, evolution of spectra is indistinguishable from the effect caused by dopant atom.

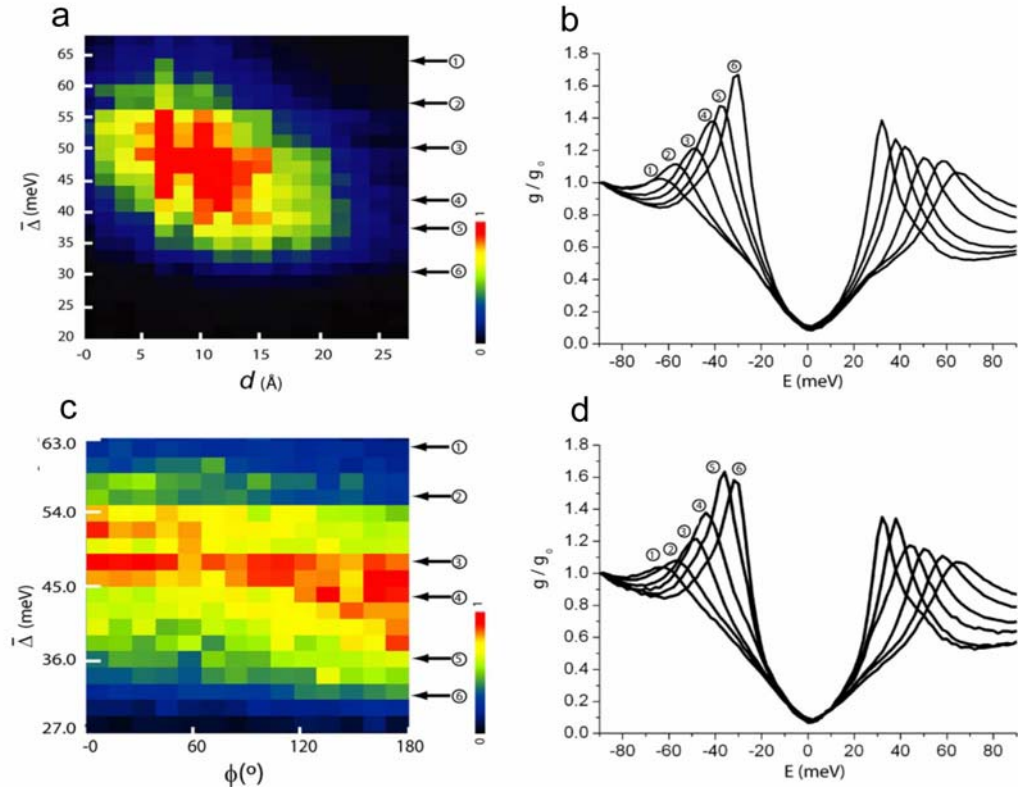


Figure 4-11 Spectra evolution as response to dopant atom and supermodulation. (a) 2D-histogram of gap values vs. d . (b) Average spectra associated with different nearest dopant atom distance d as in (a). (c) Gap magnitude sorted by the phase of the supermodulation. (d) Average spectra sorted by different supermodulation phase, as labeled in (c). It should be emphasized that the spectra in (b) and (d) are not sorted by gap values. Arrows in (a) and (c) are guides to indicate the resulting average gap values after the spectra are sorted by d and ϕ , respectively.

4.4 Discussion and Conclusions

When only the first harmonic of the crystal refinement is considered, pairing gap Δ is modulated co-sinusoidally by the periodic change in unit cell dimensions of Bi-2212. The maximal gap Δ occurs around minimal Cu-O_{apical} distance d_A and the minimal Δ occurs around maximal d_A . The relative gap modulation amplitude is found to be $\sim 9 \pm 1\%$ cross different doping levels.

There is theoretical proposal of ‘pair density wave’ (PDW) [91-94], a density wave associated with d -wave Cooper pair, particle-hole symmetric in Fourier transformed LDOS $\rho(\mathbf{q}, \omega)$, with rotational charge symmetry $4a \times 4a$ near doping level $x=1/8$. The modulation of gap along \mathbf{q}_{SM} , although does not satisfy the symmetry of a PDW described by theory, does represents the periodic variation of d -wave Cooper pair strength and provide a new opportunity to study PDW.

It has been shown that the response of spectra to randomly distributed dopant atom and systematic variation of unit cell dimension is indistinguishable. That is, getting closer to dopant atom or decreasing d_A both increase pairing gap and suppress the coherence peak height (and broaden the peak width). It is therefore reasonable to empirically assign a same mechanism to both phenomena. Hirschfeld [95] proposed that the primary effect of dopant oxygen is to tilt the CuO₅ pyramid in Bi-2212, and particularly, displace apical oxygen by as much as 0.5Å (See Figure 5-12). Using density functional theory (DFT), they show a sharp concentration of states on dopant oxygen around -1.0eV, which agrees remarkably well with the STM observed states around -0.96V. There also has been calculation based on single and multiple impurity Bogoliubov-de Gennes equation, suggesting the pair interaction is modulated locally by dopant atom. This calculation generated numerical results that have crucial

features observed in STM: strongly disordered gap $\Delta(\mathbf{r})$, anti-correlation between gap value and peak height, small charge modulation, correlation between dopant oxygen position and gap size and its short correlation length. The discovery of supermodulation effect on gap size points to the local distortion of lattice, involving either alteration of d_A or tilting of CuO_5 cage, as a key factor to the electron pairing process.

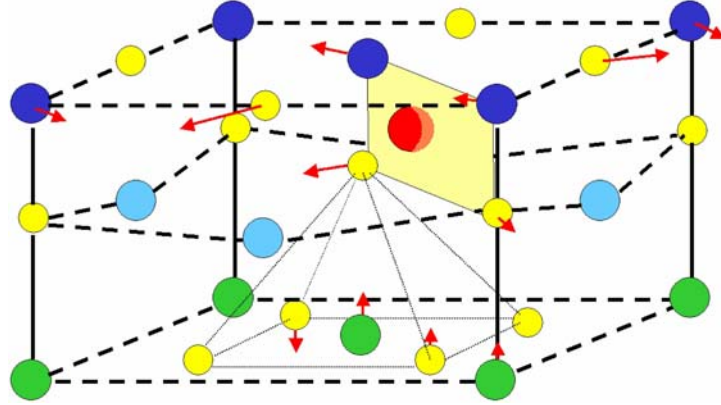


Figure 4-12 Local lattice distortion due to dopant oxygen. Taken from [95]. Red: dopant oxygen, Light blue: Sr, Yellow: stoichiometric oxygen, Green: Cu, Blue: Bi.

Yin and Ku [96] used a LDA+ U and Wannier function to emphasize the importance of energy level of apical oxygen $2p_z$ orbital \mathcal{E}_{p_z} . A ‘super-repulsion’ term V_{ij} is introduced with the effect to weaken local pairing strength. Dopant oxygen and supermodulation both perturb the energy level of apical oxygen \mathcal{E}_{p_z} , which in turn modulates V_{ij} and thus the pairing gap Δ . Yang *et al.* [97] use t - t' - J model within renormalized mean field theory to account for correlation. They reproduced the modulation in Δ by periodically varying t , t' , J along the bulk supermodulation. However in their model, the modulation in t' leads to significant carrier density modulation. Also, they ascribed the random gap disorder to Sr/Bi intersubstitution, which the experiment by STM shows is not the case [98].

There are two types of hybridization. One is in plane, between $\text{Cu } 3d_{x^2-y^2}$ and $\text{O } 2p_{\sigma}$, which is obviously important, for the superconductivity to form and charge carrier (like Zhang-Rice singlet) to propagate. The hybridization along axial direction, which is between the apical oxygen $2p_z$ and in-plane orbital (for example $\text{Cu } 4s$), is also important. The out-of-plane effect generated by local change of unit cell dimension suggests that pairing in high- T_c superconductivity may occur at atomic scale, and more numerically extensive microscopic description is needed to fully understand the experimental observations.

CHAPTER 5

Impact of Periodic Unit Cell Distortion on Electron-Lattice Coupling

STM has revealed important new information about electron-lattice interaction and the impact of local lattice distortion on superconductivity, as in Chapter 3 and Chapter 4. However, the previous study also raises many new questions to be answered. To test the effect of lattice, the most direct way is to perturb the lattice and measure the response. In supermodulation study [99], lattice is perturbed by periodic unit cell distortion. Besides this intrinsic lattice distortion in BSCCO family, there is another well established method to explore lattice impact, isotope substitution. By changing the ionic mass M , the lattice vibration frequency is changed. Isotope effect has played a central role in identifying phonon as pairing glue in BCS superconductor, as described in previous chapters. In high- T_c superconductor, due to the strong local disorder, careful study of isotope effect at atomic scale may be a key to understand lattice's role in pair formation.

5.1 Remaining Questions from Previous Electron-Lattice Study

After publishing, Ref. [100] stimulates wide discussions to re-evaluate the possible role lattice is playing in pair formation.

- Validity of isotope shift in mode energy

Some stated the concern whether the isotope shift in average mode energy $\bar{\Omega}$ is genuine, since the doping level between the two isotope sample reported in Ref. [100] is quite different, and therefore, the shift in mode energy $\bar{\Omega}$ may be caused by different carrier concentration [101,102].

- The origin of the dip-hump feature observed in d^2I/dV^2
 - (1) Pilgram *et al.* [79] proposed a model where the feature seen in d^2I/dV^2 is caused by inelastic tunneling stimulation of apical oxygen vibration mode in the barrier layers, and hence is not relevant to high- T_c superconductivity. Yang *et al.* [97] further pointed out the anti-correlation between Δ and Ω is due to supermodulation and hence such anti-correlation could be consistent with inelastic stimulation proposal by Pilgram.
 - (2) By fitting the distribution of mode energy from STM data, Hwang *et al.* [103] claimed that the bosonic mode detected by STM is mixture of lattice vibration and magnetic mode. The distribution can be divided into two populations. One remains unchanged with changing hole density (lattice mode), while the other one shifts with different doping (magnetic mode).
- Supporters for phonon
 - (1) Balatsky and Zhu [104] proposed a local version of strong-coupling d -wave superconductivity with inhomogeneous bosonic mode. They successfully reproduced anti-correlation between Δ and Ω . They also calculated coupling strength λ which turns out to have the BCS form.
 - (2) X.-J. Chen *et al.* [105] developed a phonon mediated, d -wave BCS like model to explain the dependence of T_c and isotope coefficient α on doping level, number of CuO₂ layers, pressure and lattice distortion.
 - (3) Egami [106] argues that the Cu-O bond stretching phonon might be the one observed in STM, which softens when entering superconducting state in YBCO as observed in INS; the mechanism involves more than one degree of freedom.

We want to address the following remaining questions:

Is the oxygen isotope shift in Ω [100] caused by different doping? Is the d^2I/dV^2 peak caused by stimulation of apical oxygen vibrational mode through inelastic tunneling? Does the anti-correlation between $\Delta(\mathbf{r})$ and $\Omega(\mathbf{r})$ point to non-BCS explanation or lattice does not have effect on superconductivity? How does QPI change upon $^{16}\text{O}/^{18}\text{O}$ substitution? What is the relationship between Δ and Ω within unit-cell and how does this relationship change with isotope substitution? In order to tackle those questions, isotope experiment will be an ideal test. Oxygen isotope substituted Bi-2212 at the same doping is prepared and carefully studied.

5.2 Review of Isotope Effect in High- T_c Superconductor

BCS theory has a simple prediction for isotope effect in T_c . In the BCS model, T_c is proportional to phonon frequency [10]:

$$k_B T_c = 1.13 \hbar \omega_c e^{-1/N(0)V} \quad (5-1)$$

The electron-phonon interaction V doesn't depend on frequency, and $\omega_c \propto \sqrt{1/M}$. Take log on both sides gives:

$$\ln T_c = \ln M^{-1/2} + C \quad (5-2)$$

The isotope coefficient for T_c is then defined as

$$\alpha = \frac{\Delta(\ln T_c)}{\Delta(\ln M)} \quad (5-3)$$

It is easy to see, from the standard weak coupling BCS theory, $\alpha = -0.5$. The negative sign is important, that means T_c should be higher for lighter isotopic superconductor.

As a marker for phonon mechanism on BCS superconductivity, isotope effect attracted large interest ever since the discovery of high- T_c superconductor. However, the situation is much more complicated (will only discuss hole doped case).

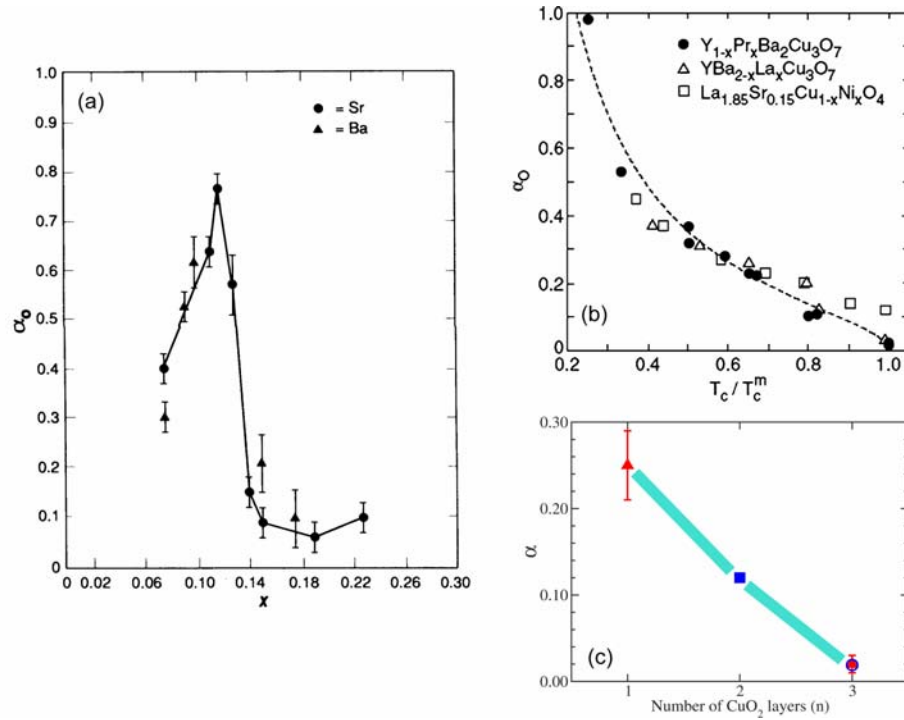


Figure 5-1 Doping and layer number dependence of isotope effect in T_c . (a) Oxygen isotope effect as function of x in $\text{La}_{2-x}\text{Ba}_x\text{CuO}_4$ and $\text{La}_{2-x}\text{Sr}_x\text{CuO}_4$, from Crawford *et al.* [107]. (b) Oxygen isotope component α_O vs. normalized $\tilde{T}_c = T_c/T_{c,\text{max}}$ for various families of cuprate. [101,108] (c) Isotope coefficient as function of number CuO_2 layers for optimally doped BSCCO, from Chen *et al.* [102].

In $\text{La}_{2-x}(\text{M}_x)\text{CuO}_4$ based superconductor ($\text{M}=\text{Sr}, \text{Ba}$), α is found to be very small (<0.1) at optimal and over doping, but increases drastically when hole concentrations goes

down and peaked around $x \approx 0.12$ [107] . This anomalous peak in α coincides with the structural phase transition from low temperature orthorhombic (LTO) to low temperature tetragonal (LTT) AND the suppression of T_c at $x = 1/8$ anomaly. This observation reveals the close link between the structural instability, doped holes and superconductivity. There is also a universal trend of α as function of normalized T_c in Y123 family and La_2CuO_4 system [101,108]. See Figure 5-1(a) and (b).

For optimally doped BSCOO family, $\text{Bi}_2\text{Sr}_2\text{Ca}_{n-1}\text{Cu}_n\text{O}_{2n+4+\delta}$, the isotope coefficient α is found to be dependent on number of layers [102], see Figure 5-1(c), with the coefficient smallest in trilayered compound and largest in single layered one.

Besides isotope shift in T_c , cuprates also exhibit unusual isotope effect on superfluid density ρ_s (or penetration depth λ). In standard BCS theory, there is no isotope shift in ρ_s . However, change in in-plane penetration depth λ_{ab} has been observed in YBCO and LSCO [109-113]. The penetration depth and ρ_s is related by

$$\rho_s = \frac{1}{\lambda_{ab}^2} = \mu_0 e^2 \frac{n_s}{m_{ab}^*} \quad (5-4)$$

The observed isotope change in λ_{ab} has been attributed to the change of effective in-plane charge carrier mass m_{ab}^* , rather than the change in charge carrier density. A careful study by Zhao, Hunt, Keller and Müller [110] suggests the existence of polaronic supercarriers in LSCO. Their main finding is that the structural phase transition temperature T_s (from LTO to LTT at $x=0.105$) does not change upon oxygen isotope substitution. This implies there is only very small difference in normal charge carrier density n , since T_s is very sensitive to n . Therefore, the supercarrier density n_s doesn't have significant change because of conservation of total particle number $n+n_s$.

On the other hand, there is about 4% change in λ_{ab} , therefore the logical deduction is this isotope shift in penetration depth is caused by change in effective mass m_{ab}^* . This finding implies the supercarrier mass is dependent on ionic mass M , consistent with the picture that polaronic charge condensates into superconducting state.

As summarized above, the unconventional isotope effects both on T_c and ρ_s point to the unconventional role of lattice in cuprate. In the following sections, the detailed study of isotope effect at atomic scale in optimally doped Bi-2212 will be presented.

5.3 Oxygen Isotope Effect on Gap and Mode Energy in Optimally Doped Bi-2212

Although the average mode energy $\bar{\Omega}$ has minimal change upon changing hole concentration and hence it is legitimate to compare $\bar{\Omega}$ of ^{16}O and ^{18}O with different doping, it is nevertheless important to verify this result for the same doping.

$^{16}\text{O}/^{18}\text{O}$ Bi-2212 at optimal doping is prepared by Dr. Fujita. To check the quality of the isotope substitution, magnetization measurement is done for ^{16}O , ^{18}O and for the re-substituted sample $^{18}\text{O} \rightarrow ^{16}\text{O}$. The result is shown in Figure 5-2. The midpoint estimation of T_c gives $T_c=89\text{K}$ for ^{16}O and $T_c=88\text{K}$ for ^{18}O . This 1K shift in T_c is consistent with that reported by Gweon *et al.* [114]. By re-substituting ^{16}O for ^{18}O , T_c shifts back to 89K. Note that the diamagnetic signal for the two isotopes are different, which might signal the penetration depth difference.

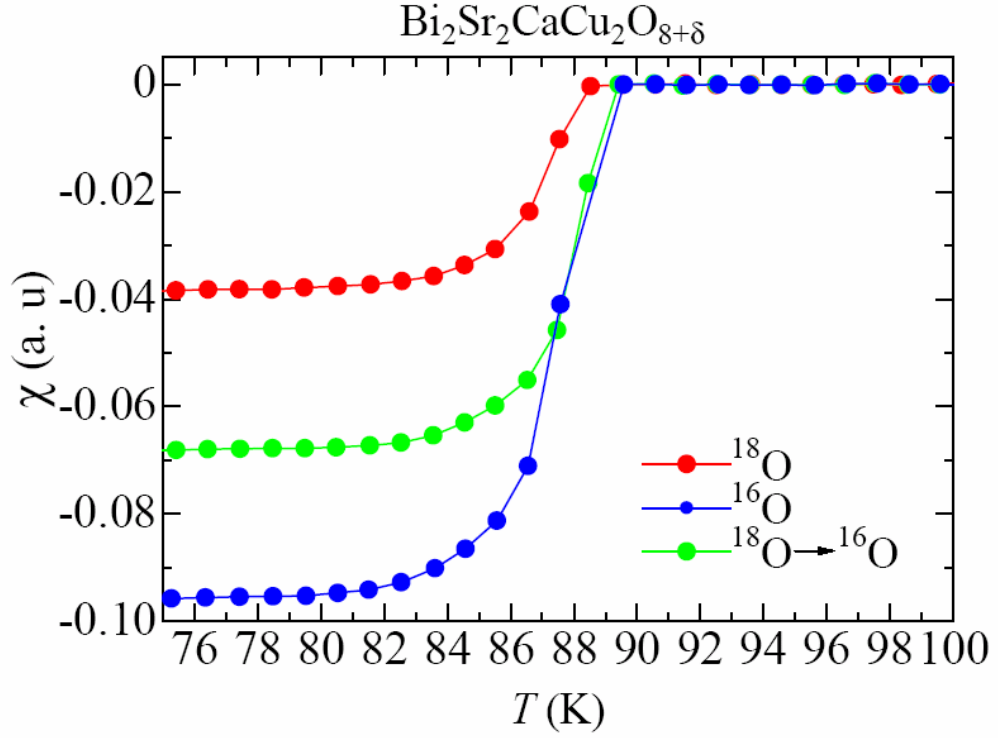


Figure 5-2 Magnetization measurement for $^{16}\text{O}/^{18}\text{O}$ substitution. $T_c=89\text{K}$ for ^{16}O and $T_c=88\text{K}$ for ^{18}O . Re-substitute ^{16}O for ^{18}O brings T_c to 89K .

To check whether $^{16}\text{O}/^{18}\text{O}$ inter-substitution is complete, Raman spectroscopy is performed. See figure 5-3. The mode energies corresponding to in-plane oxygen and apical oxygen vibration modes both have shifts by about 5%, close to the classical shift $\sim 6\% = 1 - \sqrt{\frac{16}{18}}$. Thus by this simple estimation, most in-plane and apical oxygen are replaced successfully. This Raman spectroscopy work is done by T. Masui and S. Tajima at Osaka University, Japan. Figure 5-3(a) shows the isotope shift for B_{1g} and A_{1g} phonon which involves in-plane and apical oxygen vibration respectively, and Figure 5-3(b) shows Raman scattering for A_{1g} phonon during $^{16}\text{O} \rightarrow ^{18}\text{O} \rightarrow ^{16}\text{O}$ substitution. The phonon mode frequency shifts back to the original ^{16}O value, showing the quality of the isotope substitution process.

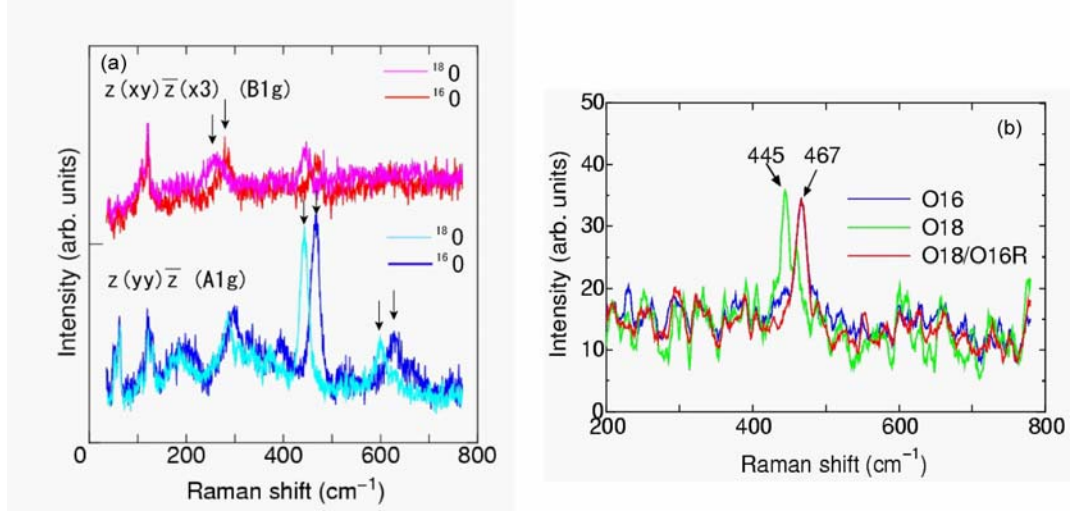


Figure 5-3 Raman scattering evaluation of isotope substitution. (a) Raman shift of B_{1g} and A_{1g} phonon frequency for oxygen isotopes. *Top*: B_{1g} phonon frequency around 280 cm⁻¹ for ¹⁶O (red) is shifted to lower value for ¹⁸O (pink), as indicated by arrow. This mode is assigned to out-of-plane motion of in-plane oxygen. *Bottom*: Phonon frequency of A_{1g} symmetry around 450 cm⁻¹ and 620 cm⁻¹ for ¹⁶O (blue) also shifts to lower value for ¹⁸O (cyan), as indicated by arrows. Corresponding phonons are vibration of oxygen in BiO plane and apical oxygen, respectively. Energy shift of each peak by ¹⁶O → ¹⁸O exchange are estimated as ~5 %, which is closer to that of expected energy shift about 6% ($\approx 1 - \sqrt{16/18}$). (b) Back substitution from ¹⁸O → ¹⁶O brings the phonon frequency back to the original value, hence verifies the reliability of this isotope exchange process.

Having confidence of the substitution process, now we can compare the gap and mode energy distribution for ¹⁶O/¹⁸O samples. Figure 5-4 shows $\Delta(\mathbf{r})$, $\Omega(\mathbf{r})$ and distributions of them for both isotope samples. The left panels shows the result for ¹⁶O and the right panels shows result for ¹⁸O. In order to get more reliable statistics, for both ¹⁶O and ¹⁸O, Δ and Ω values measured at different locations but on the same sample are combined together to generate histograms. From the absolute color scale, it is easy to see that $\bar{\Delta}$ remains unchanged while $\bar{\Omega}$ is shifted to lower value upon ¹⁸O substitution. The arithmetic average for gap and mode energies are: $\bar{\Delta} = 40.9\text{mV}$ (¹⁶O) and $\bar{\Delta} = 41.9\text{mV}$ (¹⁸O); $\bar{\Omega} = 51.3\text{mV}$ (¹⁶O) and $\bar{\Omega} = 47.0\text{mV}$ (¹⁸O).

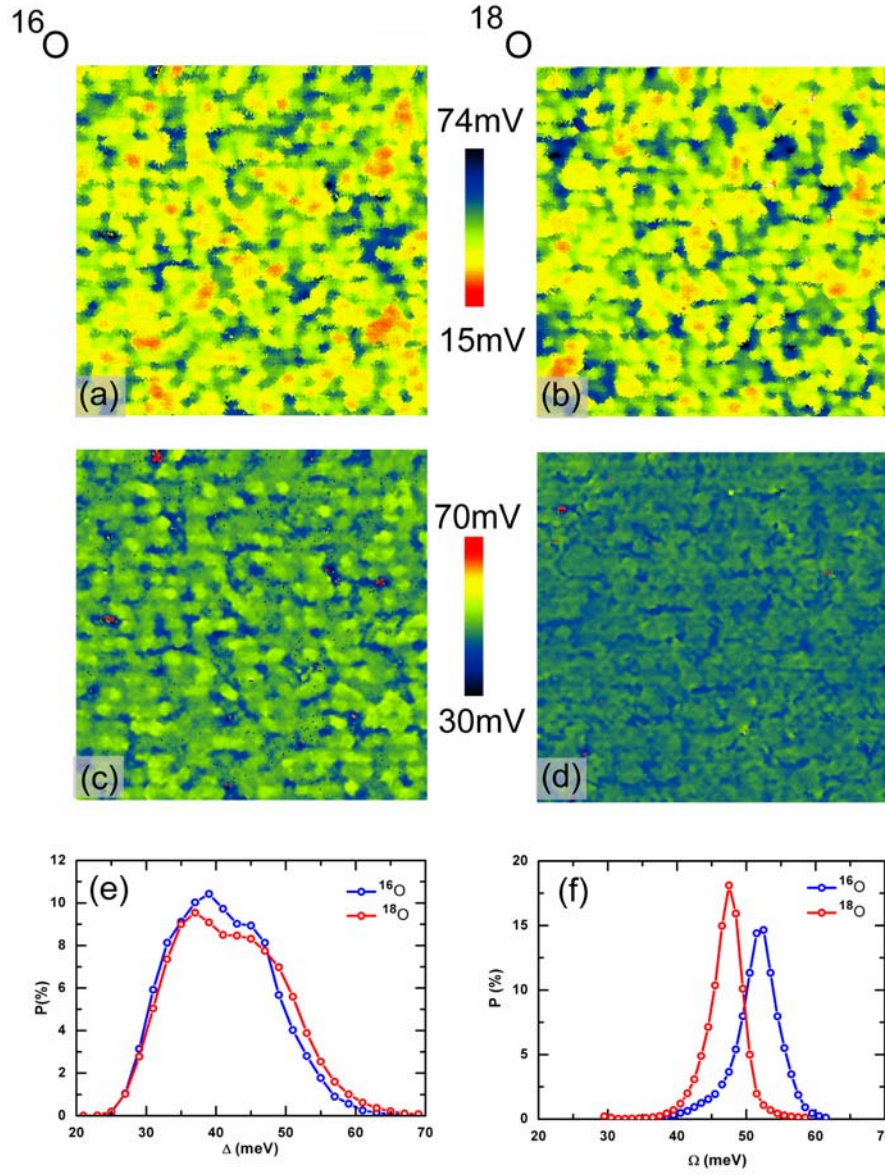


Figure 5-4 Δ and Ω distribution for optimally doped $^{16}\text{O}/^{18}\text{O}$ Bi-2212. (a)-(b) Gap map $\Delta(\mathbf{r})$ for ^{16}O and ^{18}O , respectively. (c)-(d) Mode energy map $\Omega(\mathbf{r})$ for ^{16}O and ^{18}O , respectively. These are from datasets 60614 (^{16}O) and 51219 (^{18}O). (c) The combined Δ -histogram for ^{16}O and ^{18}O . ^{16}O Δ -histogram compiled from: 60603, 60611, 60614, 60617, 60629; ^{18}O Δ -histogram compiled from 51127, 51210, 51216, 51222, 51225, 60116. The histograms for the two isotopes have very slight change, with $\bar{\Delta} = 40.9\text{mV}$ (^{16}O) and $\bar{\Delta} = 41.9\text{mV}$ (^{18}O). (d) The combined Ω -histogram for ^{16}O and ^{18}O . ^{16}O Ω -histogram compiled from: 60603, 60611, 60614; ^{18}O Ω -histogram compiled from 51127, 51210, 51219, 51225. The histograms for the two isotopes have very slight change, with $\bar{\Omega} = 51.3\text{mV}$ (^{16}O) and $\bar{\Omega} = 47.0\text{mV}$ (^{18}O).

Hence we've shown that the isotope shift reported in [100] is not due to different doping level.

5.4 Effect of Periodic Unit Cell Distortion on Electron-Lattice Coupling

Surprisingly, there is also weak modulation in $\Omega(\mathbf{r})$ (in both isotope samples), which can be seen by eyes in Figure 5-4(c) and (d). The Fourier transformed image of $\Delta(\mathbf{r})$ and $\Omega(\mathbf{r})$ all show the same wavevector \mathbf{q}_{SM} . Figure 5-5 shows example of such similarity in optimally doped Bi-2212.

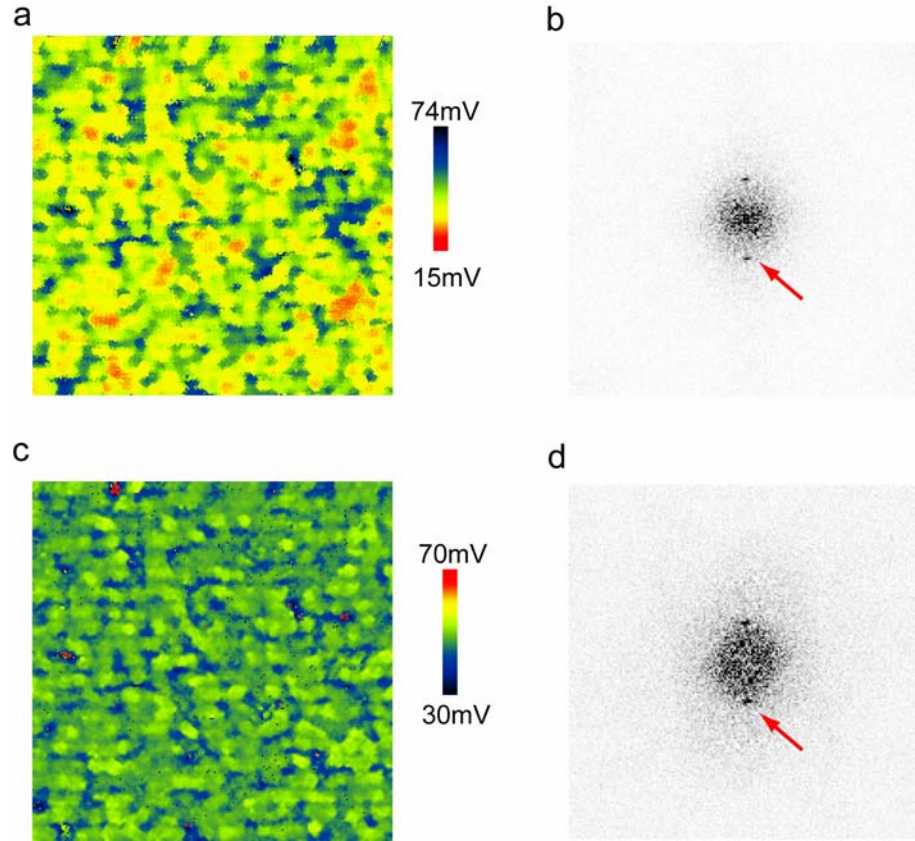


Figure 5-5 $\Delta(\mathbf{r})$ and $\Omega(\mathbf{r})$ both modulate with \mathbf{q}_{SM} . From 60614. (a)-(b) Gap map and its Fourier transform $\Delta(\mathbf{q})$. (c)-(d) Mode energy map and its Fourier transform $\Omega(\mathbf{q})$. The red arrows in (b) and (d) indicate supermodulation wavevector \mathbf{q}_{SM} .

As discussed in Chapter 4, to quantify the relation between $\Omega(\mathbf{r})$ and local lattice distortion labeled by ϕ , one needs to obtain local supermodulation phase by using the phase map technique. After generating phase map $\phi(\mathbf{r})$ and averaging $\Delta(\mathbf{r})$ and $\Omega(\mathbf{r})$ according to ϕ with bin size 5° , we get relations $\Delta(\phi)$ and $\Omega(\phi)$. The representative result is shown in Figure 5-6.

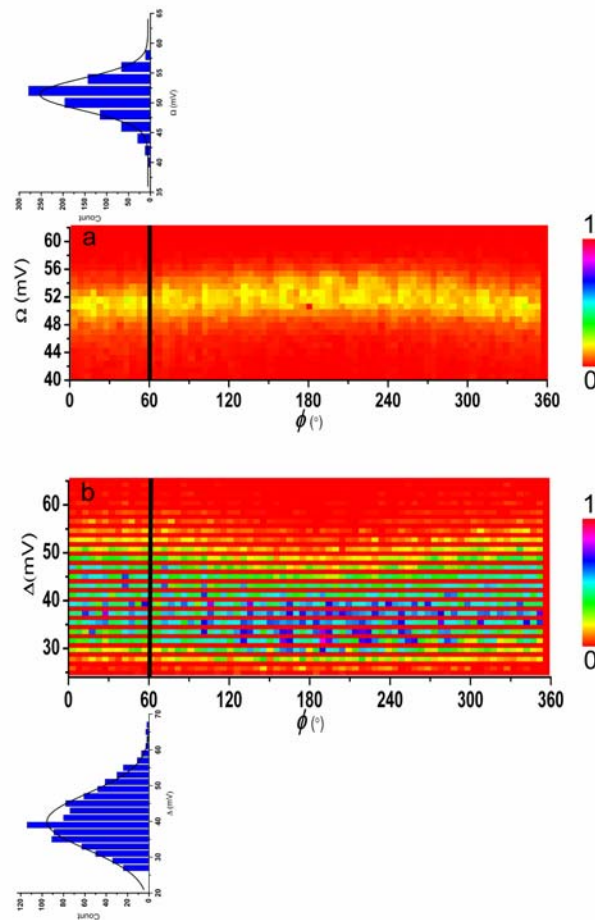


Figure 5-6 Probability of occurrence of Δ and Ω as function of supermodulation phase ϕ . (a) Normalized probability that for a given ϕ (within 5° window), certain gap value Δ can be found. (b) (a) Normalized probability that for a given ϕ (within 5° window), certain gap value Ω can be found. The distribution above and below the histogram: the distribution of Δ and Ω for $\phi = 60^\circ$, respectively. There are total 933 counts for both cases.

The whole idea of the gap map process is to find the average effect of bulk supermodulation. The conclusion is based on statistics. As shown in Figure 5-6, for each ϕ value with a bin size 5° , there is distribution of Δ and Ω . The effect of lattice is best described by the variation of average values $\bar{\Delta}$ and $\bar{\Omega}$ as function of supermodulation phase ϕ . Note the average here is the average of Δ and Ω for a particular value of ϕ , not the spatial average. For each distribution, we get the estimated mean value $\bar{\Delta}(\phi)$ and $\bar{\Omega}(\phi)$, and need to estimate the robustness of them, i.e. we need to know the likelihood of our estimation. Since for each ϕ value, there are several hundreds of Δ and Ω values, the statistics to estimate confidence interval (C.I.) can be used to construct the error bars in the plot. The process is as following:

Suppose we have a distribution of Δ for certain phase ϕ , of total N points. The mean of this distribution is $\bar{\Delta}$, and the true expectation value μ of such distribution (assume infinite number of points can be obtained). μ is unknown but can be estimated by $\bar{\Delta}$. The 95% C.I. is defined as the interval $\{\bar{\Delta} - \delta : \bar{\Delta} + \delta\}$ that 95% probability the true expectation value μ will fall within it. Since it is a large number problem, we can consider that $\bar{\Delta}$ is normally distributed with expectation value μ , but with the standard error σ / \sqrt{N} . We use the standardized random variable

$$Z = \frac{\bar{\Delta} - \mu}{\sigma / \sqrt{N}} \quad (5-4)$$

For standard normal distribution,

$$P(-1.96 < Z < 1.96) = 95\% \quad (5-5)$$

Hence, using $\delta = 1.96 \frac{\sigma}{\sqrt{N}}$, we can define the error bar for $\bar{\Delta}(\phi)$.

Figure 5-7 shows the relation $\bar{\Delta}(\phi)$ and $\bar{\Omega}(\phi)$, with error bars not the standard deviation σ , but the 95% C. I..

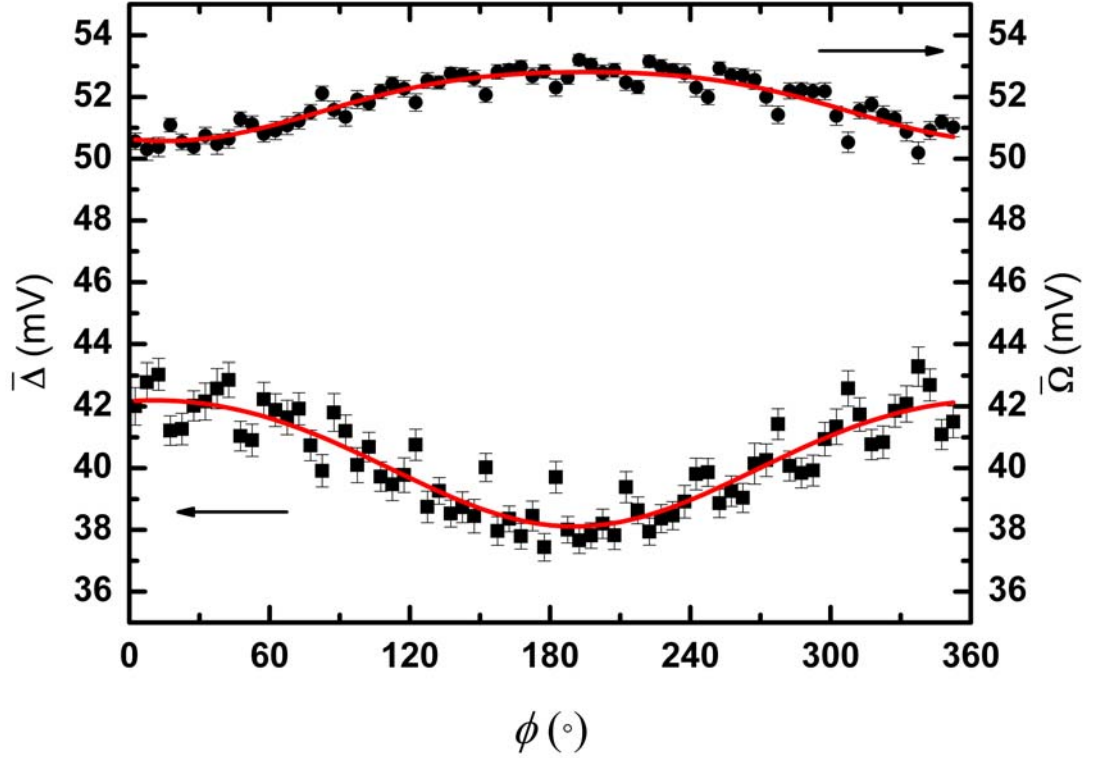


Figure 5-7 Supermodulation phase averaged local pairing gap and mode energy. The relations $\bar{\Delta}(\phi)$ and $\bar{\Omega}(\phi)$ are fitted by $\bar{\Delta}(\phi) = C_{\Delta} + A_{\Delta} \cos(\phi - \vartheta_{\Delta}) + B_{\Delta} \cos[2(\phi - \vartheta_{\Delta})]$ and $\bar{\Omega}(\phi) = C_{\Omega} + A_{\Omega} \cos(\phi - \vartheta_{\Omega}) + B_{\Omega} \cos[2(\phi - \vartheta_{\Omega})]$ and represented by the red fit lines. The modulation in mode energy is much weaker than that in local pairing gap. Dataset is 60614, OD89K.

Figure 5-7 says that within a unit cell, the lattice vibration mode energy Ω is modulated by periodic change in the unit cell dimension, but almost 180° out of phase with the modulation in Δ . In Chapter 4, the biggest change in inter-atomic distance within a unit cell due to supermodulation is the bond length d_A , the Cu-O_{apical} distance.

The mode energy Ω is smaller in supermodulation maxima (with $\phi \approx 0^\circ$ and minimal d_A) and larger in supermodulation minima (with $\phi \approx 180^\circ$ and maximal d_A). It is logical to postulate, from a purely mechanical model, that the frequency of a local lattice vibrational mode will be changed if the unit cell is distorted. Therefore, the modulation in Ω as the CuO_5 pyramid is periodically distorted could be the natural consequence if the boson mode detected in d^2I/dV^2 is local lattice vibration. The variation in Ω as function of ϕ is considerably weaker than that of Δ . For example, the fitted $\bar{\Delta}(\phi)$ and $\bar{\Omega}(\phi)$ from dataset 60614 are

$$\begin{aligned}\bar{\Delta}(\phi) &= 40.3 + 2.04 \cos(\phi - 10.5) - 0.12 \cos[2(\phi - 10.5)] \\ \bar{\Omega}(\phi) &= 51.9 - 1.12 \cos(\phi - 15.3) - 0.16 \cos[2(\phi - 15.3)]\end{aligned}\tag{5-6}$$

For the data obtained in the particular FOV presented in Figure 5-6, the percentage change (peak to peak amplitude) in Δ is 10.2% calculated from first harmonic amplitude, and the percentage change in Ω is 4.4%.

Although weak, the modulation in Ω with the wavevector \mathbf{q}_{SM} is universal across different dopings. Figure 5-8 shows examples of supermodulation phase averaged Δ and Ω at different dopings. The red fit line is the result of using first and second harmonics. As expected from the previous study [100], while the average gap value changes from $\sim 40\text{mV}$ to $\sim 50\text{mV}$, the average mode energy remains $52 \pm 1\text{mV}$. Weak modulation in Ω can be seen by eyes.

Table 5-1 lists the fitting parameters for $\bar{\Omega}(\phi)$. Of the importance is the modulation amplitude and the shift in phase from a perfect co-sinusoidal relation with the extrema at $\phi = 0^\circ$ or $\phi = 180^\circ$.

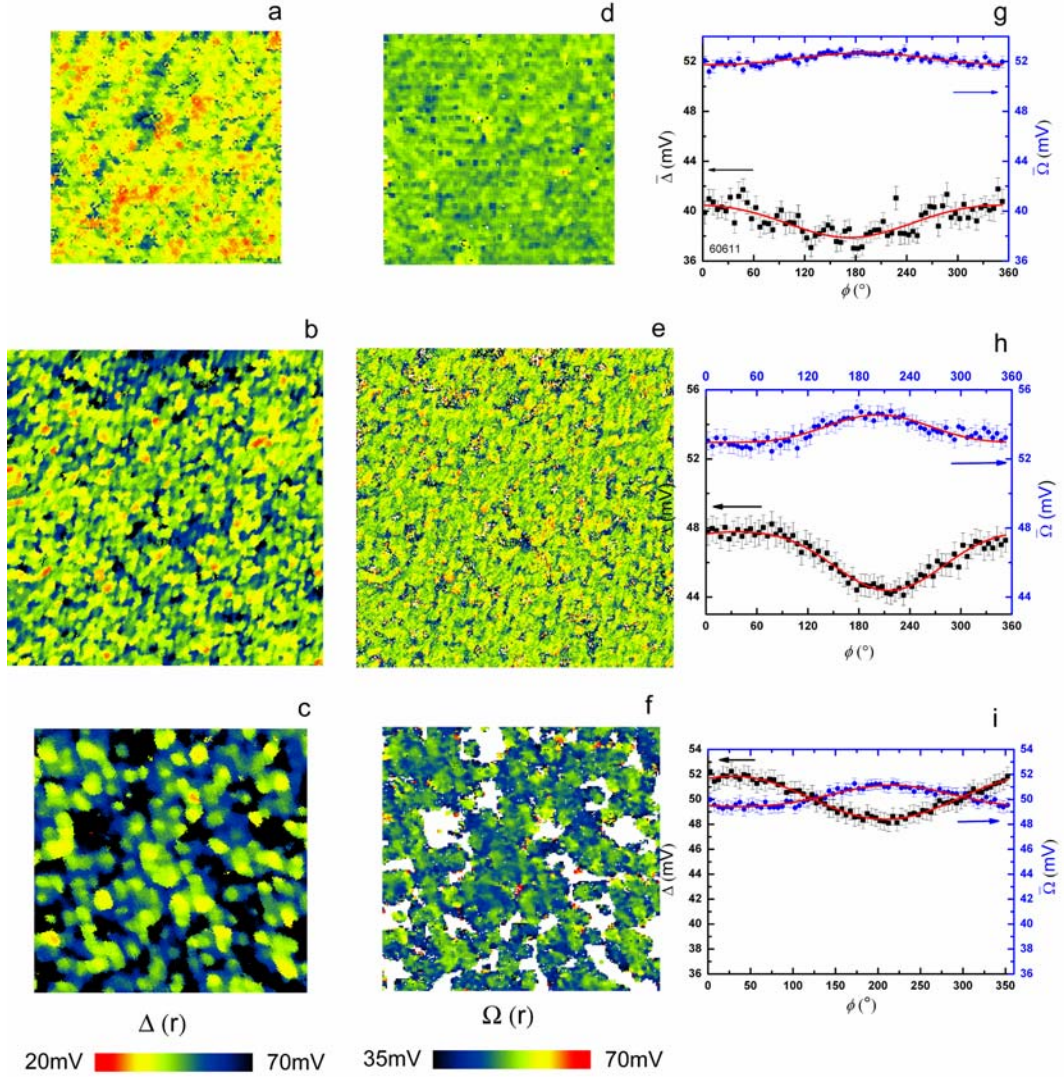


Figure 5-8 Gap and mode energy modulation as function of periodic unit cell distortion. (a), (b) and (c): Gap maps for $p \sim 0.18, 0.12(?), 0.10$. (d), (e) and (f): Mode energy maps of the three dopings. (h), (i) and (j): fitted $\bar{\Delta}$ and $\bar{\Omega}$ as function of supermodulation phase ϕ . The white black region in (c) and white region in (f) are the places where gap and the peak in d^2I/dV^2 is not well defined. Mode energy varies with the same periodicity, but 180° out of phase with gap as function of ϕ . The datasets are from: 60611 ($p \sim 0.18$), 41228 ($p \sim 0.12?$) and 40704 ($p \sim 0.10$).

Table 5-1 Fitting parameters for $\overline{\Omega}(\phi)$. The equation used to fit is $\overline{\Omega}(\phi) = C + A\cos(\phi - \vartheta) + B\cos[2(\phi - \vartheta)]$. $Amp./\overline{\Omega}$ is the relative peak-peak amplitude of the Ω modulation.

Dataset	Doping	T_c	A	B	C	ϑ	$\overline{\Omega}$	$Amp./\overline{\Omega}$
40504	?	OD65K	0.28	-0.13	50.7	18.6	50.5	2.2%
40704	0.10	UD64K	-0.85	0.09	50.2	35.9	50.2	6.4%
41228	0.12?	UD74K	-0.80	0.16	53.6	22.6	53.6	5.9%
51219 (^{18}O)	0.18	OD88K	-0.54	0.39	47.4	-28.8	46.4	3.0%
51225 (^{18}O)	0.18	OD88K	-0.18	-0.02	48.6	31.4	48.6	1.4%
60603	0.18	OD89K	-0.56	-0.04	52.1	-11.2	52.1	4.2%
60611	0.18	OD89K	-0.47	0.03	52.2	9.31	52.2	3.6%
60614	0.18	OD89K	1.20	-0.26	52.0	-19.6	54.13	6.3%

Mode energy modulates $4\% \pm 2\%$, only about half of the $9\% \pm 1\%$ in gap as reported in [99]. The modulation amplitude does not show noticeable doping dependence and can vary at different regions on the same sample too, as one can expect for a lattice vibration mode. We can also see that the phase shift is quite random, hard to draw quantitative conclusion.

5.5 Oxygen Isotope Effect on $\overline{\Delta}(\phi)$ and $\overline{\Omega}(\phi)$

Having established from last session that both superconducting gap and mode energy vary within individual unit cell (but with opposite direction), the next logical step is to examine the effect of isotope effect on their relation. Since if electron-lattice

interaction is the ‘pairing glue’, then one would expect to observe change in the Δ - ϕ relation within a CuO_5 pyramid.

The central result of this section is presented in Figure 5-9.

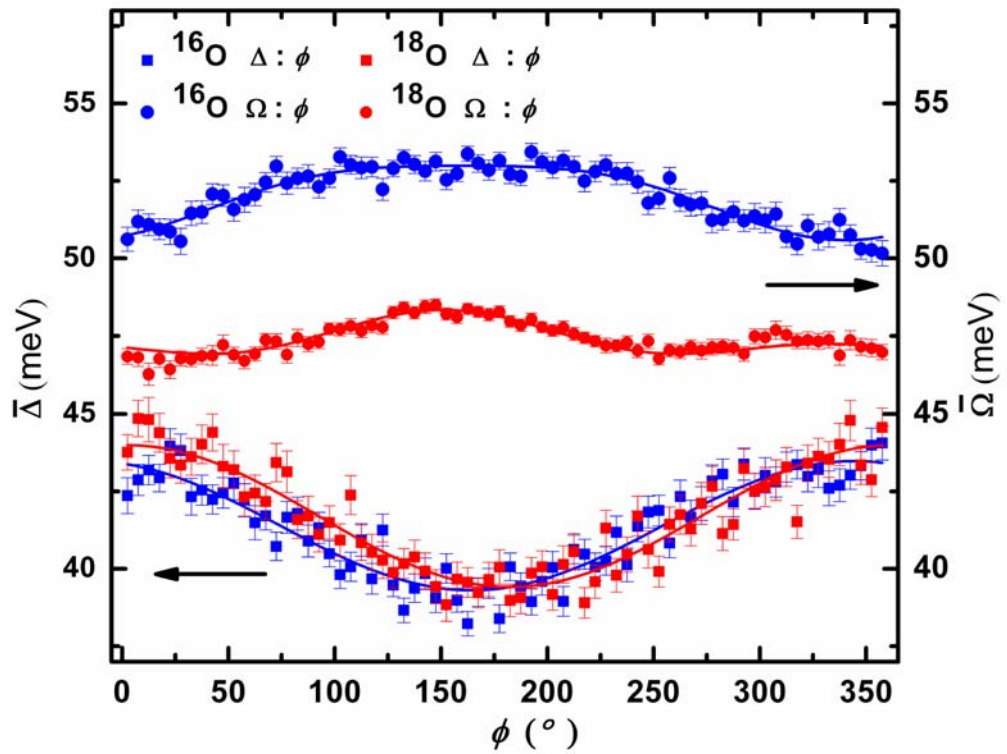


Figure 5-9 Oxygen isotope effect on $\bar{\Delta}(\phi)$ and $\bar{\Omega}(\phi)$. Blue: ^{16}O , Red: ^{18}O . With oxygen isotope substitution, the co-sinusoidal variation of gap as function of ϕ remains unchanged, except for some slight shift in phase. However, the relation $\bar{\Omega}(\phi)$ is shifted systematically by about -4meV from ^{16}O to ^{18}O , consistent with the shift reported in [100].

The significance of this result is that it presents a systematic approach to study the local relation among the critical ingredients: unit cell distortion, pairing gap and boson

mode, rather than depending on the random statistics on each quantity. One immediate deduction is that this graph does not indicate the evidence for a *local version* of BCS type theory where the electron-lattice interaction is the ‘pairing glue’. In a simple BCS type theory, the pairing gap is proportional to the lattice vibration mode energy:

$$\Delta \propto \omega_c e^{-1/N(0)g} \quad (5-1)$$

Assume coupling strength g is not changed by isotope substitution, when the characteristic frequency of mediating lattice vibration mode is changed, the gap will be changed by the same fraction. However, the local gap value in each unit cell is not altered by change of mode energy. There is a possible way to reconcile the paradox within BCS framework, which is through some Eliashberg type strong coupling model. This point will be discussed at the end of this chapter.

5.6 Oxygen isotope Effect on Bogoliubov Quasiparticle Excitation

As introduced in Chapter 2, quasiparticle interference (QPI) provides information about Bogoliubov excitation in superconducting states in cuprates [38]. It is therefore important to examine whether there is change of QPI. This process requires high precision determination of Bogoliubov band minima $\mathbf{k}_B(E) = [k_x(E), k_y(E)]$ where the quasiparticle excitation defined by $\mathbf{k} = (k_x, k_y)$ has minimal energy E . Also since only the quasiparticle state of a d -wave superconductor can have internally consistent interference wavevectors with the octet model [42], we can also determine the anisotropic gap function $\Delta(\mathbf{k})$.

Here a recent approach, ratio map, to determine \mathbf{k}_B developed by Hanaguri *et al.* [115] will be used.

In cuprate, the conductance is determined by

$$g(\mathbf{r}, E) = Ce^{-z/z_0} eN(\mathbf{r}, E) \quad (5-2)$$

Where $N(\mathbf{r}, E)$ is LDOS, the pre-factor is the distance dependent tunneling matrix element. In the real spectroscopic measurement, when taking spectrum at a point, the tip-surface distance z is determined by

$$\mathbf{I}_s = \int_0^{V_s} Ce^{-z/z_0} eN(\mathbf{r}, E = eV) dV \quad (5-3)$$

Where \mathbf{I}_s is the set current and V_s is the set bias voltage. Therefore, the pre-factor

$$Ce^{-z/z_0} = \frac{\mathbf{I}_s}{e \int_0^{V_s} N(\mathbf{r}, E = eV) dV} \quad (5-4)$$

The measured conductance is therefore

$$g(\mathbf{r}, E = eV) = \frac{\mathbf{I}_s N(\mathbf{r}, E = eV)}{\int_0^{V_s} N(\mathbf{r}, E = eV) dV} \quad (5-5)$$

In near optimally doped cuprate, the denominator $\int_0^{V_s} N(\mathbf{r}, E = eV) dV$ does not have strong spatial dependence, hence $g(\mathbf{r}, E) \propto LDOS$. However, with diminished doping $p > 0$, large spatial fluctuations in electronic structure [115,116] occur and the $g(\mathbf{r}, E) \propto LDOS$ does not hold. However, if we take ratio between positive and negative bias, the spatially inhomogeneous part is cancelled out.

$$Z(\mathbf{r}, E = eV) = \frac{g(\mathbf{r}, +V)}{g(\mathbf{r}, -V)} \quad (5-6)$$

Such ratio will not cancel the QPI modulation, as it might appear to. As Balatsky [117] points out, this ratio is equal to the ratio of coherence factor,

$$Z(\mathbf{r}, V) = \frac{|u(\mathbf{r}, eV)|^2}{|v(\mathbf{r}, eV)|^2} \quad (5-7)$$

where the normalization condition $|u(\mathbf{r}, eV)|^2 + |v(\mathbf{r}, eV)|^2 = 1$ ensures constructive spatial interference. Although this procedure is not required for near optimal doping, it is nevertheless helpful to use the same convention as in [118].

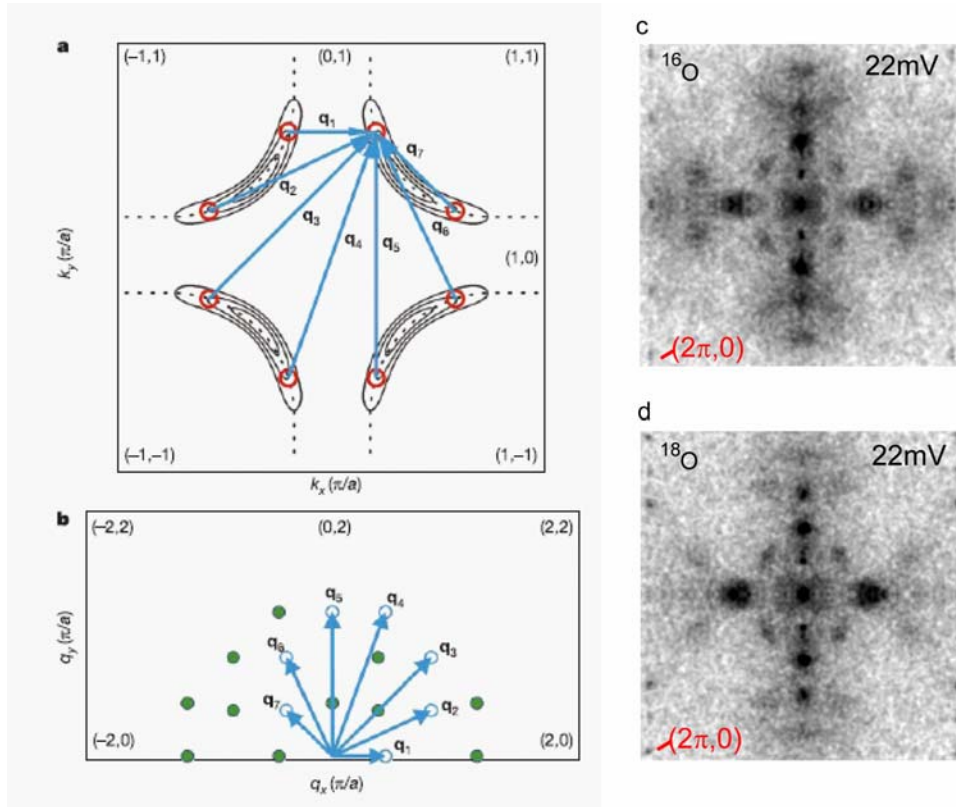


Figure 5-10 QPI of ^{16}O and ^{18}O optimal doped Bi-2212. (a)-(b): Illustration of octet model. (c)-(d) Fourier transformed ratio map $Z(\mathbf{q}, V = 22\text{mV})$ for both isotope samples.

$$\begin{aligned}
q_1 &= (2k_x, 0) & q_4 &= (2k_x, 2k_y) \\
q_2 &= (k_x + k_y, k_y - k_x) & q_5 &= (0, 2k_y) \\
q_3 &= (k_x + k_y, k_y + k_x) & q_6 &= (k_x - k_y, k_y + k_x) \\
& & q_7 &= (k_x - k_y, k_y - k_x)
\end{aligned} \tag{5-8}$$

We can invert set of \mathbf{q} vectors to extract \mathbf{k}_B . The algorithm and part of the QPI extraction is done by Andy Schmidt. Figure 5-11 shows the extracted \mathbf{k} -vectors for ^{16}O and ^{18}O samples.

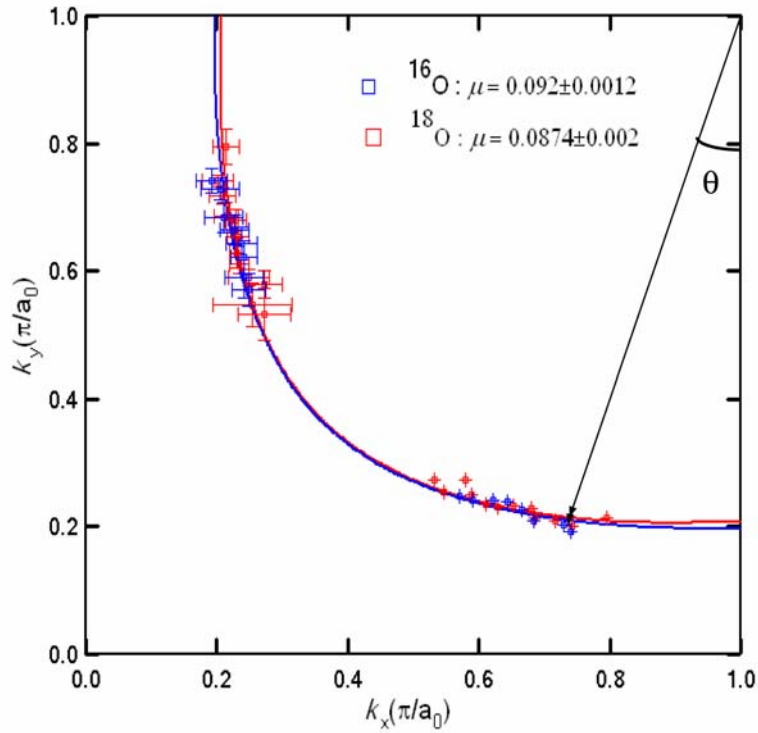


Figure 5-11 Bogoliubov band minima \mathbf{k}_B for ^{16}O and ^{18}O isotopes. The markers are the extracted \mathbf{k} -vectors. Blue: ^{16}O , red: ^{18}O . The solid curves are fitted normal state Fermi surface, using parameters from [119]. The \mathbf{k} -vectors extracted from $^{16}\text{O}/^{18}\text{O}$ samples lie within the error bar. The fitted chemical potential is $\mu = 0.092 \pm 0.0012 \text{ eV}$ for ^{16}O and $\mu = 0.087 \pm 0.002 \text{ eV}$ for ^{18}O .

It should be emphasized that each point in \mathbf{k} -space is extracted from different bias voltage. The extracted \mathbf{k} -vector can be fitted by the normal state band structure [119]

$$\begin{aligned} \varepsilon_k = & \mu + t_1 \frac{\cos k_x + \cos k_y}{2} + t_2 \cos k_x \cos k_y \\ & + t_3 \frac{\cos 2k_x + \cos 2k_y}{2} + t_4 \frac{\cos 2k_x \cos k_y + \cos k_x \cos 2k_y}{2} + t_4 \cos 2k_x \cos 2k_y \end{aligned} \quad (5-9)$$

The parameters used are $t_i = \{-0.5908, 0.0962, -0.1306, -0.0507, 0.0939\}$

Through fitting the QPI data, we can extract chemical potential for different dopings. Figure 5-12 shows the fitted band structure for different doping and the chemical potential extracted for each doping level.

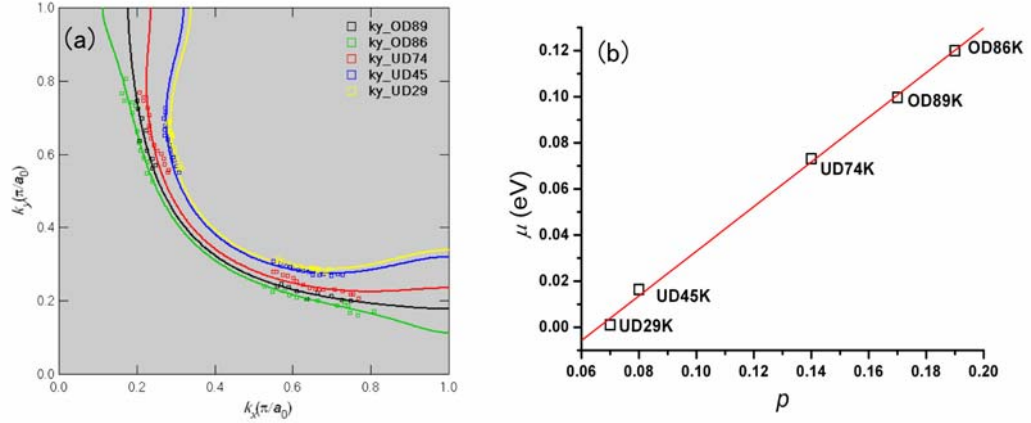


Figure 5-12 Doping dependence of chemical potential. (a) Fitted band structure from \mathbf{k}_B extracted from $p \sim 0.19, 0.17, 0.14, 0.08, 0.07$ using parameters in [119]. (b) Plot of μ vs. doping level. The slope is ~ 0.968 eV per doped hole.

Table 5-2 Doping dependence of chemical potential.

p	0.07	0.08	0.14	0.17	0.19
μ (eV)	0.00103	0.0164	0.0731	0.0997	0.120

From the fitting, μ changes by about 9.7meV per 1% change in hole density. That is, for the difference in fitted μ for $^{16}\text{O}/^{18}\text{O}$ isotope of 5meV, the possible doping level change by isotope substitution is $<0.5\%$. This small change again proves it is legitimate to state that we are indeed comparing isotope samples at the identical doping level.

Figure 5-13 shows the anisotropic gap function $\Delta(\theta_k)$ extracted from QPI.

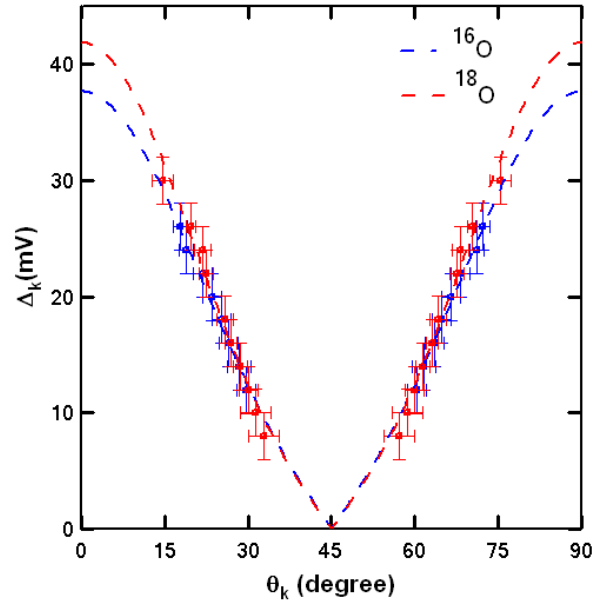


Figure 5-13 Gap function for ^{16}O and ^{18}O isotope samples. Scattered plot is the extracted gap vs. angle. θ_k is the angle defined in Figure 5-10, Δ_k is the bias voltage corresponding to each extracted \mathbf{k} -vector with angle θ_k . Again, the $\Delta(\theta_k)$ relation for $^{16}\text{O}/^{18}\text{O}$ isotope samples lie within the error bar. The dashed lines are the fitted gap function. The fitted parameters are $\Delta_0 = 37.67 \pm 2.9 \text{ meV} (^{16}\text{O})$ and $\Delta_0 = 41.89 \pm 2.5 \text{ meV} (^{18}\text{O})$, $B = 0.886 \pm 0.03 (^{16}\text{O})$ and $B = 0.865 \pm 0.02 (^{18}\text{O})$.

The functional form of gap equation is introduced by ARPES [120]:

$$\Delta(\theta_k) = \Delta_0 [B \cos(2\theta_k) + (1 - B) \cos(6\theta_k)] \quad (5-10)$$

where θ_k is the angle defined in Figure 5-10, Δ_k is the bias voltage corresponding to each extracted \mathbf{k} -vector with angle θ_k . Fitted Δ_0 and B are within the error bars for the two isotopes.

Finally, as a consistency check, plot $\mathbf{q}(E)$ for the two isotope samples, using the parameters obtained in above fitting schemes. The consistency plot is shown in Figure 5-14. The steps are as the following:

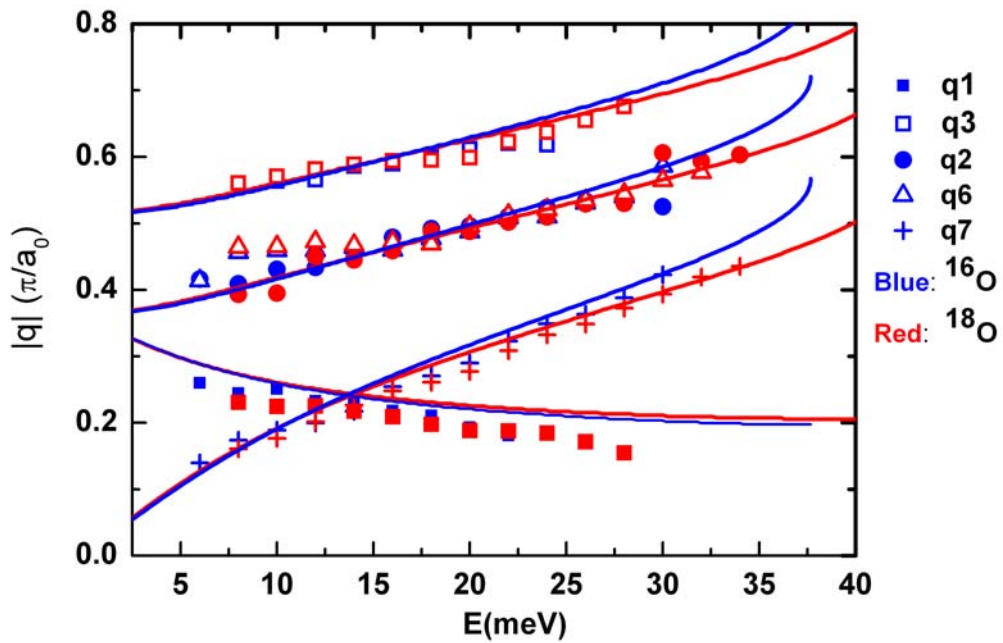


Figure 5-14 Self consistency check for QPI fitting. Scatter plot is the length of \mathbf{q} vectors extracted from $Z(\mathbf{q}, E)$ as function of the minimal excitation energy E . The solid lines are generated $\mathbf{q}(E)$ as described by the steps in the text.

- (1) Generate normal state band structure $E(\mathbf{k})$.
- (2) For each \mathbf{k} , calculate θ_k , then use this angle and Δ_0 obtained from fitting gap function (Figure 5-12) to determine the minimal excitation energy $E = \Delta(\theta_k)$ for the wavevector \mathbf{k} .

- (3) For each \mathbf{k} at the energy determined in (2), calculate the elastic scattering wavevector $\mathbf{q}(E) = \mathbf{k}(E) - \mathbf{k}'(E)$. (There are 7 other wavevectors \mathbf{k}' at the same energy E)

The $\mathbf{q}(E)$ for ^{16}O and ^{18}O also match well with each other. To summarize, there is no detectable change in Bogoliubove excitation in superconducting state upon oxygen isotope substitution at optimal doping.

5.7 Examine Spectral function $A(\mathbf{k}, \omega)$ Upon Isotope Substitution

STM and ARPES are mutually supplementary probes, being powerful in probing the \mathbf{r} -space and \mathbf{k} -space electronic structure respectively. STM measures the current between the tip and sample at location \mathbf{r} and energy ω (relative to Fermi energy E_F), and the conductance $g(\mathbf{r}, \omega)$ is [39]

$$g(\mathbf{r}, \omega) = I_0 \left| M_{f,i}^{\mathbf{r}} \right|^2 R(\omega) A(\mathbf{r}, \omega) \quad (5-11)$$

Where $M_{f,i}^{\mathbf{r}}$ is tunneling matrix elements, $R(\omega)$ represents the finite energy resolution, $A(\mathbf{r}, \omega)$ is the single particle spectral function in real space (or LDOS). ARPES measures the photoelectron current $I(\hat{e}, \mathbf{k}, \omega)$ ejected from the surface by UV and X-ray photons and can be written as

$$I(\hat{e}, \mathbf{k}, \omega) = I_0 \left| M_{f,i}^{\hat{e}} \right|^2 f(\omega) A(\mathbf{k}, \omega) \quad (5-12)$$

Where $M_{f,i}^{\hat{e}}$ is the photoemission matrix element, $f(\omega)$ is Fermi function, and $A(\mathbf{k}, \omega)$ is \mathbf{k} -space single particle spectral function.

STM's weakness in revealing \mathbf{k} -space information in cuprate has partly been covered by QPI technique, which is a mix of \mathbf{k} -space and \mathbf{r} -space imaging process. Recently Dr. Fujita develops method to extract full \mathbf{k} -space spectral function $A(\mathbf{k}, \omega)$ from LDOS measured by STM, and from which one can extract important quantities such as QP scattering rate.

This procedure adopts a d -wave BCS type model but with life time broadening [121,122]. The LDOS measured in STM is imaginary part of single particle Green's function. The simplest way to write Green's function for an interacting system is

$$G(\mathbf{k}, \omega) = \frac{1}{\omega - \varepsilon_{\mathbf{k}} - \Sigma(\mathbf{k}, \omega)} \quad (5-13)$$

The tight-binding dispersion is defined as

$$\begin{aligned} \varepsilon_{\mathbf{k}} = & \mu + t_1 \frac{\cos k_x + \cos k_y}{2} + t_2 \cos k_x \cos k_y \\ & + t_3 \frac{\cos 2k_x + \cos 2k_y}{2} + t_4 \frac{\cos 2k_x \cos k_y + \cos k_x \cos 2k_y}{2} + t_4 \cos 2k_x \cos 2k_y \end{aligned}$$

with μ from fitting QPI, and t_1 - t_4 in [119].

The self energy contains the d -wave superconducting gap and the QP scattering can be written as [122]

$$\Sigma(\mathbf{k}, \omega) = -i\Gamma + \frac{\Delta^2(\mathbf{k})}{\omega + \varepsilon_{\mathbf{k}} + i\Gamma} \quad (5-14)$$

The gap function is as defined before

$$\Delta(\mathbf{k}) = \Delta_0[B \cos(2\theta_{\mathbf{k}}) + (1 - B)\cos(6\theta_{\mathbf{k}})] \quad (5-15)$$

The broadening Γ due to scattering can be written as

$$\Gamma = \Gamma_1 + \alpha\omega \quad (5-16)$$

The second linear term in ω represents inelastic scattering and is employed by Alldredge *et al.* [123] to successfully fit the differential conductance dI/dV over much of the doping range in Bi-2212.

The total spectral function can be written as the summation of coherence part and background which accounts for the asymmetry of dI/dV . For a certain gap maximum Δ_0 ,

$$A_{STM}(\mathbf{k}, \omega; \Delta_0) = -\text{Im}G(\mathbf{k}, \omega; \Delta_0) + b\omega \quad (5-17)$$

To obtain the parameters Γ_1 , b , α , B , one can fit LDOS with gap size Δ_0 by

$$N(\omega, \Delta_0) = \sum_{\mathbf{k}} A_{STM}(\mathbf{k}, \omega; \Delta_0) \quad (5-18)$$

The nonlinear fitting is done by minimizing χ^2 using standard Levenberg-Marquardt method. After fitting LDOS for each gap size (averaged over some range of Δ_0), the total spectral function can be obtained by

$$A_{STM}(\mathbf{k}, \omega) = \sum_{\Delta_0} P(\Delta_0) A_{STM}(\mathbf{k}, \omega; \Delta_0) \quad (5-19)$$

Where $P(\Delta_0)$ is the probability of having gap maxima Δ_0 . An alternative way is to fit the averaged spectra which have gap size within $\pm 2mV$ of mean gap $\bar{\Delta}_0$.

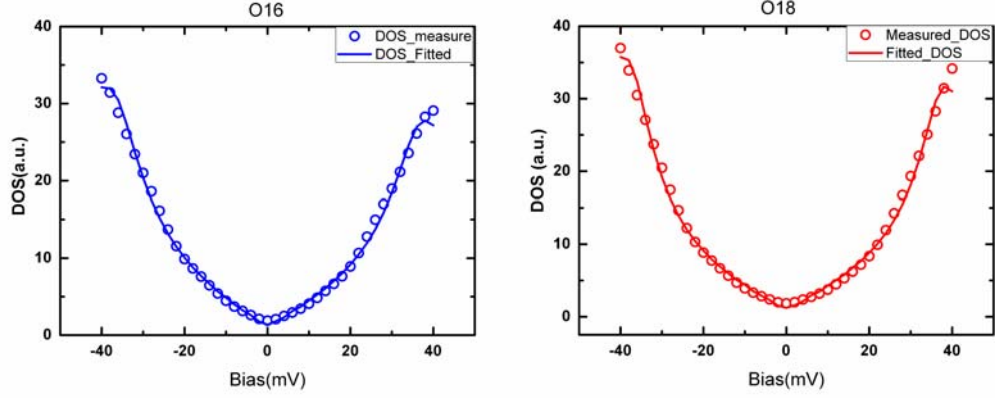


Figure 5-15 DOS fit by $A(\mathbf{k}, \omega)$. The fitting is done by using μ obtained by fitting \mathbf{k}_B and vary Δ_0 , B , Γ_1 , α and b .

The accuracy of fitting is calculated by χ^2 :

$$\chi^2 = \frac{1}{A} \frac{1}{N-p} \sum_i (y_{i,\text{exp}} - y_{i,\text{fit}})^2 \quad (5-20)$$

Where N is number of points, p is number of parameters, A is the total area under the fit curve. Table 5-3 summarizes the result.

Table 5-3 Fitting parameters for $A(\mathbf{k}, \omega)$.

	μ (eV)	Δ_0 (mV)	B	Γ_1 (mV)	α	b	χ^2
^{16}O	0.0921	36.8 ± 1.6	1.0	1.076 ± 0.6	0.1 ± 0.04	-0.804 ± 1	0.0006
^{18}O	0.0874	37.4 ± 1.5	1.0	0.95 ± 0.7	0.0792 ± 0.04	0.104 ± 1	0.0009

From fitting, the parameters for ^{16}O and ^{18}O all lie within error bar, no appreciable change is detected.

5.8 Discussions and conclusions

It is helpful to think the experimental results presented in Chapter 3, 4 and 5 as a whole. The large amount of information revealed by the series of experiments can be summarized as following:

- (1) There is ubiquitous electron-boson interaction feature outside the gap in tunneling spectra, with the mode energy Ω defined as the peak in d^2I/dV^2 after gap referencing $\omega=E-\Delta$.
- (2) Mode energy is strongly disordered at nanoscale, and average mode energy $\bar{\Omega}$ has minimal change with changing hole density.
- (3) There is intense modulation in d^2I/dV^2 along Cu-O bond direction with wavevector $\mathbf{p}_1 \approx 2\pi/a_0[\pm(0.2,0);\pm(0,0.2)] \pm 15\%$, or wavelength about $5a_0$.
- (4) Upon oxygen isotope substitution, the average mode energy $\bar{\Omega}$ has a shift of about -4.0meV from ^{16}O to ^{18}O .
- (5) Local disorder $\Delta(\mathbf{r})$ and $\Omega(\mathbf{r})$ are anti-correlated, with zero displacement correlation coefficient ~ -0.30 .
- (6) Pairing gap maxima varies co-sinusoidally with bulk supermodulation, or with Cu-O_{apical} distance d_A , with gap size anti-correlated with d_A .
- (7) Ω is also modulated with periodic unit cell distortion caused by bulk supermodulation, but roughly 180° out of phase with gap modulation, and the modulation amplitude is about half of that of pairing gap.
- (8) Isotope substitution does not change superconducting electronic structure.
- (9) $^{16}\text{O}/^{18}\text{O}$ oxygen isotope substitution systematically shifts the relation $\bar{\Omega}(\phi)$ but leaves $\bar{\Delta}(\phi)$ unchanged.

In the following subsections discussions will be made in the attempt to answer some of the questions arising from previous chapters.

5.8.1 Inelastic Stimulation of Apical Oxygen?

Pilgram, Rice and Sigrist [79] proposed a model where the dip-hump feature is caused by the stimulation of apical oxygen vibration mode by tunneling current, and hence irrelevant to CuO_2 plane electronic property. However, there are several important experimental facts which are not explained, at least, explicitly, by such model.

- (1) The dip-hump feature becomes more prominent with superconducting peak height, which reveals close link between this feature and CuO_2 electronic structure, if not directly to superconductivity. There is also another argument provided by Weiqiang Chen [124], the diminishing dip-hump feature as gap size increases and coherence peak broadens can also be explained by the suppression of quasiparticle weight due to inelastic scattering described by [123], and as a result the injected electrons coupled to the hypothetical inelastic oxygen mode quickly loses coherence, and produces less pronounced dip-hump feature.
- (2) Pilgram *et al.* [79] also proposed an inelastic tunneling path, which is through apical oxygen to in plane Cu. According to the simplified picture, there should be spatial modulation in d^2I/dV^2 at $\mathbf{p} \approx 2\pi/a_0[0.5,0]$ (wavelength $\sim 2a_0$) or no spatial modulation if the inelastic tunneling follows the path in Pilgram's model (see Figure 5-15 (a)). However, modulation at the observed wavevector $\mathbf{p}_1 \approx 2\pi/a_0[\pm(0.2,0);\pm(0,0.2)] \pm 15\%$ (\sim wavelength $5a_0$) is observed.
- (3) Another more general point is that, according to this line of reasoning, the inelastic tunneling experiments in break junction experiments over the past 50 years are all invalid. For example, in the famous SIN break junction experiment on superconducting Lead [51] which led to the quantitative confirmation of BCS

theory, the “kink” outside the superconducting gap can also be attributed to the inelastic stimulation of phonon in the barrier.

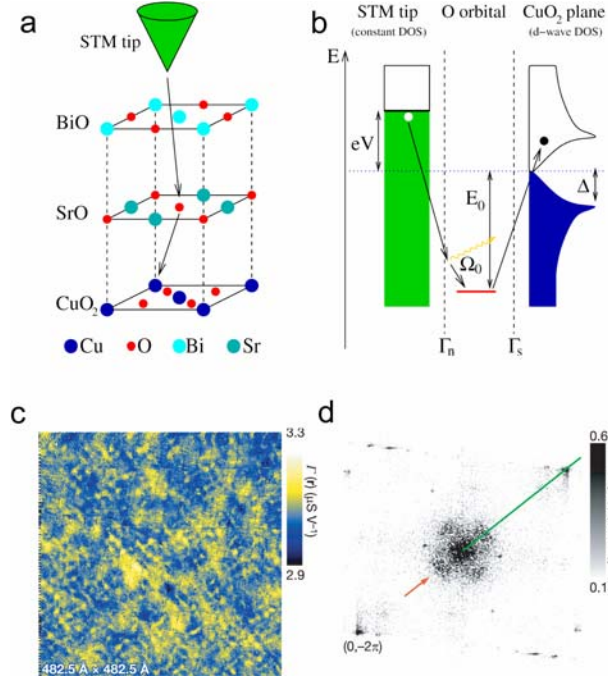


Figure 5-16 Hypothetical inelastic tunneling path and spatial modulation in d^2I/dV^2 . (a) The inelastic tunneling path for injected electrons proposed by Pilgram *et al.* [79]. The electron goes through apical oxygen but does not directly jump to the Cu below, instead, it is deflected to the neighboring Cu atom. (b) The schematics of inelastic tunneling picture. Injected electrons stimulate the vibrational mode with frequency Ω_0 in blocking SrO and BiO layers. (c) Spatial modulation in $d^2I/dV^2(\mathbf{r}, \omega)$. (d) Fourier transformed $d^2I/dV^2(\mathbf{r}, \omega)$ with $\mathbf{p}_1 \approx 2\pi/a_0[\pm(0.2, 0); \pm(0, 0.2)] \pm 15\%$. The model showing in (a) and (b) does not predict the spatial modulation shown by (c) and (d).

- (4) The energy of the boson mode is consistent with the range 50-80meV where the “kink” is detected in ARPES. Recently, ARPES also observed an isotope shift [125] of the kink energy at similar energy range and by similar amount of ~4meV as observed in STM. The consistency between ARPES and STM indicates that the observed boson mode is intrinsic to the material, since the mechanism for

tunneling and photoemission is totally different, one would not expect electron ejected by photons, which is at energy of $\sim eV$ will stimulate the same mode in the barrier in the similar way as tunneling electron of $\sim 100meV$ does.

From the above analysis, the inelastic stimulation picture does not really find experimental support, but rather a plausibility argument.

5.8.2 Electron-Lattice Interaction as Pairing Glue?

From discussion in 5.5 and Figure 5-9, the systematic shift of $\overline{\Omega}(\phi)$ upon oxygen isotope substitution while the unchanged relation $\overline{\Delta}(\phi)$, in the simplest way of thinking, does not indicate simple BCS type theory with electron-boson interaction as the pairing glue.

However, it should not be forgotten Cuprate cannot possibly be described by simple BCS interaction. A more realistic approach is to use Eliashberg like strong coupling framework. A. V. Balatsky [104] has worked out a local version of strong coupling theory, which can account for the anti-correlation between $\Delta(\mathbf{r})$ and $\Omega(\mathbf{r})$, the almost zero isotope shift in T_c in overdoped Bi-2212, and the isotope shifts in $\overline{\Omega}$. The key assumption in this model is that the local coupling constant $g(\mathbf{r})$ and mode energy $\Omega(\mathbf{r})$ are independent and randomly distributed. The effective coupling constant $g_{eff}(\mathbf{r})$ is found to be

$$g_{eff}(\mathbf{r}) = 2 \frac{g^2(\mathbf{r})}{\Omega(\mathbf{r})} \quad (5-21)$$

And the T_c (gap) is determined by the following BCS equation

$$T_c \propto \omega_c e^{-1/N(0)g_{eff}} \quad (5-22)$$

The only difference between this result and previously mentioned BCS equation is that besides the lattice vibration frequency ω_c , the effective coupling constant g_{eff} also varies with isotope substitution, such that the effects of ω_c and g_{eff} cancel each other to produce minimal change both in T_c and in $\bar{\Delta}$. The coupling strength should obviously be considered in any BCS type theory, but such cancellation is too much coincidence. To really address this problem, one would need to perform local version of McMillan-Rowell [126] inversion on 10^5 spectra to quantitatively determine $\alpha^2 F(\omega, \mathbf{k})$ (\mathbf{k} dependence is assumed for anisotropic coupling) and coupling strength $\lambda(\mathbf{k}) = \int \frac{\alpha^2 F(\omega, \mathbf{k})}{\omega} d\omega$. Also, the electron-electron interaction should be taken into account as in Eliashberg theory. Hence, although we cannot rule out the role of varying g_{eff} in causing minimal isotope shift in T_c (gap) and anti-correlation between Δ and Ω , up to this point there is no quantitative evidence from experiment this is the case.

Pasupathy *et al.* [127] studied the temperature dependence of pairing gap, the normal state electronic excitation and local coupling between electron and boson mode. In this study, the EBI strength λ is estimated by the deviation from the weak-coupling background beyond the superconducting pairing energy, which shows no correlation with pairing gap size. The normal state electronic structure (measured by dI/dV) is also found to be inhomogeneous, and there is strong correlation between pairing gap Δ and a hump feature around -150mV to -300mV in normal state. The conclusion is that the boson detected in STM is not likely to be the glue for high- T_c superconductivity, instead, the pairing inhomogeneity arises from electronic excitation which is observed in the normal state. Their reported non-correlation between the coupling strength and

the superconducting gap size is not consistent with our results, where we show the EBI feature obviously gets stronger as decreasing gap size (Figure 5-17). Also, Ref. [127] relies on a few point spectra to draw the conclusion and hence the statistics is not robust. Although we observed the correlation between EBI strength and gap size (peak height), the diminishing EBI feature as increasing gap size could be the result of losing quasiparticle weight (or coherence) due to scattering.

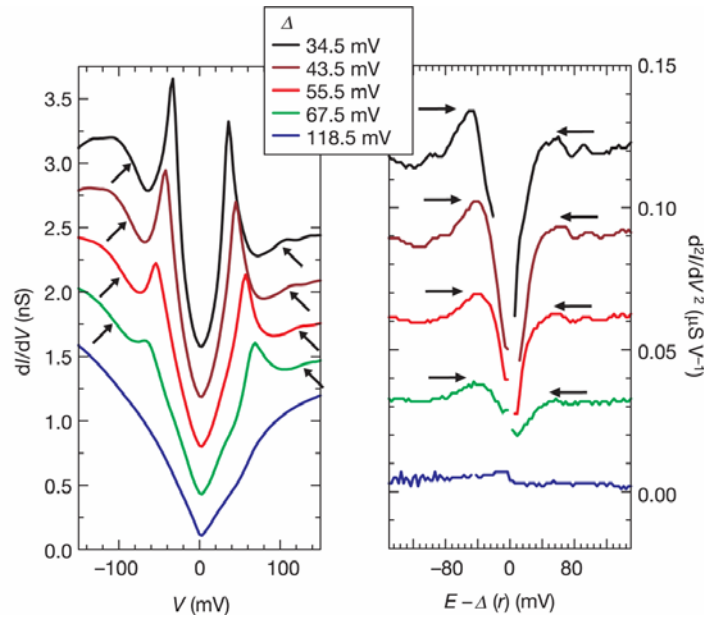


Figure 5-17 Examples of dI/dV and d^2I/dV^2 . The peak in d^2I/dV^2 diminishes as the coherence gap size increases and peak height decreases.

To summarize, the doping independence of $\bar{\Omega}$ (Figure 3-6) and isotope effect of $\bar{\Omega}(\phi)$ and $\bar{\Delta}(\phi)$ (Figure 5-9) do not indicate the electron-lattice interaction detected in STM is the pairing glue.

5.8.3 Anti-correlation Caused by Supermodulation?

Although the experimental results do not indicate the EBI observed in STM as pairing glue, the EBI does present a puzzling feature which suggests the lattice's relevance to

CuO₂ electronic structure. That is, the anti-correlation between $\Delta(\mathbf{r})$ and $\Omega(\mathbf{r})$. With the discovery that both Δ and Ω within a unit cell is modulated by bulk supermodulation, and their obvious local anti-correlation seen in Figure 5-9, the most direct deduction is that anti-correlation between Δ and Ω is through separate effects caused by distortion of unit cell. From a mechanical picture, it is very natural the lattice vibration frequency would be modified by change of unit cell dimension, for example, the change of hybridization due to change in inter-atomic distance will alter the effective spring constant and hence change the natural frequency. To test this postulate, the correlation between the two anti-correlations $C[\Delta(\mathbf{r}):\Omega(\mathbf{r})]$ and $C[\bar{\Delta}(\phi):\bar{\Omega}(\phi)]$ should be carefully examined.

Since the already weak modulation in $\bar{\Omega}(\phi)$ varies in amplitude from sample to sample, from FOV to FOV, we can check whether the correlation $C[\Delta(\mathbf{r}):\Omega(\mathbf{r})]$ grows with $\bar{\Omega}(\phi)$ amplitude. The amplitude $A[\bar{\Omega}(\phi)]$ is obtained from fit curves (See Figure 5-8 and Table 5-1).

Another more quantitative check is to calculate the normalized correlation from the fit curves of $\bar{\Omega}(\phi)$ by

$$C[\bar{\Delta}(\phi):\bar{\Omega}(\phi)] = \frac{\sum_i (\bar{\Delta}(\phi_i) - \Delta_0)(\bar{\Omega}(\phi_i) - \Omega_0)}{\sqrt{\sum_i (\bar{\Delta}(\phi_i) - \Delta_0)^2} \sqrt{\sum_i (\bar{\Omega}(\phi_i) - \Omega_0)^2}} \quad (5-23)$$

Where Δ_0 and Ω_0 are the spatial average, ϕ_i 's are the discretized phase with bin size 5°. Then plot $C[\Delta(\mathbf{r}):\Omega(\mathbf{r})]$ as function of $C[\bar{\Delta}(\phi):\bar{\Omega}(\phi)]$ for different datasets.

Figure 5-18 shows the relation $C[\Delta(\mathbf{r}):\Omega(\mathbf{r})]$ vs. $A[\bar{\Omega}(\phi)]$ and $C[\Delta(\mathbf{r}):\Omega(\mathbf{r})]$ vs. $C[\bar{\Delta}(\phi):\bar{\Omega}(\phi)]$.

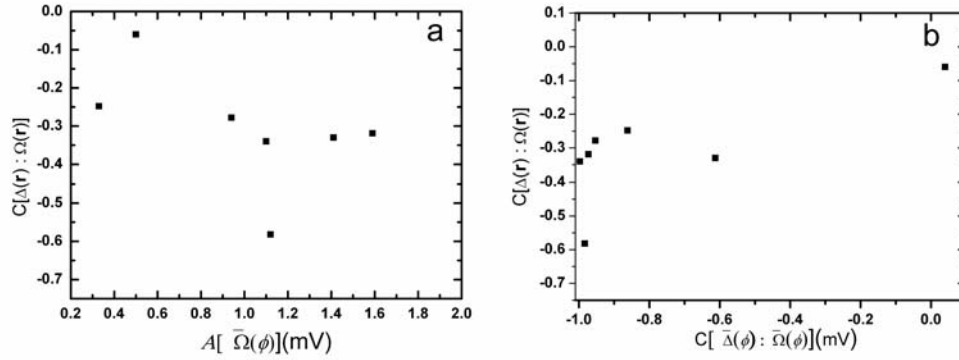


Figure 5-18 The spatial zero-displacement correlation coefficient as function of (a) modulation amplitude of Ω along supermodulation wavevector \mathbf{q}_{SM} , and (b) the correlation calculated from $\bar{\Delta}(\phi)$ and $\bar{\Omega}(\phi)$ defined by Equation (5-23). The data are taken from 40504, 41228, 51219, 51225, 60603, 60611, 60614.

The plots in Figure 5-18 are quite scattered. Without forcing a linear fit to run through the points, one can still see moderate dependence of $C[\Delta(\mathbf{r}) : \Omega(\mathbf{r})]$ on the supermodulation phase averaged Ω . The strength of anti-correlation $C[\Delta(\mathbf{r}) : \Omega(\mathbf{r})]$ increases with growing amplitude $A[\bar{\Omega}(\phi)]$ (Figure 5-18 (a)), and there is positive correlation between the two anti-correlations, $C[\Delta(\mathbf{r}) : \Omega(\mathbf{r})]$ and $C[\bar{\Delta}(\phi) : \bar{\Omega}(\phi)]$ (Figure 5-18 (b)). The above analysis cannot exclusively identify supermodulation as the only cause of the anti-correlation $C[\Delta(\mathbf{r}) : \Omega(\mathbf{r})]$ observed in [100], because (1) limited number of points do not give robust statistics, (2) a linear fit to the scatter plots would not be accurate, and hence hard to draw quantitative conclusion. Especially in Figure 5-18(b), if the anti-correlation $C[\Delta(\mathbf{r}) : \Omega(\mathbf{r})]$ is solely caused by supermodulation, then the points should align quite nicely along the line with slope 1.

Although not quantitatively precise, the puzzling anti-correlation $C[\Delta(\mathbf{r}) : \Omega(\mathbf{r})]$ seems to be closely linked with co-sinusoidal variation in Ω caused by bulk supermodulation.

There is a paradox though. In heavily overdoped Pb-Bi2212, bulk supermodulation is suppressed, but there is still anti-correlation between gap and mode energy about -0.3. This casts doubts on the solely supermodulation explanation.

5.8.4 Summary and Conclusions

The technical advancement is that for the first time, the isotope effects is measured for the same doping cuprates in both \mathbf{r} - and \mathbf{k} - space electronic structure at atomic scale; at the same time a deterministic relation between pairing strength and lattice vibration is established, such relation is a function of unit cell dimension change, and isotope effect on this relation is also measured as a function of individual unit cell distortion.

Oxygen isotope substitution at optimal doping in Bi-2212 does not change the average superconducting electronic structure, including Bogoliubov band minima \mathbf{k}_B , gap function, spectral function $A(\mathbf{k}, \omega)$. The average gap size $\bar{\Delta}$ and gap distribution do not change either. It is found that mode energy and pairing gap are both modulated by periodic unit cell distortion. Moreover, their respective modulations are almost 180° out of phase. The only detectable change by STM is the systematic shift of the relation $\bar{\Omega}(\phi)$.

Above results may at the first glance lead to the conclusion that electron-lattice is irrelevant in high- T_c superconductivity. However, such deduction is based on the simple minded assumption that electron-lattice and electron-electron (magnetic) interactions are mutually exclusive and either one of them is solely responsible for superconductivity in cuprates. In cuprates superconductor, superconducting transition temperature T_c and pairing strength Δ are not simply proportional to each other as in BCS theory, and are controlled by different mechanisms. T_c is determined by

superfluid density ρ_s [128] (see the Uemura plot in Figure 5-19), while pairing strength is affected by various factors such as dopant atoms, change of d_A , doping levels. Therefore, non-detectable change in average superconducting electronic structure by isotope substitution at optimal doping does not mean lattice is irrelevant in superconductivity, since ‘superconductivity’ in the context of cuprates can have multi-facet meaning.

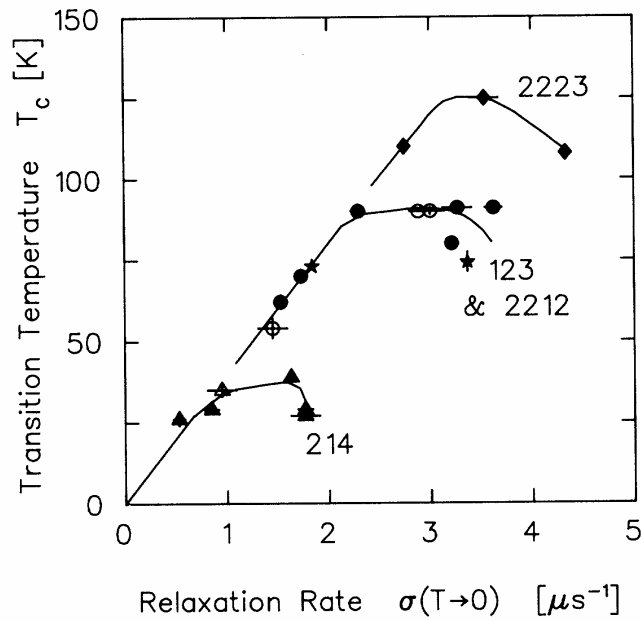


Figure 5-19 Universal relation between T_c and ρ_s taken from Ref. [128]. The muon-spin-relaxation rate σ is proportional to superfluid density ρ_s . 214 represents $La_{2-x}Sr_xCuO_4$, with doping $x=0.08, 0.10, 0.15, 0.20, 0.21$ in the order of increasing σ . 2212 represents $Bi_2Sr_2CaCu_2O_{8+\delta}$, 123 represents $YBa_2Cu_3O_y$, with increased doping as increasing σ . 2223 represents $Bi_{2-x}Pb_xSr_2Cu_3O_{10}$, $Tl_2Ba_2Ca_2Cu_3O_{10}$ and $(Tl_{0.5}Pb_{0.5})Sr_2Ca_2Cu_3O_9$, in the order of increasing doping. In the underdoped regime, T_c of different families falls onto a straight line as function of muon-spin-relaxation rate σ , or superfluid density ρ_s .

Another probably more profound point is that trying to separate the el-el and el-lattice interactions may from the beginning be the wrong approach. Trying to understand isotope effect from BCS framework is not a realistic approach, since in cuprates el-el

and el-lattice interactions are intermingled together. More importantly, in a system highly disordered at nanometer scale with strong electron correlation and evolved from AF Mott insulator, it is hard to imagine that BCS type theory will completely explain isotope effect. Moreover, the deterministic local relation between pairing gap Δ and mode energy Ω obviously requires a local theory.

As a matter of fact, some of the contemporary theory of correlated electron system does put el-el and el-lattice interaction on the equal foot and has local version of el-lattice interaction in the Hamiltonian. For example, Hubbard-Holstein (HH) model reads [129]

$$H = -t \sum_{\langle i,j \rangle \sigma} (c_{i\sigma}^+ c_{j\sigma} + c_{j\sigma}^+ c_{i\sigma}) + U \sum_i n_{i\uparrow} n_{i\downarrow} + \sum_i \frac{p_i^2}{2M} + \frac{1}{2} M \omega_0^2 x_i^2 + g n_i x_i \quad (5-24)$$

The first two terms are Hubbard interaction, the middle two terms are the energy of a local harmonic oscillator. The last term represents the on-site electron-phonon coupling due to local lattice distortion. In HH model, electron-phonon coupling and AF correlation strongly enhances both polaron formation and antiferromagnetism [130]. The simple physical picture is that (1) AF correlation reduces the mobility of holes and el-phonon coupling strength is inversely proportional to the kinetic energy of the holes, hence AF correlation will enhance polaron formation; (2) The el-phonon coupling enhances AF correlation by decreasing hole motions. In HH model, T_c is predicted to decrease as increasing el-phonon coupling constant λ , where λ is defined as $\lambda = 2g^2 / (2M\omega_0^2 W)$, the ratio of the single electron lattice deformation energy $E_p = g^2 / (2M\omega_0^2)$ to half of the electronic bandwidth $W/2 = 4t$. Also, the isotope shift in T_c as a function of doping is also predicted to be minimal around optimal doping and increases as going to lower doping (see Figure 5-20).

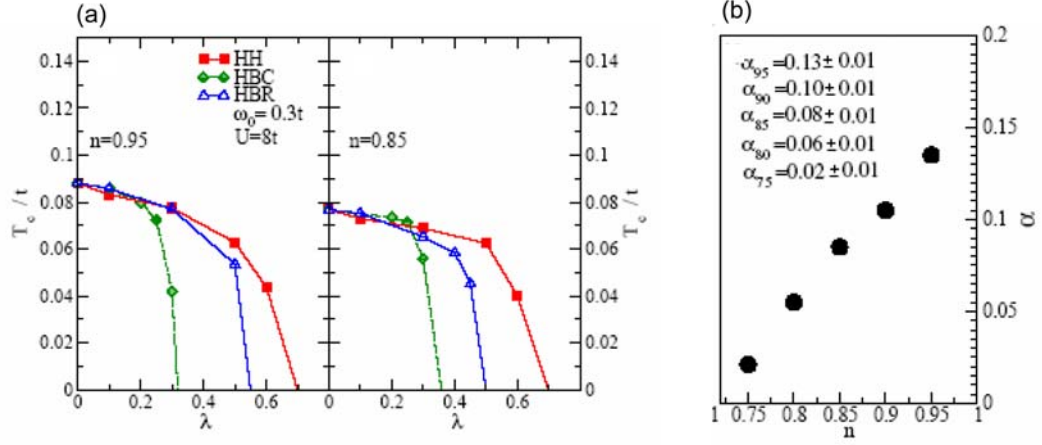


Figure 5-20 Prediction from Hubbard-Holstein model. (a) T_c vs. λ for Hubbard Holstein phonon (HH), Hubbard-buckling mode (BC) and Hubbard-breathing mode (HBR), with $\omega_0=0.3t$ and $U=8t$. Left panel is for 5% doping and the right panel is for 15% doping. Taken from Ref. [130] (b) Isotope coefficient α as a function of doping (note doping level= $1-n$). Taken from Ref. [129].

It should be kept in mind that there are well known experiments showing isotope effect on T_c is most prominent in underdoped region in some cuprate family, like in LSCO [131], and hence it will be important to study isotope effect on local electronic structure and electron-boson coupling in this doping range in Bi-2212 for future experiment.

APPENDIX A

Atomic Resolution d^2I/dV^2 -Imaging of $\text{Sr}_3\text{Ru}_2\text{O}_7$

The last one year of my Ph.D. was spent on studying a new type of strongly correlated electron system, $\text{Sr}_3\text{Ru}_2\text{O}_7$ (Sr327). In this appendix I will summarize the main experimental results from this study. This ongoing project is done with Dr. Jinho Lee and graduate student Milan Allan.

- **Crystal Structure**

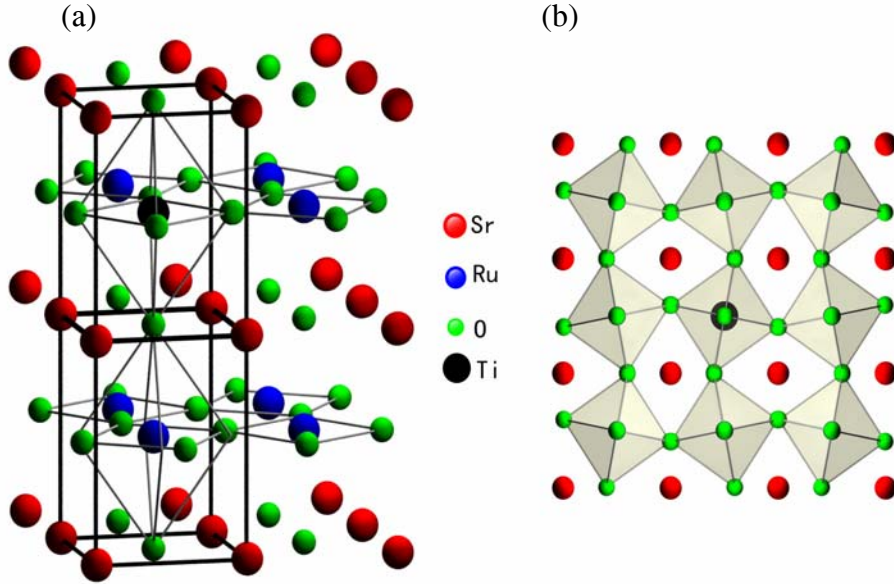


Figure App.-1 Crystal structure of $\text{Ti-Sr}_3\text{Ru}_2\text{O}_7$. (a) Side view (b) Top view. Note the rotation of RuO_6 octahedra along c -axis in (b). Ti impurity substitutes Ru atom.

$\text{Sr}_3\text{Ru}_2\text{O}_7$ has the similar layered perovskite structure as Bi-2212. Figure App.-1 shows the crystal structure. $\text{Sr}_3\text{Ru}_2\text{O}_7$ has the similar RuO_6 as in Bi-2212 with one apical oxygen sitting at the top apex. There is bulk structural $\sqrt{2} \times \sqrt{2}$ reconstruction, the RuO_6 octahedra rotates 7° about Ru-Ru bond direction. The material we studied is 1% Ti doped $\text{Sr}_3\text{Ru}_2\text{O}_7$, $\text{Sr}_3\text{Ru}_{1.98}\text{Ti}_{0.02}\text{O}_7$. Ru is in $4(d^4)^{4+}$ state with spin 1 and Ti is in $3(d^0)^{4+}$ state with spin 0.

- **Important Discoveries in $\text{Sr}_3\text{Ru}_2\text{O}_7$**

The two most distinguished property of pure $\text{Sr}_3\text{Ru}_2\text{O}_7$ are metamagnetism (MM) and nematicity.

The ground state of pure $\text{Sr}_3\text{Ru}_2\text{O}_7$ is paramagnetic close to ferromagnetic instability. When applying magnetic field, either along c -axis or parallel to ab plane at low temperature, the paramagnetic state rapidly changes to a more highly polarized state at high field. Such change is most obviously seen as the superlinear increase in magnetization when increasing magnetic field (see Figure App.-2(a)). The characteristic field of MM is about 5.5T when $B//ab$ and about 7.7 T when $B//c$. MM is also seen as peak in magnetoresistance as function of magnetic field (see figure App.-2(b)).

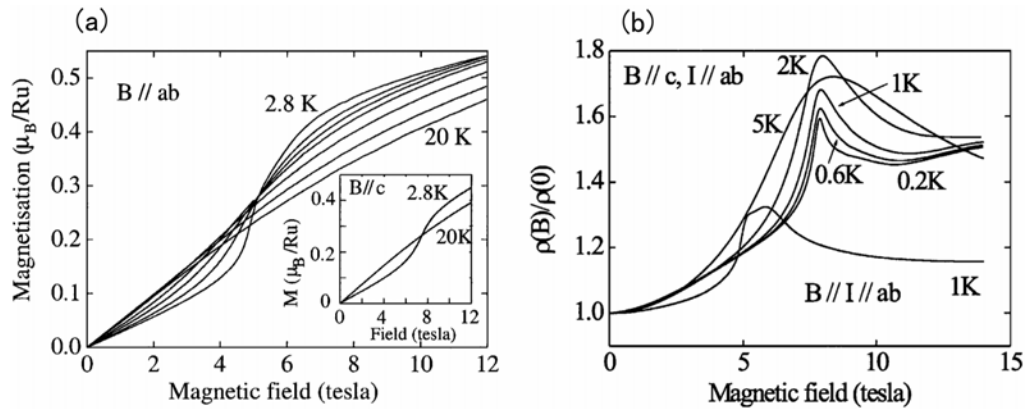


Figure App.-2 Metamagnetism in $\text{Sr}_3\text{Ru}_2\text{O}_7$. Taken from Ref. [132]. (a) Magnetization of single crystal $\text{Sr}_3\text{Ru}_2\text{O}_7$ for magnetic field applied in the ab plane. Metamagnetism is seen under 10K. (b) The magnetoresistance of single crystal $\text{Sr}_3\text{Ru}_2\text{O}_7$ at a series of temperatures under 10K. The peak corresponds to MM transition.

One very crude explanation for metamagnetism is through Stoner instability type argument, where the magnetic susceptibility diverges when the product of exchange U and density of states $N(E_F)$ is close to threshold.

$$\chi = \frac{\mu_0^2 N(E_F)}{1 - \frac{1}{2} U N(E_F)}$$

The other discovery is the electronic nematic fluid [133]. In high purity $\text{Sr}_3\text{Ru}_2\text{O}_7$, in proximity to metamagnetic quantum critical point, when applying modest in-plane magnetic field, strong anisotropy in magnetoresistance is developed. The easy and hard directions of magnetotransport are along *a*- or *b*-axis and can be interchanged by aligning the in-plane field along *b*- or *a*-axis (easy direction perpendicular to the in-plane magnetic field). Figure App.-3 shows the key result. This discovery shows an example of strongly-correlated nematic electron fluid characterized by a lowering of rotational symmetry in its itinerant property and is not a simple consequence of symmetry lowering of the lattice.

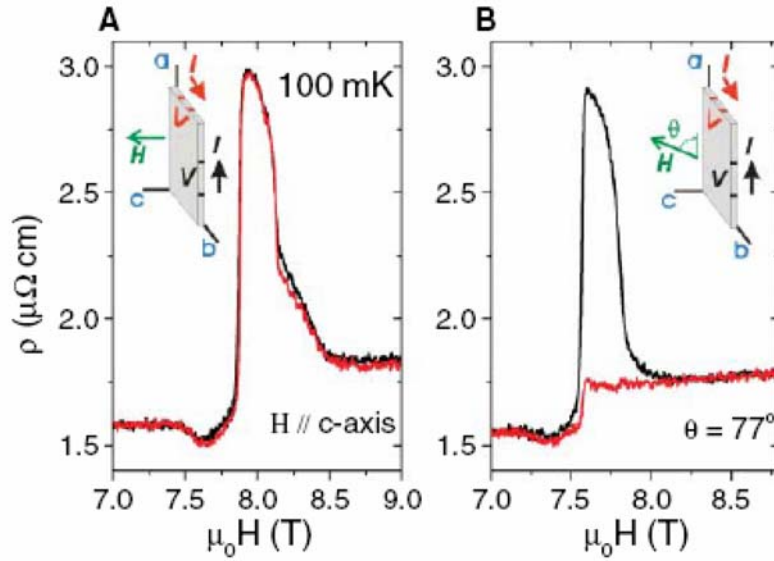


Figure App.-3 The two diagonal component ρ_{aa} and ρ_{bb} of in-plane magnetoresistivity of a high purity $\text{Sr}_3\text{Ru}_2\text{O}_7$. (A) Applied field is parallel to *c*-axis. (B) Applied field is tilted along *c*-axis and the in-plane component is along *a*-axis. ρ_{aa} (black) and ρ_{bb} (red). Taken from [133].

- **Atomic resolution d^2I/dV^2 -imaging on Sr327**

The material we mainly studied is 1% Ti doped sample $\text{Sr}_3\text{Ru}_{1.98}\text{Ti}_{0.02}\text{O}_7$. The reason to use Ti-Sr327 is that it is known that the above two distinctive properties of Sr327 only exists in high purity crystal. The superlinear rise of magnetization and metamagnetic peak in magnetoresistance shown in Figure App.-2(b) is smeared out with only 0.5% Ti impurity [134]. Therefore, it is important to understand what impurity is doing locally.

In this section I will briefly summarize the novel observation in d^2I/dV^2 study of Ti-Sr327.

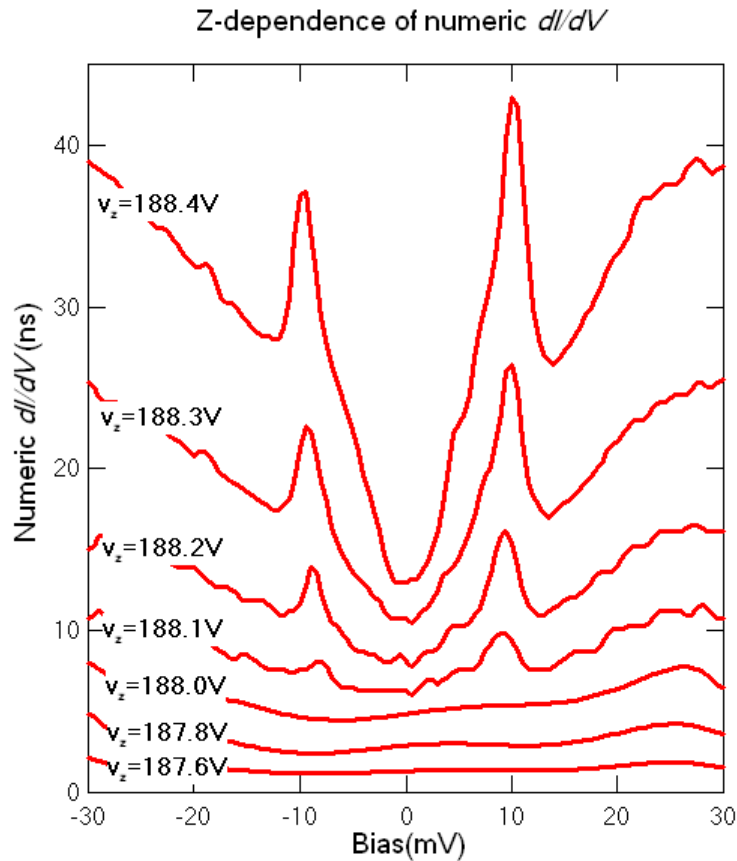


Figure App.-4 Distance dependence of differential conductance. V_z is z-piezo voltage. The larger V_z corresponds to smaller tip-surface distance d . As d is reduced, two symmetric peaks around $\pm 10\text{mV}$ emerge.

(1) Distance dependence of tunneling spectra

In Sr327, distance dependence of tunneling spectra is observed. When tip-surface distance gets smaller, symmetric peak emerges both at positive and negative bias. Figure App.-4 shows the situation.

There are several possibilities: (a) There is increased overlap of the wave functions between tip and either one or some of d_{xy} , d_{yz} , d_{xz} electronic orbitals of Ru atom. (b) Stark effect induced by increasing electric field due to decreased tip-surface distance. (c) The two symmetric peaks are from inelastic tunneling. The origin of such distance dependence phenomena is still under investigation.

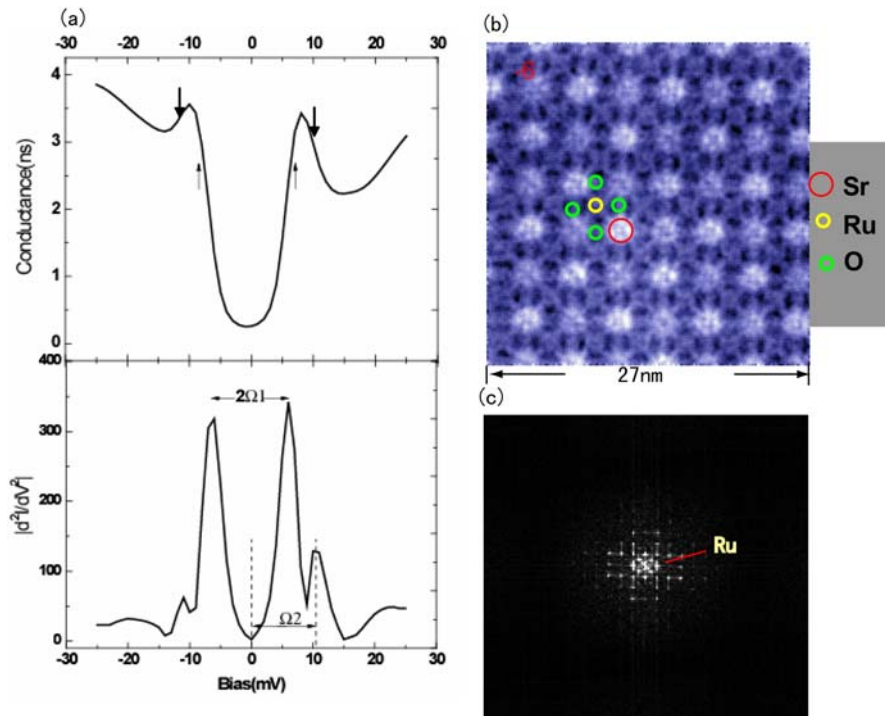


Figure App.-5 Fine structure inside unit cell. (a) Upper: numeric dI/dV , with the arrows pointing to the steepest rise in conductance. Lower: $|d^2I/dV^2|$. Define the energy of the peaks in second derivative as Ω_1 and Ω_2 (mode energy). (b) $dI/dV(\mathbf{r}, V=-6\text{mV})$. Sub-unit cell fine structure emerges with four-fold symmetry

within narrow energy range around Ω_1 and Ω_2 . (c) FFT of conductance map in (b). Fourier peaks outside the first First Brillouin zone defined by Ru peak are seen.

(2) Fine structure inside a unit cell

Around ± 4 -6mV, a 4-fold symmetric sub-unit cell pattern emerges in dI/dV -map. This sub-unit cell feature only appears within narrow energy range where peaks in d^2I/dV^2 occur and can be seen both in \mathbf{r} - and \mathbf{k} -space. Figure App.-5 shows the spatial modulation pattern. A distinctive feature is that those sub-unit cell features

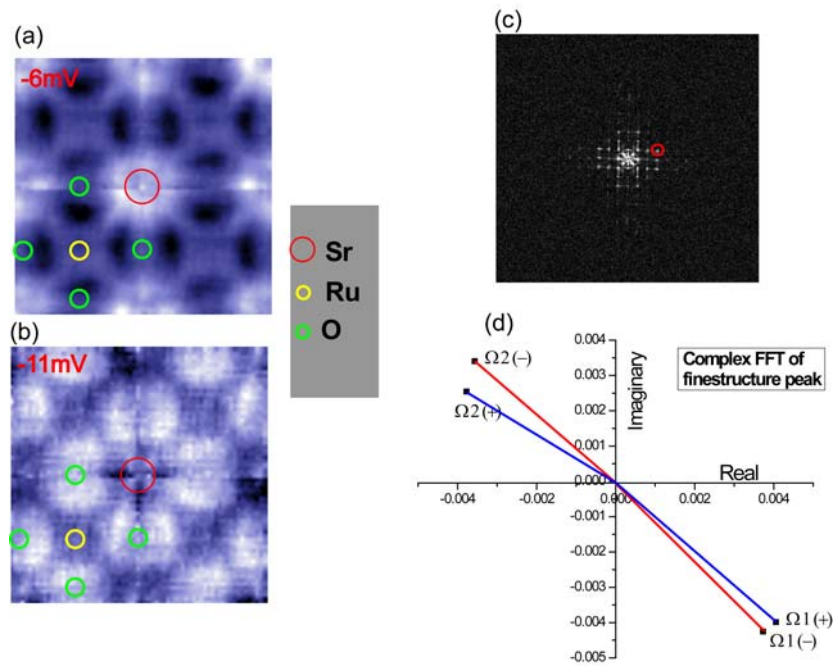


Figure App.-6 The spatial phase reversion of fine structure. Conductance map at energies around Ω_1 and Ω_2 . Equivalent unit cells are added together to increase S/N.

(a) $dI/dV(\mathbf{r}, V = -6\text{mV})$. (b) $dI/dV(\mathbf{r}, V = -11\text{mV})$. (c) FFT of fine structure at -6mV . The red circle marks one of the Fourier vectors corresponding to the fine structure. (d) The complex Fourier transform vector labeled by the red circle in (c) at different at the mode energies $\pm \Omega_1$ and $\pm \Omega_2$. It is clear that the fine structure is almost 180° out of phase at the two mode energies. And such spatial phase inversion is true for both filled states and empty states.

have four-fold symmetry and pointing along d_{xy} orbital direction. Taking into account the fact that those fine structures emerges with the rise of the symmetric peaks in dI/dV when the tip is pushed close to the surface, and occurs at the peak of d^2I/dV^2 , it is a logical hypothesis that the fine structures is related to d_{xy} orbital which is coupled to some collective mode and only detectable when the tip is close enough to the surface to have enough wave function overlap with the orbitals in RuO₂ layer. Note that Figure App.-5 only shows the fine structure at the energy around the primary peak in d^2I/dV^2 . At energy around the secondary peak position Ω_2 , similar sub-unit cell pattern also appears. Amazingly the spatial phase of the fine structure at Ω_1 and Ω_2 is reversed. See Figure App.-6.

(3) Ti impurity effect on mode energy

To map out the mode energy, we take the similar approach as in d^2I/dV^2 study in Bi-2212. A mode energy map can be generated by defining half of the energy difference between the two symmetric peaks in d^2I/dV^2 as mode energy value (note in this case we have two mode energies, Ω_1 and Ω_2 on each side).

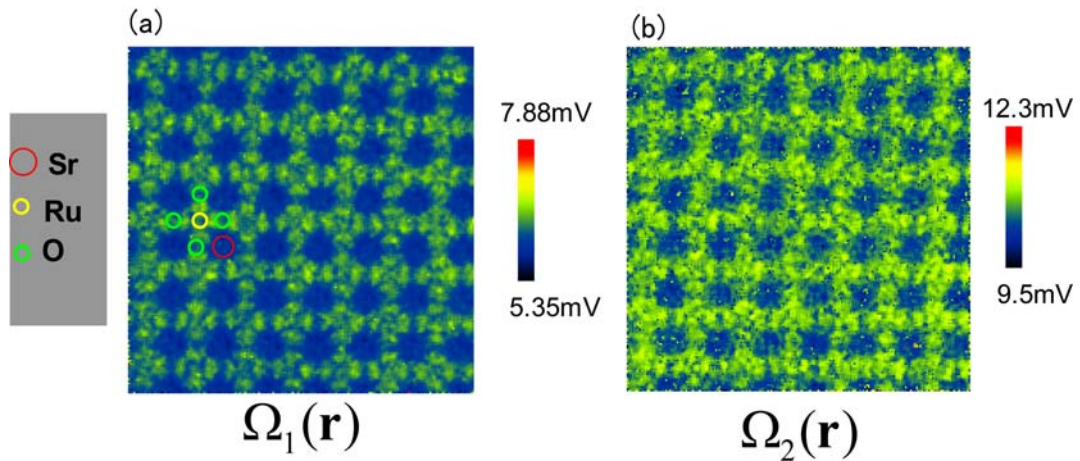


Figure App.-7 Mode energy map. Ω_1 and Ω_2 are defined in Figure App.-5. It is obvious that the mode energy also exhibits the fine structures similar as that in dI/dV map.

Ti impurity replaces Ru atom. With atomic resolution imaging, we can examine the local effect of Ti impurity. The primary effect of Ti impurity is to shift both Ω_1 and Ω_2 to higher energies. When moving away from Ti, the mode energy rapidly falls down to the average value within one unit cell. More over, mode energy at Ti site exhibits 4-fold symmetry. Figure App.-8 shows the mode energy map around a single Ti impurity and the angle averaged mode energy as function of distance to Ti site.

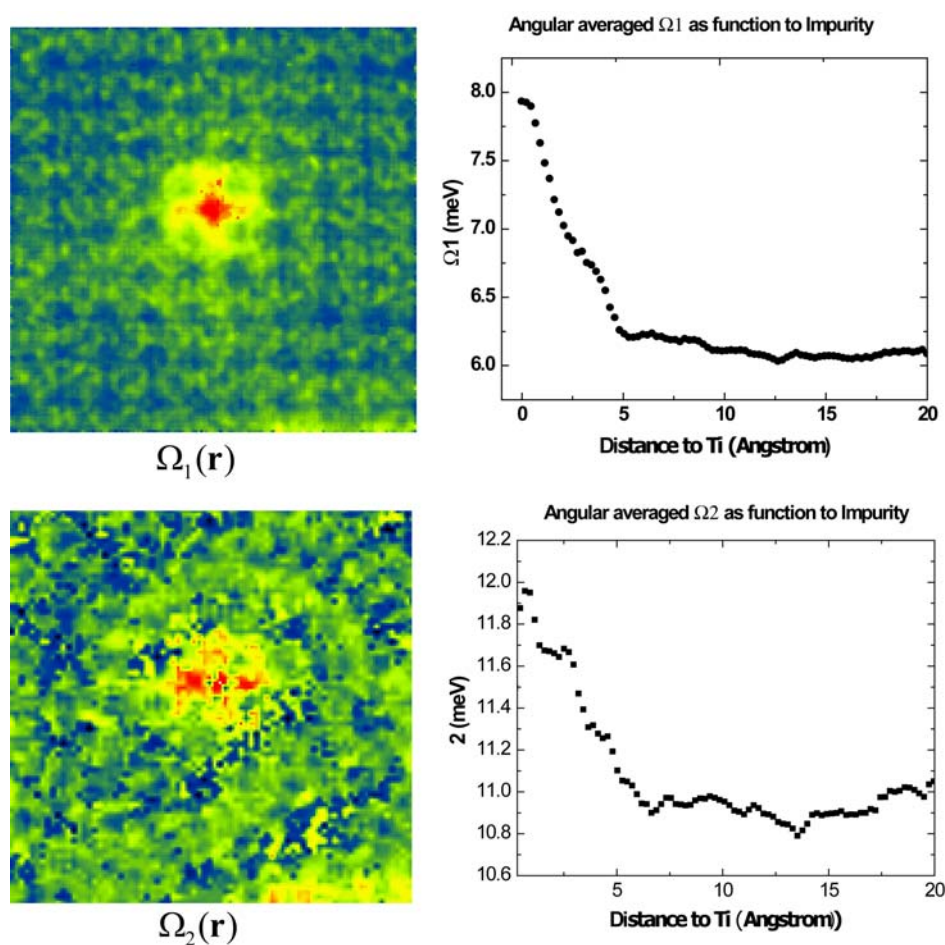


Figure App.-8 Distance dependence of mode energy around Ti impurity. The mode energy falls quickly to background value within a unit cell from Ti atom, and exhibits four-fold symmetry.

One hypothesis of such local effect on mode energy is that Ti distorted the local lattice since it has different radius as the neighboring Ru ions, therefore, frequency of the local mode energy, either lattice vibration or other local mode, is changed.

In summary, a primary study of Sr327 reveals distance dependent differential conductance, sub-unit cell fine structure and the local effect of Ti impurity on Sr327 electronic structure. All the three phenomena are closely connected, primarily because all the dramatic emergence of new patterns in dI/dV (distance dependence peak, fine structure) happens in a same and narrow energy range. More over, Ti impurity locally pushes the energy of the symmetric peaks in dI/dV by about 2mV (which is about 30%), indicative of the very local nature of the observed new phenomena in Sr327.

REFERENCES

1. G. Binnig and H. Rohrer, Scanning tunneling microscopy, *Helv. Phys. Acta.* **55**, 726 (1982).
2. G. Binnig, H. Rohrer, C. Gerber, and E. Weibel, Tunneling through a controllable vacuum gap, *Applied Physics Letters* **40**, 178 (1982).
3. G. Binnig, H. Rohrer, C. Gerber, and E. Weibel, Surface Studies by Scanning Tunneling Microscopy, *Phys. Rev. Lett.* **49**, 57 (1982).
4. J. Bardeen, Tunnelling from a Many-Particle Point of View, *Phys. Rev. Lett.* **6**, 57 (1961).
5. D.-J. Kim and J.-Y. Koo, A low-noise and wide-band ac boosting current-to-voltage amplifier for scanning tunneling microscopy, *Rev. Sci. Instr.* **76**, 023703 (2005).
6. J. E. Hoffman, Thesis, (2003).
7. H. K. Onnes, *Leiden Comm.* 120b, 122b, 124c, (1911).
8. W. Meissner and R. Ochsenfeld, *naturwissenschaften* **21**, 787 (1933).
9. J. Bardeen, L. N. Cooper, and J. R. Schrieffer, Theory of Superconductivity, *Phys. Rev.* **108**, 1175 (1957).
10. M. Tinkham, *Introduction to Superconductivity* (McGraw-Hill, New York, 1980), Chap. 2.
11. H. Frolich, Theory of the Superconducting State. I. The Ground State at the Absolute Zero of Temperature, *Phys. Rev.* **79**, 845 (1950).
12. E. Maxwell, Isotope Effect in the Superconductivity of Mercury, *Phys. Rev.* **78**, 477 (1950).
13. C. A. Reynolds, B. Serin, W. H. Wright, and L. B. Nesbitt, Superconductivity of Isotopes of Mercury, *Phys. Rev.* **78**, 487 (1950).
14. A. A. Abrikosov, *Zh. Eksperim. i Teor. Fiz.* **32**, 1442 (1957).
15. W. L. McMillan, Transition Temperature of Strong-Coupled Superconductors, *Phys. Rev.* **167**, 331 (1968).

16. J. G. Bednorz and K. A. Müller, Possible high T_c superconductivity in the Ba–La–Cu–O system, *Z. Phys. B* **64**, 189 (1986).
17. M. K. Wu, J. R. Ashburn, C. J. Torng, P. H. Hor, R. L. Meng, L. Gao, Z. J. Huang, Y. Q. Wang, and C. W. Chu, Superconductivity at 93 K in a new mixed-phase Yb-Ba-Cu-O compound system at ambient pressure, *Phys. Rev. Lett.* **58**, 908 (1987).
18. Y. Maeno, H. Hashimoto, K. Yoshida, S. Nishizaki, T. Fujita, J. G. Bednorz, and F. Lichtenberg, Superconductivity in a layered perovskite without copper, *Nature* **372**, 532 (1994).
19. Y. Kamihara, T. Watanabe, M. Hirano, and H. Hosono, Iron-Based Layered Superconductor $\text{La}[\text{O}_{1-x}\text{F}_x]\text{FeAs}$ ($x = 0.05\text{--}0.12$) with $T_c = 26$ K, *J. Am. Chem. Soc.* **130**, 3296 (2008).
20. G. F. Chen, T. Wu, G. Wu, R. H. Liu, H. Chen, and D. F. Fang, Superconductivity at 41 K and its competition with spin-density-wave instability in layered $\text{CeO}_{1-x}\text{F}_x\text{FeAs}$, Preprint at <http://arxiv.org/abs/0803.3790v1> (2008).
21. X. H. Chen, T. Wu, G. Wu, R. H. Liu, H. Chen, and D. F. Fang, Superconductivity at 43 K in Samarium-arsenide Oxides $\text{SmFeAsO}_{1-x}\text{F}_x$, *Cond. Mat. Preprint* at <http://arxiv.org/abs/0803.3603> (2008).
22. S. Maekawa, in *Physics of Transition Metal Oxides*, edited by S. Maekawa (Springer, Verlag Berlin Heidelberg New York, 2004), Chap. 1.
23. G. Kotliar and J. Liu, Superexchange mechanism and d-wave superconductivity, *Phys. Rev. B* **38**, 5142 (1988).
24. J. R. Kirtley, C. C. Tsuei, J. Z. Sun, C. C. Chi, L. S. Yu-Jahnes, A. Gupta, M. Rupp, and M. B. Ketchen, Symmetry of the order parameter in the high- T_c superconductor $\text{YBa}_2\text{Cu}_3\text{O}_{7-d}$, *Nature* **373**, 225 (1995).
25. C. C. Tsuei, J. R. Kirtley, M. Rupp, J. Z. Sun, A. Gupta, M. B. Ketchen, C. A. Wang, Z. F. Ren, J. H. Wang, and M. Bhushan, Pairing Symmetry in Single-Layer Tetragonal $\text{Tl}_2\text{Ba}_2\text{CuO}_{6+d}$ Superconductors, *Science* **271**, 329 (1996).
26. W. N. Hardy, D. A. Bonn, D. C. Morgan, R. Liang, and K. Zhang, Precision measurements of the temperature dependence of λ in $\text{YBa}_2\text{Cu}_3\text{O}_{6.95}$: Strong evidence for nodes in the gap function, *Phys. Rev. Lett.* **70**, 3999 (1993).

27. S. Kamal, D. A. Bonn, N. Goldenfeld, P. J. Hirschfeld, R. Liang, and W. N. Hardy, Penetration Depth Measurements of 3D XY Critical Behavior in $\text{YBa}_2\text{Cu}_3\text{O}_{6.95}$ Crystals, *Phys. Rev. Lett.* **73**, 1845 (1994).
28. Z. X. Shen *et al.*, Anomalous large gap anisotropy in the a-b plane of $\text{Bi}_2\text{Sr}_2\text{CaCu}_2\text{O}_{8+d}$, *Phys. Rev. Lett.* **70**, 1553 (1993).
29. P. L. Gammel, D. J. Bishop, G. J. Dolan, J. R. Kwo, C. A. Murray, L. F. Schneemeyer, and J. V. Waszczak, Observation of Hexagonally Correlated Flux Quanta In $\text{YBa}_2\text{Cu}_3\text{O}_7$, *Phys. Rev. Lett.* **59**, 2592 (1987).
30. C. E. Gough, M. S. Colclough, E. M. Forgan, R. G. Jordan, M. Keene, C. M. Muirhead, A. I. M. Rae, N. Thomas, J. S. Abell, and S. Sutton, Flux quantization in a high- T_c superconductor, *Nature* **326**, 855 (1987).
31. J. L. Tallon, C. Bernhard, H. Shaked, R. L. Hitterman, and J. D. Jorgensen, Generic superconducting phase behavior in high- T_c cuprates: T_c variation with hole concentration in $\text{YBa}_2\text{Cu}_3\text{O}_{7-d}$, *Phys. Rev. B* **51**, 12911 (1995).
32. B. Batlogg, H. Y. Hwang, H. Takagi, R. J. Cava, H. L. Kao, and J. Kwo, Normal state phase diagram of $(\text{La,Sr})_2\text{CuO}_4$ from charge and spin dynamics, *Physica C* **235-240**, 130 (1994).
33. I. G. Kuzemskaya, A. L. Kuzemsky, and A. A. Cheglov, Superconducting Properties of the Family of Mercurocuprates and Role of Layered Structure, *J. Low Temp. Phys.* **118**, 147 (2000).
34. J.-P. Locquet, J. Perret, J. Fompeyrine, E. Machler, J. W. Seo, and G. Van Tendeloo, Doubling the critical temperature of $\text{La}_{1.9}\text{Sr}_{0.1}\text{CuO}_4$ using epitaxial strain, *Nature* **394**, 453 (1998).
35. E. Pavarini, I. Dasgupta, T. Saha-Dasgupta, O. Jepsen, and O. K. Andersen, Band-Structure Trend in Hole-Doped Cuprates and Correlation with $T_{c,\text{max}}$, *Phys. Rev. Lett.* **87**, 047003 (2001).
36. H. Eisaki, N. Kaneko, D. L. Feng, A. Damascelli, P. K. Mang, K. M. Shen, Z. X. Shen, and M. Greven, Effect of chemical inhomogeneity in bismuth-based copper oxide superconductors, *Phys. Rev. B* **69**, 064512 (2004).
37. K. Fujita, T. Noda, K. M. Kojima, H. Eisaki, and S. Uchida, Effect of Disorder Outside the CuO_2 Planes on T_c of Copper Oxide Superconductors, *Phys. Rev. Lett.* **95**, 097006 (2005).

38. K. McElroy, R. W. Simmonds, J. E. Hoffman, D. H. Lee, J. Orenstein, H. Eisaki, S. Uchida, and J. C. Davis, Relating atomic-scale electronic phenomena to wave-like quasiparticle states in superconducting $\text{Bi}_2\text{Sr}_2\text{CaCu}_2\text{O}_{8+\delta}$, *Nature* **422**, 592 (2003).
39. K. McElroy, G. H. Gweon, S. Y. Zhou, J. Graf, S. Uchida, H. Eisaki, H. Takagi, T. Sasagawa, D. H. Lee, and A. Lanzara, Elastic Scattering Susceptibility of the High Temperature Superconductor $\text{Bi}_2\text{Sr}_2\text{CaCu}_2\text{O}_{8+d}$: A Comparison between Real and Momentum Space Photoemission Spectroscopies, *Phys. Rev. Lett.* **96**, 067005 (2006).
40. S. H. Pan *et al.*, Microscopic electronic inhomogeneity in the high-Tc superconductor $\text{Bi}_2\text{Sr}_2\text{CaCu}_2\text{O}_{8+x}$, *Nature* **413**, 282 (2001).
41. K. M. Lang, V. Madhavan, J. E. Hoffman, E. W. Hudson, H. Eisaki, S. Uchida, and J. C. Davis, Imaging the granular structure of high-Tc superconductivity in underdoped $\text{Bi}_2\text{Sr}_2\text{CaCu}_2\text{O}_{8+d}$, *Nature* **415**, 412 (2002).
42. Q.-H. Wang and D.-H. Lee, Quasiparticle scattering interference in high-temperature superconductors, *Phys. Rev. B* **67**, 020511 (2003).
43. H. L. Edwards, D. J. Derro, A. L. Barr, J. T. Markert, and A. L. de Lozanne, Spatially Varying Energy Gap in the CuO Chains of $\text{YBa}_2\text{Cu}_3\text{O}_{7-x}$ Detected by Scanning Tunneling Spectroscopy, *Phys. Rev. Lett.* **75**, 1387 (1995).
44. T. Hanaguri, C. Lupien, Y. Kohsaka, D. H. Lee, M. Azuma, M. Takano, H. Takagi, and J. C. Davis, A 'checkerboard' electronic crystal state in lightly hole-doped $\text{Ca}_{2-x}\text{Na}_x\text{CuO}_2\text{Cl}_2$, *Nature* **430**, 1001 (2004).
45. D. Grebille, H. Leligny, A. Ruyter, P. Labbé, and B. Raveau, Static disorder in the incommensurate structure of the high Tc superconductor $\text{Bi}_2\text{Sr}_2\text{CaCu}_2\text{O}_{8+\delta}$, **52**, 628 (1996).
46. K. McElroy, J. Lee, J. A. Slezak, D. H. Lee, H. Eisaki, S. Uchida, and J. C. Davis, Atomic-Scale Sources and Mechanism of Nanoscale Electronic Disorder in $\text{Bi}_2\text{Sr}_2\text{CaCu}_2\text{O}_{8+d}$, *Science* **309**, 1048 (2005).
47. I. Martin and A. V. Balatsky, Doping-induced inhomogeneity in high-Tc superconductors, *Physica C* 357-360, 46 (2001).
48. Q.-H. Wang, J. H. Han, and D.-H. Lee, Pairing near the Mott insulating limit, *Phys. Rev. B* **65**, 054501 (2001).

49. Z. Wang, J. R. Engelbrecht, S. Wang, H. Ding, and S. H. Pan, Inhomogeneous d-wave superconducting state of a doped Mott insulator, *Phys. Rev. B* **65**, 064509 (2002).
50. T. S. Nunner, B. M. Andersen, A. Melikyan, and P. J. Hirschfeld, Dopant-Modulated Pair Interaction in Cuprate Superconductors, *Phys. Rev. Lett.* **95**, 177003 (2005).
51. I. Giaever, H. R. Hart, and K. Megerle, *Phys. Rev.* **126**, 941 (1962).
52. W. L. McMillan and J. M. Rowell, Lead Phonon Spectrum Calculated from Superconducting Density of States, *Phys. Rev. Lett.* **14**, 108 (1965).
53. G. M. Eliashberg, *Zh. Eksperim. i Teor. Fiz.* **38**, 966 (1960).
54. Q. Huang, J. F. Zasadzinski, K. E. Gray, J. Z. Liu, and H. Claus, Electron tunneling study of the normal and superconducting states of $\text{Bi}_{1.7}\text{Pb}_{0.3}\text{Sr}_2\text{CaCu}_2\text{O}_x$, *Phys. Rev. B* **40**, 9366 (1989).
55. Q. Huang, J. F. Zasadzinski, N. Tralshawala, K. E. Gray, D. G. Hinks, J. L. Peng, and R. L. Greene, Tunnelling evidence for predominantly electron-phonon coupling in superconducting $\text{Ba}_{1-x}\text{K}_x\text{BiO}_3$ and $\text{Nd}_{2-x}\text{Ce}_x\text{CuO}_{4-y}$, *Nature* **347**, 369 (1990).
56. Y. DeWilde *et al.*, Unusual Strong-Coupling Effects in the Tunneling Spectroscopy of Optimally Doped and Overdoped $\text{Bi}_2\text{Sr}_2\text{CaCu}_2\text{O}_{8+\delta}$, *Phys. Rev. Lett.* **80**, 153 (1998).
57. C. Renner, B. Revaz, J. Y. Genoud, K. Kadowaki, and Fischer, Pseudogap Precursor of the Superconducting Gap in Under- and Overdoped $\text{Bi}_2\text{Sr}_2\text{CaCu}_2\text{O}_{8+\delta}$, *Phys. Rev. Lett.* **80**, 149 (1998).
58. L. Ozyuzer, J. F. Zasadzinski, C. Kendziora, and K. E. Gray, Quasiparticle and Josephson tunneling of overdoped $\text{Bi}_2\text{Sr}_2\text{CaCu}_2\text{O}_{8+\delta}$ single crystals, *Phys. Rev. B* **61**, 3629 (2000).
59. P. Romano, L. Ozyuzer, Z. Yusof, C. Kurter, and J. F. Zasadzinski, Modeling study of the dip-hump feature in $\text{Bi}_2\text{Sr}_2\text{CaCu}_2\text{O}_{8+\delta}$ tunneling spectroscopy, *Phys. Rev. B* **73**, 092514 (2006).
60. P. V. Bogdanov, Evidence for an energy scale for quasiparticle dispersion in $\text{Bi}_2\text{Sr}_2\text{CaCu}_2\text{O}_8$, *Phys. Rev. Lett.* **85**, 2581 (2000).

61. P. D. Johnson, Doping and temperature dependence of the mass enhancement observed in the cuprate $\text{Bi}_2\text{Sr}_2\text{CaCu}_2\text{O}_{8+\delta}$, *Phys. Rev. Lett.* **87**, 177007 (2001).
62. A. Kaminski, Renormalization of spectral line shape and dispersion below T_c in $\text{Bi}_2\text{Sr}_2\text{CaCu}_2\text{O}_{8+\delta}$, *Phys. Rev. Lett.* **86**, 1070 (2001).
63. A. Lanzara, Evidence for ubiquitous strong electron-phonon coupling in high-temperature superconductors, *Nature* **412**, 510 (2001).
64. S. V. Borisenko, Anomalous enhancement of the coupling to the magnetic resonance mode in underdoped Pb-Bi2212, *Phys. Rev. Lett.* **90**, 207001 (2003).
65. T. Cuk, Coupling of the B1g phonon to the antinodal electronic states of $\text{Bi}_2\text{Sr}_2\text{Ca}_{0.92}\text{Y}_{0.08}\text{Cu}_2\text{O}_{8+\delta}$, *Phys. Rev. Lett.* **93**, 117003 (2004).
66. T. E. Mason, G. Aeppli, S. M. Hayden, A. P. Ramirez, and H. A. Mook, Low energy excitations in superconducting $\text{La}_{1.8}\text{Sr}_{0.14}\text{CuO}_4$, *Phys. Rev. Lett.* **71**, 919 (1993).
67. C. H. Lee, K. Yamada, Y. Endoh, G. Shirane, R. J. Birgeneau, M. A. Kastner, M. Greven, and Y.-J. Kim, Energy Spectrum of Spin Fluctuations in Superconducting $\text{La}_{2-x}\text{Sr}_x\text{CuO}_4$ ($0.10 \leq x \leq 0.25$), *J. Phys. Soc. Jpn.* **69**, 1170 (2000).
68. S. M. Hayden, H. A. Mook, P. Dai, T. G. Perring, and F. Dogan, The structure of the high-energy spin excitations in a high-transition-temperature superconductor, *Nature* **429**, 531 (2004).
69. Y. Sidis, Magnetic resonant excitations in high- T_c superconductors, *Phys. Status. Solidi. B* **241**, 1204 (2004).
70. J. M. Tranquada, Quantum magnetic excitations from stripes in copper oxide superconductors, *Nature* **429**, 534 (2004).
71. R. J. Birgeneau, C. Stock, J. M. Tranquada, and K. Yamada, Magnetic neutron scattering in hole doped cuprate superconductors, *J. Phys. Soc. Jpn.* **75**, 111003 (2006).
72. R. J. McQueeney, Anomalous dispersion of LO phonons in $\text{La}_{1.85}\text{Sr}_{0.15}\text{CuO}_4$ at low temperatures, *Phys. Rev. Lett.* **82**, 628 (1999).

73. Y. Petrov, T. Egami, R. J. McQueeney, M. Yethiraj, H. A. Mook, and F. Dogan, Phonon Signature of Charge Inhomogeneity in High Temperature Superconductors $\text{YBa}_2\text{Cu}_3\text{O}_{6+x}$, Preprint at <<http://arxiv.org/abs/cond> (2000).
74. M. Matsuda, M. Fujita, K. Yamada, R. J. Birgeneau, Y. Endoh, and G. Shirane, Electronic phase separation in lightly doped $\text{La}_{2-x}\text{Sr}_x\text{CuO}_4$, Phys. Rev. B **65**, 134515 (2002).
75. B. C. Stipe, M. A. Rezaei, and W. Ho, Single-Molecule Vibrational Spectroscopy and Microscopy, Science **280**, 1732 (1998).
76. A. J. Heinrich, J. A. Gupta, C. P. Lutz, and D. M. Eigler, Single-Atom Spin-Flip Spectroscopy, Science **306**, 466 (2004).
77. J. X. Zhu, J. Sun, Q. Si, and A. V. Balatsky, Effects of a collective spin resonance mode on the scanning tunnelling microscopy spectra of d-wave superconductors, Phys. Rev. Lett. **92**, 017002 (2004).
78. J.-X. Zhu, K. McElroy, J. Lee, T. P. Devereaux, Q. Si, J. C. Davis, and A. V. Balatsky, Effects of τ_1 Scattering on Fourier-Transformed Inelastic Tunneling Spectra in High- T_c Cuprates with Bosonic Modes, Preprint at <<http://arxiv.org/abs/cond> (2005).
79. S. Pilgram, T. M. Rice, and M. Sigrist, Role of Inelastic Tunneling through the Insulating Barrier in Scanning-Tunneling-Microscope Experiments on Cuprate Superconductors, Phys. Rev. Lett. **97**, 117003 (2006).
80. Y. Ohta, T. Tohyama, and S. Maekawa, Apex oxygen and critical temperature in copper oxide superconductors: Universal correlation with the stability of local singlets, Phys. Rev. B **43**, 2968 (1991).
81. F. C. Zhang and T. M. Rice, Effective Hamiltonian for the superconducting Cu oxides, Phys. Rev. B **37**, 3759 (1988).
82. J. P. Attfield, A. L. Kharlanov, and J. A. McAllister, Cation effects in doped La_2CuO_4 superconductors, Nature **394**, 157 (1998).
83. L. Forr, V. Ilakovac, and B. Keszei, High-pressure study of $\text{Bi}_2\text{Sr}_2\text{CaCu}_2\text{O}_8$ single crystals, Phys. Rev. B **41**, 9551 (1990).
84. X.-J. Chen, V. V. Struzhkin, R. J. Hemley, H.-k. Mao, and C. Kendziora, High-pressure phase diagram of $\text{Bi}_2\text{Sr}_2\text{CaCu}_2\text{O}_{8+\delta}$ single crystals, Phys. Rev. B **70**, 214502 (2004).

85. Y. A. N. Gao, P. Lee, P. Coppens, M. A. Subramania, and A. W. Sleight, The Incommensurate Modulation of the 2212 Bi-Sr-Ca-Cu-O Superconductor, *Science* **241**, 954 (1988).
86. V. Petricek, Y. Gao, P. Lee, and P. Coppens, X-ray analysis of the incommensurate modulation in the 2:2:1:2 Bi-Sr-Ca-Cu-O superconductor including the oxygen atoms, *Phys. Rev. B* **42**, 387 (1990).
87. X. B. Kan and S. C. Moss, Four-dimensional crystallographic analysis of the incommensurate modulation in a $\text{Bi}_2\text{Sr}_2\text{CaCu}_2\text{O}_8$ single crystal, *Acta. Cryst. B* **48**, 122 (1991).
88. A. Bianconi, M. Lusignoli, N. L. Saini, P. Bordet, K. V. Kvik, and P. G. Radaelli, Stripe structure of the CuO_2 plane in $\text{Bi}_2\text{Sr}_2\text{CaCu}_2\text{O}_{8+y}$ by anomalous x-ray diffraction, *Phys. Rev. B* **54**, 4310 (1996).
89. M. Zhiqiang, X. Gaojie, Z. Shuyuan, T. Shun, L. Bin, T. Mingliang, F. Chenggao, X. Cunyi, and Z. Yuheng, Relation of the superstructure modulation and extra-oxygen local-structural distortion in $\text{Bi}_{2.1-y}\text{Pb}_y\text{Sr}_{1.9-x}\text{La}_x\text{CuO}_z$, *Phys. Rev. B* **55**, 9130 (1997).
90. J. A. Slezak, Thesis, Chapter 3 (2007).
91. H.-D. Chen, J.-P. Hu, S. Capponi, E. Arrigoni, and S.-C. Zhang, Antiferromagnetism and Hole Pair Checkerboard in the Vortex State of High T_c Superconductors, *Phys. Rev. Lett.* **89**, 137004 (2002).
92. D. Podolsky, E. Demler, K. Damle, and B. I. Halperin, Translational symmetry breaking in the superconducting state of the cuprates: Analysis of the quasiparticle density of states, *Phys. Rev. B* **67**, 094514 (2003).
93. H.-D. Chen, O. Vafek, A. Yazdani, and S.-C. Zhang, Pair Density Wave in the Pseudogap State of High Temperature Superconductors, *Phys. Rev. Lett.* **93**, 187002 (2004).
94. Z. Tezanovic, Charge Modulation, Spin Response, and Dual Hofstadter Butterfly in High- T_c Cuprates, *Phys. Rev. Lett.* **93**, 217004 (2004).
95. Y. He, T. S. Nunner, P. J. Hirschfeld, and H. P. Cheng, Local Electronic Structure of $\text{Bi}_2\text{Sr}_2\text{CaCu}_2\text{O}_8$ near Oxygen Dopants: A Window on the High- T_c Pairing Mechanism, *Phys. Rev. Lett.* **96**, 197002 (2006).
96. W.-G. Yin and W. Ku, Tuning Hole Mobility, Concentration, and Repulsion in High- T_c Cuprates via Apical Atoms, Preprint at <http://arxiv.org/abs/cond> (2007).

97. K.-Y. Yang, T. M. Rice, and F.-C. Zhang, Effect of superlattice modulation of electronic parameters on the density of states of cuprate superconductors, *Phy. Rev. B* **76**, 100501 (2007).
98. G. Kinoda, H. Mashima, K. Shimizu, J. Shimoyama, K. Kishio, and T. Hasegawa, Direct determination of localized impurity levels located in the blocking layers of $\text{Bi}_2\text{Sr}_2\text{CaCu}_2\text{O}_y$ using scanning tunneling microscopy/spectroscopy, *Phy. Rev. B* **71**, 020502 (2005).
99. J. A. Slezak, J. Lee, M. Wang, K. McElroy, K. Fujita, B. M. Andersen, P. J. Hirschfeld, H. Eisaki, S. Uchida, and J. C. Davis, From the Cover: Imaging the impact on cuprate superconductivity of varying the interatomic distances within individual crystal unit cells, *Proc. Natl. Acad. Sci. U.S.A.* **105**, 3203 (2008).
100. J. Lee *et al.*, Interplay of electron-Lattice interactions and superconductivity in $\text{Bi}_2\text{Sr}_2\text{CaCu}_2\text{O}_{8+\delta}$, *Nature* **442**, 546 (2006).
101. A. R. Bishop *et al.*, Real and marginal isotope effects in cuprate superconductors, *Journal of Superconductivity and Novel Magnetism* **20**, 393 (2007).
102. X. J. Chen, B. Liang, C. Ulrich, C. T. Lin, V. V. Struzhkin, Z. G. Wu, R. J. Hemley, H. K. Mao, and H. Q. Lin, Oxygen isotope effect in $\text{Bi}_2\text{Sr}_2\text{Ca}_{n-1}\text{Cu}_2\text{O}_{2n+4+\delta}$ ($n=1,2,3$) single crystals, *Phys. Rev. B* **76**, 140502 (2007).
103. J. Hwang, T. Timusk, and J. P. Carbotte, Scanning-tunnelling spectroscopy, *Nature* **446**, E3 (2007).
104. A. V. Balatsky and J.-X. Zhu, Local strong-coupling pairing in d-wave superconductors with inhomogeneous bosonic modes, *Phy. Rev. B* **74**, 094517 (2006).
105. X.-J. Chen, V. V. Struzhkin, Z. Wu, R. J. Hemley, H.-k. Mao, and H.-Q. Lin, Phonon-mediated superconducting transitions in layered cuprate superconductors, *Phy. Rev. B* **75**, 134504 (2007).
106. T. Egami, Lattice effects in cuprates, *Physica C* **460**, 267 (2007).
107. M. K. Crawford, W. E. Farneth, E. M. McCarron, R. L. Harlow, and A. H. Moudden, Oxygen isotope effect and structural phase-transitions in La_2CuO_4 -based superconductors, *Science* **250**, 1390 (1990).

108. T. Schneider and H. Keller, Universal trends in extreme type-II superconductors, *Phys. Rev. Lett.* **69**, 3374 (1992).
109. G.-m. Zhao, K. K. Singh, A. P. B. Sinha, and D. E. Morris, Oxygen isotope effect on the effective mass of carriers from magnetic measurements on $\text{La}_{2-x}\text{Sr}_x\text{CuO}_4$, *Phys. Rev. B* **52**, 6840 (1995).
110. G.-m. Zhao, M. B. Hunt, H. Keller, and K. A. Muller, Evidence for polaronic supercarriers in the copper oxide superconductors $\text{La}_{2-x}\text{Sr}_x\text{CuO}_4$, *Nature* **385**, 236 (1997).
111. J. Hofer, K. Conder, T. Sasagawa, G.-m. Zhao, M. Willemin, H. Keller, and K. Kishio, Oxygen-Isotope Effect on the In-Plane Penetration Depth in Underdoped $\text{La}_{2-x}\text{Sr}_x\text{CuO}_4$ Single Crystals, *Phys. Rev. Lett.* **84**, 4192 (2000).
112. T. Schneider and H. Keller, Isotope Effects in Underdoped Cuprate Superconductors: A Quantum Critical Phenomenon, *Phys. Rev. Lett.* **86**, 4899 (2001).
113. G.-m. Zhao, V. Kirtikar, and D. E. Morris, Isotope effects and possible pairing mechanism in optimally doped cuprate superconductors, *Phys. Rev. B* **63**, 220506 (2001).
114. G. H. Gweon, An unusual isotope effect in a high-transition-temperature superconductor, *Nature* **430**, 187 (2004).
115. T. Hanaguri, Y. Kohsaka, J. C. Davis, C. Lupien, I. Yamada, M. Azuma, M. Takano, K. Ohishi, M. Ono, and H. Takagi, Quasiparticle interference and superconducting gap in $\text{Ca}_{2-x}\text{Na}_x\text{CuO}_2\text{Cl}_2$, *Nat. Phys.* **3**, 865 (2007).
116. K. McElroy, D. H. Lee, J. E. Hoffman, K. M. Lang, J. Lee, E. W. Hudson, H. Eisaki, S. Uchida, and J. C. Davis, Coincidence of Checkerboard Charge Order and Antinodal State Decoherence in Strongly Underdoped Superconducting $\text{Bi}_2\text{Sr}_2\text{CaCu}_2\text{O}_{8+\delta}$, *Phys. Rev. Lett.* **94**, 197005 (2005).
117. K. Fujita, I. Grigorenko, J. Lee, M. Wang, J.-X. Zhu, J. C. Davis, H. Eisaki, S. Uchida, and A. V. Balatsky, Bogoliubov angle and visualization of particle-hole mixture in superconductors, Preprint at <http://arxiv.org/abs/0709.0632> (2007).
118. Y. Kohsaka *et al.*, Quasiparticle extinction with approaching Mottness in $\text{Bi}_2\text{Sr}_2\text{CaCu}_2\text{O}_{8+d}$, submitted (2008).

119. M. Eschrig and M. R. Norman, Effect of the magnetic resonance on the electronic spectra of high-Tc superconductors, *Phys. Rev. B* **67**, 144503 (2003).
120. J. Mesot *et al.*, Superconducting Gap Anisotropy and Quasiparticle Interactions: A Doping Dependent Photoemission Study, *Phys. Rev. Lett.* **83**, 840 (1999).
121. A. V. Chubukov, M. R. Norman, A. J. Millis, and E. Abrahams, Gapless pairing and the Fermi arc in the cuprates, *Phys. Rev. B* **76**, 180501 (2007).
122. M. R. Norman, A. Kanigel, M. Randeria, U. Chatterjee, and J. C. Campuzano, Modeling the Fermi arc in underdoped cuprates, *Phys. Rev. B* **76**, 174501 (2007).
123. J. W. Alldredge *et al.*, Evolution of the electronic excitation spectrum with strongly diminishing hole density in superconducting $\text{Bi}_2\text{Sr}_2\text{CaCu}_2\text{O}_{8+\delta}$, *Nat. Phys.* **4**, 319 (2008).
124. W. Chen, Private communication
125. J. F. Douglas *et al.*, Superconductors - Unusual oxygen isotope effects in cuprates?, *Nature* **446**, E5 (2007).
126. W. L. McMillan and J. M. Rowell, *Superconductivity*. 1969. p. 561.
127. A. N. Pasupathy, A. Pushp, K. K. Gomes, C. V. Parker, J. Wen, Z. Xu, G. Gu, S. Ono, Y. Ando, and A. Yazdani, Electronic Origin of the Inhomogeneous Pairing Interaction in the High-Tc Superconductor $\text{Bi}_2\text{Sr}_2\text{CaCu}_2\text{O}_{8+\delta}$, *Science* **320**, 196 (2008).
128. Y. J. Uemura *et al.*, Universal Correlations between T_c and n_s/m^* (Carrier Density over Effective Mass) in High-Tc Cuprate Superconductors, *Phys. Rev. Lett.* **62**, 2317 (1989).
129. M. Alexandru and M. Jarrell, The isotope effect in the Hubbard model with local phonons, arXiv: Preprint at <<http://arxiv.org/abs/0803.0567v1>> (2008).
130. M. Alexandru, B. Moritz, M. Jarrell and T. Maier, Suppression of superconductivity in the Hubbard model by buckling and breathing phonons, arXiv: Preprint at <<http://arxiv.org/abs/cond-mat/0611067>> (2006).

- 131. M. K. Crawford, W. E. Farneth, E. M. McCarron, III, R. L. Harlow, and A. H. Moudden, Oxygen Isotope Effect and Structural Phase Transitions in La_2CuO_4 -Based Superconductors, *Science* **250**, 1390 (1990).
- 132. R.S. Perry, *et al.*, Metamagnetism and Critical Fluctuations in High Quality Single Crystals of the Bilayer Ruthenate $\text{Sr}_3\text{Ru}_2\text{O}_7$, *Phys. Rev. Lett.* **86**, 2661 (2001).
- 133. R.A. Borzi, S.A. Grigera, J. Farrell, R.S. Perry, S.J.S. Lister, S.L. Lee, D.A. Tennant, Y. Maeno, and A.P. Mackenzie, Formation of a Nematic Fluid at High Fields in $\text{Sr}_3\text{Ru}_2\text{O}_7$, *Science* **315**, 214 (2007).
- 134. J. Hooper, *et al.*, Competing magnetic fluctuations in $\text{Sr}_3\text{Ru}_2\text{O}_7$ probed by Ti doping, *Phys. Rev. B* **75**, 060403 (2007).